

Two-dimensional metal-organic networks as templates for the self-assembly of atom and cluster arrays

THÈSE N° 6885 (2016)

PRÉSENTÉE LE 19 FÉVRIER 2016
À LA FACULTÉ DES SCIENCES DE BASE
LABORATOIRE DE NANOSTRUCTURES SUPERFICIELLES
PROGRAMME DOCTORAL EN PHYSIQUE

ÉCOLE POLYTECHNIQUE FÉDÉRALE DE LAUSANNE

POUR L'OBTENTION DU GRADE DE DOCTEUR ÈS SCIENCES

PAR

Giulia Elisabetta PACCHIONI

acceptée sur proposition du jury:

Prof. V. Savona, président du jury
Prof. H. Brune, Dr M. Pivetta, directeurs de thèse
Prof. R. Fasel, rapporteur
Prof. K. Franke, rapporteuse
Dr M. Lingenfelder, rapporteuse



ÉCOLE POLYTECHNIQUE
FÉDÉRALE DE LAUSANNE

Suisse
2016

"You see, Momo," he told her one day, "it's like this. Sometimes, when you've a very long street ahead of you, you think how terribly long it is and feel sure you'll never get it swept."

He gazed silently into space before continuing. "And then you start to hurry," he went on.

"You work faster and faster, and every time you look up there seems to be just as much left to sweep as before, and you try even harder, and you panic, and in the end you're out of breath and have to stop - and still the street stretches away in front of you. That's not the way to do it."

He pondered a while. Then he said, "You must never think of the whole street at once, understand? You must only concentrate on the next step, the next breath, the next stroke of the broom, and the next, and the next. Nothing else."

Again he paused for thought before adding, "That way you enjoy your work, which is important, because then you make a good job of it. And that's how it ought to be."

There was another long silence. At last he went on, "And all at once, before you know it, you find you've swept the whole street clean, bit by bit. What's more, you aren't out of breath."

He nodded to himself. "That's important, too," he concluded.

— *Michael Ende*

A Luca

Abstract

This thesis presents a study of the use of two-dimensional metal-organic systems as templates for the organization of metal atoms and clusters on surfaces.

We start with a systematic characterization of the metal-organic porous networks formed on Cu(111) by polyphenyl-dicarbonitrile molecules, and of the temperature dependence of the assembly process, leading to a variety of geometrical structures. Using molecules of two different lengths we observe networks with distinct periodicities, and we reveal a competition between the different interactions governing the assembly.

We also study the self-assembly of a single molecule magnet on supported graphene, observing the same disposition as in a layer of the molecular crystal, which explains the high magnetic anisotropy measured for the system.

The metal-organic template is used to organize metal atoms and clusters in the network pores, obtaining a regular array of clusters with a narrow size distribution. We demonstrate how this approach can be used to produce clusters of different elements, such as Fe, Co and Er, as well as mixed transition metal - rare earth metal clusters.

Otherwise, the metal-organic networks can be used to organize Fe atoms under the molecules, in which case a two-orbital Kondo system with a marked spatial dependence is obtained. After characterizing the magnetic properties of Fe atoms adsorbed on bare Cu(111), we use a combination of scanning tunneling spectroscopy, density functional theory and x-ray absorption and dichroism to study the Kondo effect of the Fe-molecule system, identifying the involved magnetic orbitals and demonstrating that they are both Kondo screened.

Keywords: Scanning tunneling microscopy (STM), scanning tunneling spectroscopy (STS), self-assembly, metal-organic networks, supramolecular architectures, templates, nanostructures, clusters, Kondo effect.

Résumé

Ce travail de thèse présente une étude sur l'utilisation de réseaux bidimensionnels métallo-organiques pour l'organisation d'atomes et d'agrégats métalliques en surface.

Nous commençons par une caractérisation systématique des réseaux métallo-organiques formés sur une surface de Cu(111) par des molécules polyphenyl-dicarbonitrile, et de l'effet de la température sur le processus d'assemblage, qui donne comme résultat différentes structures géométriques. En utilisant des molécules de deux longueurs différentes, nous obtenons des réseaux de périodicités distinctes, et nous observons une compétition entre les différentes interactions qui contrôlent l'assemblage du système. Nous étudions aussi l'auto-assemblage d'une molécule magnétique, qui s'organise sur une couche de graphène comme dans une couche du cristal moléculaire. Cela explique la valeur élevée de l'anisotropie magnétique mesurée pour ce système.

Les réseaux métallo-organiques sont utilisés pour organiser des atomes et des agrégats métalliques dans les cavités du réseau. Le résultat est l'obtention d'un réseau d'agrégats avec une distribution de taille étroite. Nous montrons comment cette procédure peut être utilisée pour obtenir des agrégats d'éléments différents, comme Fe, Co et Er, mais aussi des agrégats mixtes de métaux de transition et de terres rares.

Ces réseaux métallo-organiques peuvent aussi être utilisés pour fixer des atomes métalliques sous les molécules. Avec le Fe dans cette configuration, un effet Kondo avec une forte dépendance spatiale et deux canaux d'écrantage se manifeste. Nous caractérisons d'abord les propriétés des atomes de Fe sur le substrat, Cu(111). Ensuite nous utilisons la spectroscopie à balayage à effet tunnel, la théorie de la fonctionnel de la densité et l'absorption et le dichroïsme circulaire de rayons X pour étudier l'effet Kondo qui se produit lorsque le Fe est situé sous une molécule. Nous pouvons ainsi identifier les deux orbitales magnétiques qui participent à l'effet Kondo, et démontrer que les deux sont écrantées.

Mots clefs : Microscopie à balayage à effet tunnel (STM), spectroscopie à balayage à effet tunnel (STS), auto-assemblage, réseaux métallo-organiques, architectures supramoléculaires, nanostructures, templates, agrégats, effet Kondo.

Contents

Abstract (English/Français)	i
Introduction	1
1 Methods	5
1.1 Scanning Tunneling Microscopy	5
1.1.1 A simple theory of STM and STS	6
1.1.2 Measuring with functionalized tips	7
1.1.3 The experimental setup	9
1.2 Measuring magnetic properties: XAS and XMCD	10
Part I: Molecular Self-Assembly	13
2 NC-Ph_n-CN/Cu(111): Deposition @ RT	15
2.1 Introduction	15
2.2 NC-Ph ₅ -CN	17
2.2.1 Chain assembly	17
2.2.2 Honeycomb network	19
2.2.3 Measurements @ RT: compact structure	21
2.2.4 Spectroscopy on the honeycomb network	22
2.3 NC-Ph ₃ -CN	23
2.3.1 Chain assembly	23
2.3.2 Honeycomb network	24
2.3.3 Coverage-dependent structures	27
2.3.4 Spectroscopy on the chain and honeycomb structures	27
2.4 Comparison between the two molecules for deposition @ RT	30
2.5 Codeposition of NC-Ph ₅ -CN and NC-Ph ₃ -CN	31
2.6 Conclusions	32
3 NC-Ph_n-CN/Cu(111): Temperature-dependent Assemblies	35
3.1 Introduction	35
3.2 NC-Ph ₅ -CN	35
3.2.1 Truncated triangles network	35
3.2.2 Kagome network	37

Contents

3.2.3	Triangular structure	38
3.2.4	Spectroscopy on the NC-Ph ₅ -CN temperature-dependent assemblies . .	40
3.3	NC-Ph ₃ -CN	42
3.3.1	Truncated triangles network	42
3.3.2	Kagome network	44
3.3.3	Chevron pattern	45
3.3.4	Open kagome network	46
3.3.5	Annealing @ RT	47
3.3.6	Spectroscopy on the NC-Ph ₃ -CN temperature-dependent assemblies . .	48
3.4	Conclusions	50
4	Er(trensal) single molecule magnets	53
4.1	Introduction	53
4.2	Magnetic properties of Er(trensal)	53
4.3	STM measurements	56
4.4	Conclusions	59
Part II: Use of the networks as templates for the organization of metal atoms and clusters		61
5	Use of the molecular networks as templates	63
5.1	Introduction	63
5.2	Confinement of the surface state	63
5.3	Deposition of Fe on the NC-Ph ₅ -CN honeycomb template	64
5.3.1	Cluster formation	67
5.3.2	Higher Fe coverage	68
5.3.3	Fe deposition at 18 K	68
5.3.4	Thermal stability	70
5.3.5	Other NC-Ph ₅ -CN networks used as templates	71
5.4	Deposition of Fe on the NC-Ph ₃ -CN honeycomb template	72
5.5	Co clusters on NC-Ph ₅ -CN honeycomb template	75
5.6	Er clusters on NC-Ph ₅ -CN honeycomb template	77
5.7	Mixed Co-Er clusters on NC-Ph ₅ -CN template	79
5.8	Conclusions	81
Part III: Magnetic properties		83
6	Magnetic properties of Fe atoms and clusters on Cu(111)	85
6.1	Introduction	85
6.2	Fe monomers on Cu(111)	86
6.3	Small Fe clusters on Cu(111)	92
6.4	Conclusions	95

7 Two-orbital Kondo effect on metal-organic complexes	97
7.1 Introduction	97
7.2 STS measurements	98
7.3 DFT calculations	100
7.4 XAS and XMCD measurements	102
7.5 Conclusions	105
8 Conclusions and perspectives	107
Bibliography	128
Acknowledgements	129
Curriculum Vitae	131

Introduction

It was in the autumn of 1986 that readers could see for the first time, in the journal *Surface Science*, a real-space image of individual organic molecules, copper phthalocyanines adsorbed on a silver surface [1] [Fig. 1(a)]. The first high-resolution images of the same molecule, showing the adsorption configuration and some intramolecular details, were published three years later [2] [Fig. 1(b)]. This was made possible by the invention of a powerful instrument for the investigation of matter at the nanoscale: the Scanning Tunneling Microscope, or STM. The authors write that "these observations [...] suggest a strong potential for STM as a tool for observing molecular phenomena, provided STM image contrast is understood and molecular motion [...] can be overcome". Almost thirty years later we can say that this forecast was completely fulfilled, also thanks to the advent of cryogenic STM in 1984 [3]. STMs can nowadays be used to investigate molecules from different perspectives, allowing to characterize their properties from the vibrational, optical, electronic and magnetic point of view, and giving access to their interaction with the substrate and with each other.

Inelastic Electron Tunneling Spectroscopy (IETS), that was known as a technique to investigate molecular vibrational spectra well before the invention of STM [4], was soon identified by Binnig and Rohrer as a promising way to exploit the STM potential [5]; STM-IETS permits to obtain vibrational fingerprints at the single molecule level, as experimentally demonstrated in the late '90s [6]. By the way, IETS was also suggested to be the mechanism at the base of the sense of smell [7], which would provide a quantum mechanical explanation for a problem of molecular biology.

Scanning Tunneling Spectroscopy (STS), the spectroscopic mode of STM, also became almost immediately an important complement to the topographical information obtained with the microscope, providing information on the electronic structure of the sample in the form of current-voltage spectra [8].

In the '90s it was demonstrated that photon emission can be stimulated with the STM tip [9], opening the way to integration of fluorescence and phosphorescence spectroscopy with the topographic measurements, a powerful tool for the optical characterization of molecules on surfaces [10, 11].

STM has also been a key instrument for the development of a field of high interest involving the characterization and study of molecules: molecular electronics. Although research in this direction dates back to the '70s [12, 13], STM allowed for the first time to measure the conductance of single molecules [14], marking the true beginning of molecular electronics and providing an important tool in the quest for the miniaturization of circuit components

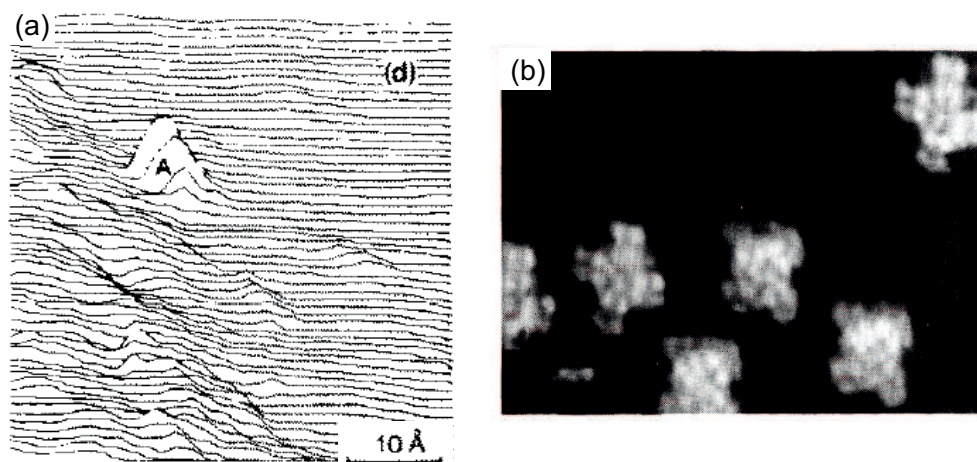


Figure 1: First images of a molecule on a surface: (a) STM scan showing a copper phthalocyanine on silver, $V_t = 600$ mV, $I_t = 350$ pA (1986), adapted with permission from [1] and (b) high resolution STM image of a group of copper phthalocyanines on Cu(100), $V_t = 150$ mV, $I_t = 2$ nA (1989), adapted with permission from [2].

to the very limit, that of a single molecule, to produce ever faster and cheaper computers. Organic molecules are widely studied also for other applications in electronics, such as organic light-emitting diodes [15] and molecule-based photovoltaics [16].

Another direction that is being explored to meet the challenge of the fabrication of single molecule transistors exploits the quantum nature of molecules using the electron spin: it is the field of molecular spintronics [17]. Also in this case, an ingenious use of STM produced a powerful tool for the study of magnetic properties of single molecules: the spin-polarized STM [18, 19], where a tip coated with a magnetic material acts as a spin valve to reveal the magnetic structure of the sample.

Thus there are many reasons why the study of molecules on surfaces is a subject of great interest, and STM, thanks to its versatility, can give access to different properties of the system under study. However, beyond the characterization of the properties of single molecules, it is also interesting to investigate their use as building blocks for creating more complex structures. These can also include metal centers which can be of interest, for example, for their magnetic or catalytic properties. In three dimensions, the combination of organic molecules and metal centers to create metal organic frameworks (MOFs) has been widely explored. These structures offer high surface area, tunable porosity and a wide choice of metallic centers. Promising applications include hydrogen storage [20], which is an important issue if hydrogen is to become seriously used in fuel cells, heterogeneous catalysis [21], gas separation [22], for example for CO₂ capture, and drug delivery [23]; examples are shown in Fig. 2(a) and (b).

Molecular self assembly on surfaces is widely studied as well, to explore the properties of two-dimensional nanoscale materials [24, 25, 26, 27]. One example is shown in Fig. 2(c). Unlike top-down approaches, requiring active manipulation of the surface and suffering from limited resolution and slowness, self-assembly is driven by intrinsic properties of the system

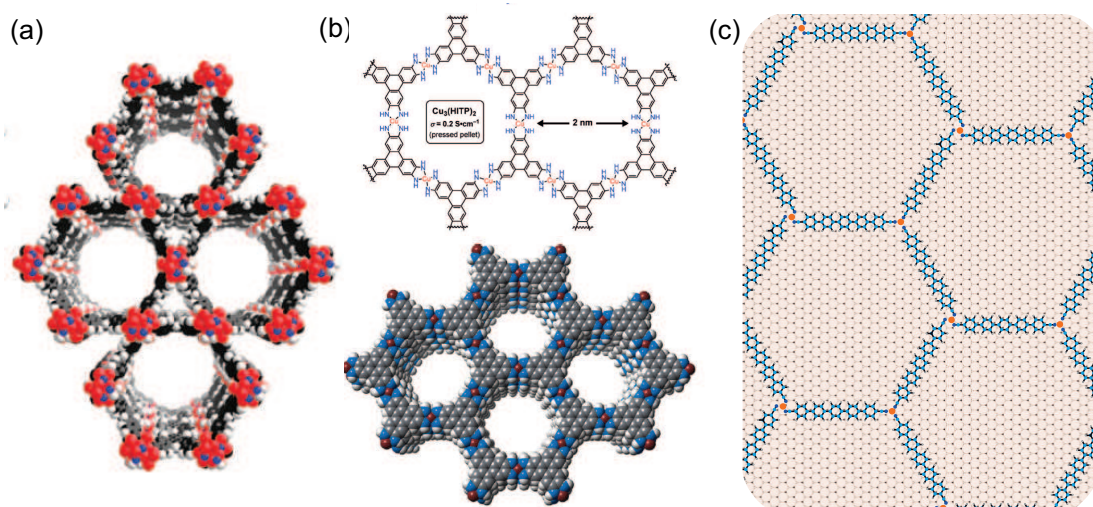


Figure 2: Examples of self-assembled metal-organic structures: (a) a 3D MOF containing Zr (blue), O (red), C (black) and H (white) atoms, an effective catalyst for the destruction of chemical warfare agents (adapted with permission from [28]), (b) 2D MOF with a parallel stacking of layers, composed of N (blue), Cu (red), C (gray) and H (white); this MOF is interesting because of its high electric conductance (adapted with permission from [29]), and (c) surface-supported metal-organic network comprising N (blue), Cu (red), C (light blue) and H (grey) atoms; the surface is Cu(111). This network is described in Chapter 2.

and allows to obtain complex structures, while maintaining control at the atomic level. A wide variety of patterns can be obtained, ranging from compact to porous, from purely organic networks to metal coordinated ones; the molecular assembly can be directed through the use of template surfaces, or the molecular network itself can be used as a template for the subsequent organization of additional molecules or of atoms and clusters. This aspect is especially relevant, as being able to organize metal clusters in regular patterns is relevant, for example, for the exploitation of their magnetic and catalytic properties. Finding ways to induce their self organization is thus a subject of high interest.

In this thesis a number of these aspects are explored, after a brief introduction to the employed experimental techniques in **Chapter 1**.

Part I deals with molecular self-assembly and with the characterization of the networks that evolve in different conditions, for example upon changes in the deposition temperature or by using different substrates.

Chapters 2 and 3 explore the assemblies formed by NC-Ph₅-CN and NC-Ph₃-CN on Cu(111); this system is particularly interesting as the surface plays an active role in the determination of the molecular organization, providing - depending on the temperature - Cu atoms that act as coordination centers for the formation of metal-organic networks. Comparison between the patterns formed by the two molecules allows the identification of the interactions prevailing in the assembly process in the two cases. We present networks ranging from porous honeycomb to compact ones, along with scanning tunneling spectroscopy measurements of the molecular orbitals in the different assemblies. While **Chapter 2** focuses on the self-assembly

upon deposition on the substrate kept at room temperature, **Chapter 3** explores the effect of lowering the substrate temperature during deposition, implying a diminished availability of Cu adatoms for node coordination.

Chapter 4 describes the self-assembly of a single-molecule magnet, Er(trensal), showing that its ability to form an ordered layer on graphene supported on Ru(0001) and Ir(111) is at the base of the appealing magnetic behavior revealed by X-ray absorption and dichroism measurements.

Part II describes how the highly regular, porous networks presented in Chapters 2 and 3 can be used as templates for the self-organization of metal atoms and clusters.

Chapter 5 shows that, thanks to the confinement of the Cu(111) surface state induced by the molecular networks, atoms are steered towards the center of the network cavities, and a gentle annealing results in the formation of a regular array of clusters, one in each pore. This procedure is successfully employed to produce clusters of transition metal elements, such as Fe and Co, of rare earths, such as Er, and mixed Co-Er clusters, all regularly organized thanks to the templating effect of the molecular network. Such clusters can be interesting both from the catalytic and the magnetic point of view.

Part III is dedicated to the study of the magnetic properties of a self-assembled system prepared, again, using the molecular network presented in Chapter 2 as template.

Chapter 6 presents synchrotron measurements on Fe atoms adsorbed on Cu(111), which is an interesting system, as it exhibits multiplet features in X-ray absorption spectroscopy, that disappear upon the formation of small clusters when the coverage is increased. These measurements are needed for the calibration and interpretation of the results presented in the following chapter.

Chapter 7 is dedicated to the study of the Kondo effect that is measured on Fe atoms that are buried under the molecules. This Kondo system is interesting because it exhibits two different Kondo temperatures and line shapes, and a strong spatial anisotropy that we can attribute, thanks to the support of density functional theory calculations, to the presence of two singly occupied orbitals with different spatial distributions across the system. We further characterized the system with X-ray adsorption and dichroism measurements. In this case the molecular network is thus used as a template to organize the atoms under the molecules, and the result is the formation of a regular array of Kondo impurities.

Conclusions and perspectives are finally presented in **Chapter 8**.

1 Methods

1.1 Scanning Tunneling Microscopy

On the 29th of December 1959 Richard Feynman, in a famous lecture, expressed his vision of a future when men would be able to manipulate matter at the smallest scale, assembling atoms and molecules to create nanoscale machines. He declared: "I am not afraid to consider the final question as to whether, ultimately – in the great future – we can arrange the atoms the way we want; the very atoms, all the way down!". His dream came one step closer to reality in 1981, when the Scanning Tunneling Microscope (STM) made his appearance, making it possible to 'see' atoms for the first time.

Since its invention the STM [30, 31] has proven a powerful instrument for probing matter at the nanoscale. Over the years a huge number of systems has been investigated with STM, making it, together with the atomic force microscope and the other scanning probe techniques, an incredibly fruitful instrument for the elucidation of different properties on the scale of the extremely small. For the first time it was possible to acquire real-space images of surfaces with atomic resolution [32]. In 1986 its creators, Gerd Binnig and Heinrich Rohrer, were rewarded with the Nobel prize.

The popularity of the STM is due to its ability to image at the atomic level with very high resolution and to resolve the electronic structure of the sample on a local scale. Information on the local density of states (LDOS) of the sample can be obtained thanks to the spectroscopic STM mode, Scanning Tunneling Spectroscopy (STS). Moreover, STM can be used for bottom-up fabrication by moving individual atoms and molecules [33, 34] or to induce chemical reactions on the surface, creating bonds to form molecules or breaking them by cutting away ligands to change molecular properties [35, 36]. The experiments of Don Eigler, who first realized Feynman's dream by moving single xenon atoms on a nickel surface to spell out the IBM logo [33], and of Hyojune Lee and Wilson Ho, who used the STM tip to form a molecule of Fe(CO)₂ starting from its constituents [36], are both considered milestones of the history of nanotechnology.

The working of the instrument relies on the principle of quantum tunneling - the possibility at the quantum scale to pass through a potential barrier. When an extremely sharp conductive tip is brought very close to a conductive surface ($\approx 10^{-10}$ m) electrons can tunnel through the vacuum separating them. If a bias voltage V is applied, the Fermi levels of tip and sample,

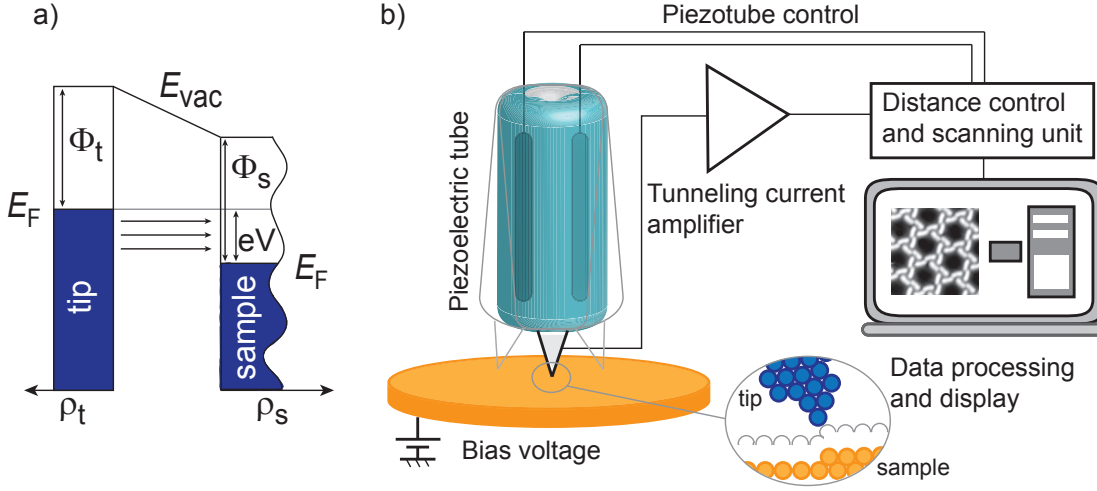


Figure 1.1: (a) Representation of DOS of sample and tip with an applied bias voltage V , showing the quantum tunneling of electrons from tip to sample. (b) Sketch of an STM system showing the general setup.

aligned at $V = 0$, shift with respect to one another by eV and a tunnel current is established, Fig. 1.1(a). The lateral position of the tip and the distance from the sample can be controlled with a precision in the picometer range via piezoelectric tubes that contract or extend under the action of an applied voltage. When the microscope is operated in constant-current mode, the current flowing between tip and sample is recorded thanks to a feedback system that ensures that the distance from the surface is adjusted as to keep the tunneling current constant. This mode of operation is the most commonly employed. The alternative is to measure in constant height mode, in which case the distance from the sample is kept constant. The operation principle of an STM is illustrated in Fig. 1.1(b).

1.1.1 A simple theory of STM and STS

One of the simplest models for the derivation of the tunneling current was first proposed by Bardeen [37] and it considers the STM tip and the sample as two parallel plates separated by an insulator. The wavefunctions of the tip and of the sample, ψ_t and ψ_s , respectively, expand in the tunnel barrier. The tunneling matrix M can be written as:

$$M = \frac{\hbar}{2m} \int_S (\psi_t^* \frac{\partial \psi_s}{\partial z} - \psi_s^* \frac{\partial \psi_t}{\partial z}) dS \quad (1.1)$$

with z the direction perpendicular to the two electrodes and S a surface comprised between them.

The probability for an electron of the tip with energy E_t to tunnel into a state of the sample with energy E_s is given by the Fermi golden rule:

$$p = \frac{2\pi}{\hbar} |M|^2 \delta(E_t - E_s) \quad (1.2)$$

where the multiplication by the Dirac delta function δ means that tunneling is allowed only between states of the same energy (elastic tunneling).

The tunneling current can be expressed as:

$$I = \frac{4\pi e}{\hbar} \int_{-\infty}^{\infty} \rho_s(E_F - eV + \epsilon) \rho_t(E_F + \epsilon) (f(E_F - eV + \epsilon) - f(E_F + \epsilon)) |M|^2 d\epsilon \quad (1.3)$$

where V is the applied voltage, f the Fermi-Dirac distribution defined as:

$$f(E) = \frac{1}{1 + e^{(E-E_F)/k_B T}} \quad (E_F = \text{Fermi energy}) \quad (1.4)$$

and ρ_t and ρ_s the density of states (DOS) of tip and sample, respectively. When the temperature is close to zero the Fermi distribution can be approximated with a step function and, since the relevant energy interval is small, $|M|$ can be treated as a constant, thus we can simplify the expression for the tunneling current as:

$$I \propto \int_0^{eV} \rho_t(\epsilon + E_F) \rho_s(\epsilon + E_F - eV) d\epsilon \quad (1.5)$$

with the energies given with respect to the Fermi level. This expression only depends on the tip and sample densities of states. It follows that the derivative of the current with respect to the voltage, the differential conductance, is expressed as:

$$\frac{dI}{dV} \propto \rho_t(E_F) \rho_s(E_F - eV) \quad (1.6)$$

It is this quantity that is measured in STS. In this kind of measurement voltage pulses are applied to the tip in order to obtain a DOS as constant as possible, so that the recorded signal gives direct access to the sample DOS. To acquire differential conductance spectra the tip is positioned over the point of the sample that one wants to probe, with I and V set to a desired value. Then the voltage is swiped across the desired range with the feedback loop open, in order to maintain a fix tip-sample distance (which is particularly important if the voltage interval goes through zero, otherwise the tip would crash on the sample at $V = 0$). Finally, a small modulation voltage is added to the bias in order to be able to record the differential conductance signal with a lock-in technique.

1.1.2 Measuring with functionalized tips

With an STM it is difficult to obtain a high geometrical resolution of the structure of complex molecules, because the measurements mainly probe the LDOS near E_F , while the chemical information about the structure of the molecule is normally contained in lower-lying orbitals. However, when a small molecule is present in the tunneling junction, a much higher contrast can be obtained. One example is constituted by Scanning Tunneling Hydrogen Microscopy (STHM) where H_2 or D_2 molecules are used to enhance the resolution, as reported for the first time by Temirov *et al.* [39]. In this situation, as explained in Ref. [38] and illustrated in Fig. 1.2, inelastic steps appear in differential conductance spectra at $\pm V_{\text{inel}}$ due to a rearrangement of

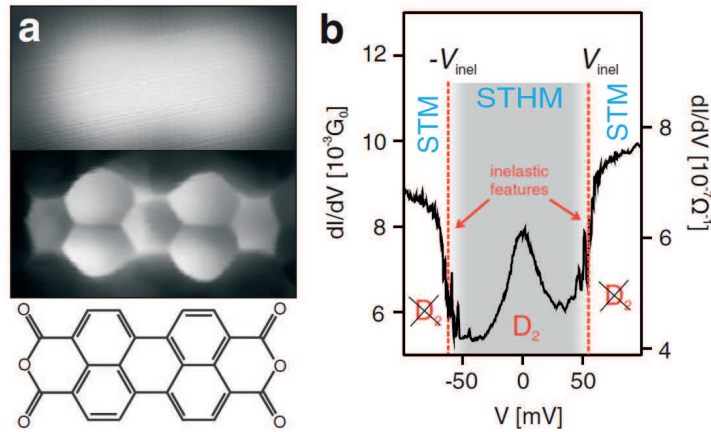


Figure 1.2: (a) STM, top ($V_t = 316$ mV), STHM, bottom (-5 mV), and structure of the molecule of PTCDA/Au(111). (b) Differential conductance acquired on the center of the molecule (lock-in parameters: 10 mV modulation, 2.3 kHz frequency). Figure adapted with permission from Ref. [38].

the atoms in the junction. By measuring at a bias such that $|eV|$ is smaller than $|eV_{inel}|$ STHM imaging is obtained (D_2 molecule between tip and surface), while it is possible to go back to the normal operating mode just by increasing the voltage above V_{inel} (D_2 displaced away from the tip apex).

The high resolution characterizing STHM can be ascribed to the Pauli exclusion principle [38, 41]: in order to have the minimum possible overlap between the wavefunctions of the D_2 and those of the atoms of the substrate, the wavefunctions rearrange locally, depleting the

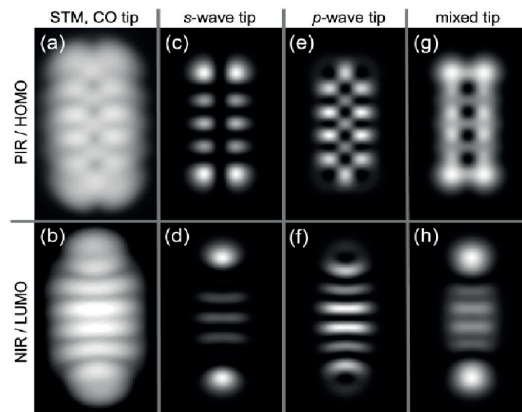


Figure 1.3: STM measurements of pentacene on 2 ML of NaCl on Cu(111) using a CO tip. (a) $I_t = 0.9$ pA, $V_t = -2.15$ V, corresponding to the positive ion resonance (PIR). (b) $I_t = 1.3$ pA, $V_t = 1.25$ V, corresponding to the negative ion resonance (NIR). Calculated STM images of the HOMO and LUMO at $z_0 = 4.5$ Å obtained using the Tersoff-Hamann approach for an s -wave tip (c) and (d), a p -wave tip (e) and (f) and a sp -wave mixed tip (g) and (h). Figure adapted with permission from Ref. [40].

metal LDOS near E_F and resulting, owing to the associated energy cost, in a repulsive force between D_2 and metal. Consequently, the contrast in these images can be interpreted as a two-dimensional mapping of the short-range Pauli repulsion. In practice, when the tip moves, for example, from the center of a carbon ring to a position above a carbon atom, the increased electron density on the atom will push the D_2 molecule closer to the tip, depleting the tip DOS and thus lowering the conductance. As a result the carbon atoms appear darker in the images. This technique also allows the imaging of intermolecular bonds [42]. The same kind of force sensor giving intramolecular resolution can be obtained using Xe, CO or CH_4 to decorate the tip apex [43]. In the case of CO molecules the enhanced contrast, allowing for the imaging of the molecular orbitals of molecules adsorbed on insulating surfaces, was ascribed also to p -wave tip contributions, owing to tunneling through the π orbitals of the CO-decorated tip [40]. STM images simulated with such sp -wave mixed tips, Fig. 1.3, show a very good agreement with experimental results.

1.1.3 The experimental setup

All the STM measurements presented in this work have been performed using a home-built low temperature (LT) STM working at the liquid helium (5 K), solid nitrogen (50 K) or liquid nitrogen (78 K) temperature in ultra high vacuum (UHV) [44, 45]. The instrument can also be used to perform plasmon enhanced light-emission measurements [46, 47], although this potentiality was not exploited in this thesis work.

The STM head is placed into a system of two cryostats, consisting of an inner dewar that can be filled with liquid helium or liquid nitrogen, which in turn can be solidified by pumping, and an outer dewar filled with liquid nitrogen, acting as a thermal screen for the inner one. Thanks to a set of holes in the rotating shields of the inner cryostat, it is possible to perform *in situ* evaporation of metal on the sample at a temperature of 10 K. We can anneal the sample at different temperatures; even though the sample temperature is not directly measured, we can infer it from the temperature inside the inner cryostat or with indirect methods. Turning the cryostat shields so that the openings match brings the sample to a temperature of 18 K, which can be increased to 20 K if a light is shone on the STM head through the vacuum window. Keeping the sample out of the cryostat for one minute results in an annealing to \approx 50 K, estimated from the observation that after such a treatment on a Xe/HOPG sample the second Xe layer desorbs, while the first one does not [48]. Annealing at room temperature is performed by putting the sample, out of the cryostat, in contact with a metallic part of the instrument for five to ten minutes.

The base pressure in the STM chamber is 1×10^{-10} mbar, however when the cryostat is cooled at the liquid helium temperature the pressure inside it is lower than 10^{-14} mbar [44]. An adjacent chamber is equipped for sample preparation, with possibility of performing sputtering and annealing and of evaporating atoms or molecules. During deposition the sample can be mounted on a cold finger connected to a small tank filled with liquid nitrogen in order to cool it from room temperature down to \approx 140 K; a thermocouple reads the cold finger temperature. The flux of evaporated atoms or molecules is estimated *a posteriori* from the coverage observed on STM images and from the evaporation time. The base pressure

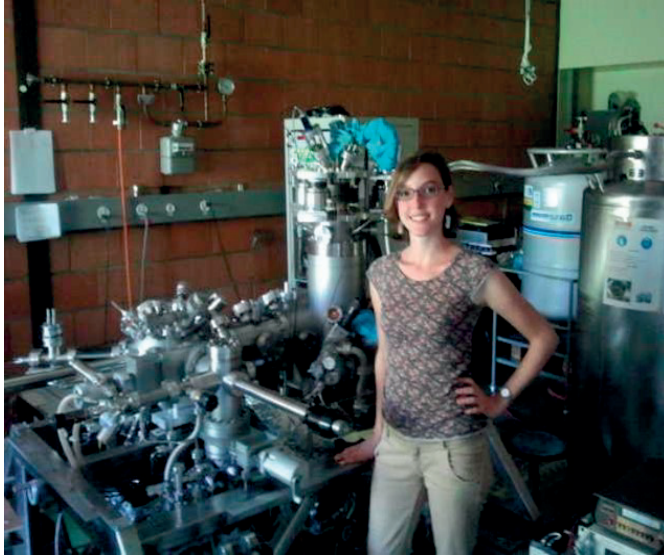


Figure 1.4: The LT UHV scanning tunneling microscope.

in the preparation chamber is 1×10^{-10} mbar. The STM controller and the software are a commercial Omicron SCALA system.

All measurements presented in this thesis are performed at a measuring temperature $T_{\text{meas}} = 5$ K, unless differently specified. In all STS measurements the voltage modulation refers to peak-to-peak values; differential conductance maps are extracted from a grid of 32×32 point spectra.

1.2 Measuring magnetic properties: XAS and XMCD

Up to this point, we have described techniques that allow for a local investigation of the morphology and of the electronic properties of the sample. When one wants to probe magnetic properties, spin excitation spectroscopy performed with the STM can give access to zero-field splitting and to magnetic anisotropy. However, space averaging synchrotron techniques are the techniques of choice to reveal the orbital and spin magnetic moments, as well as the electronic ground state and the magnetic anisotropy in an element specific way. They are thus a valuable complement to STM measurements. I will give here a very simple description of these methods.

X-ray Absorption Spectroscopy (XAS) and X-ray Magnetic Circular Dichroism (XMCD) [49, 50] are powerful techniques for the study of magnetic properties of materials, as they are element specific and highly sensitive, making it possible to study magnetic impurities with very low concentrations. They work thanks to the resonant absorption of photons with energy in the soft x-ray range. The orbital and spin magnetic moments can be obtained from the measured spectra using the sum rules derived by Thole and Carra [51, 52], and from XMCD measurements magnetization curves can be deduced. From angular dependent XMCD measurements as a function of the applied magnetic field it is possible to determine the Magnetic Anisotropy Energy (MAE), which is a key parameter for obtaining stable magnetization, since

its magnitude determines the probability of thermally induced magnetization reversal [53]. The absorption of circularly polarized light by a magnetized sample depends on the orientation of the sample magnetization with respect to the light polarization direction. In this simple description we will refer to excitations from $2p$ to $3d$ electronic levels as observed in transition metals, which will be a useful introduction to the results presented in Chapters 6 and 7, where systems with Fe will be investigated, while in Chapter 4 we will present results about a rare-earth element, Er, thus with excitations from $3d$ to $4f$ levels.

Right (R) or left (L) circularly polarized photons (corresponding to parallel - positive - or antiparallel - negative - photon helicity with respect to the light propagation direction) are absorbed by core electrons. As a consequence of angular momentum conservation, they transfer their angular momentum, respectively $\Delta m = \pm 1$, to the excited electron. If the electron comes from a spin-orbit split level the angular momentum can be in part transferred to the spin, and R and L photons excite photoelectrons with opposite spin polarization. Since the $p_{3/2}$ and $p_{1/2}$ levels have opposite spin-orbit coupling, respectively $l + s$ and $l - s$, at the two edges L_3 and L_2 the spin polarization will be opposite.

If the sample has a net polarization, the empty states will have predominantly minority spin character, and as a result the favored transitions will be the ones that involve initial states with predominant minority spin character. Thus the final states act as a spin filter for the excited photoelectron. A schematic representation of x-ray absorption at the L_2 and L_3 edges is shown in Fig. 1.5(a), and an example of XAS and corresponding XMCD spectra are shown in Fig. 1.5(b). The solid line corresponds to the configuration where sample magnetization and light polarization are parallel, the dashed line to the one where they are antiparallel. The corresponding adsorption coefficients are called, respectively, μ_+ and μ_- . The orbital and spin magnetic moments, μ_L and μ_{S+7T} , can be obtained from the measured spectra using the sum rules:

$$\mu_L = -\frac{4}{3} h_d \frac{\int_{L_3+L_2} (\mu_+ - \mu_-) dE}{\int_{L_3+L_2} (\mu_+ + \mu_-) dE} \quad (1.7)$$

$$\mu_{S+7T} = -h_d \frac{6 \int_{L_3} (\mu_+ - \mu_-) dE - 4 \int_{L_3+L_2} (\mu_+ - \mu_-) dE}{\int_{L_3+L_2} (\mu_+ + \mu_-) dE} \quad (1.8)$$

The XMCD signal is obtained as the difference between μ_+ and μ_- and is proportional to the majority-minority spin imbalance in the $3d$ states above E_F , in other words it's proportional to the sample magnetization.

The experiments presented in this thesis were performed at the EPFL/PSI X-Treme beam-line [54] at the Swiss Light Source. The end-station includes a chamber for the sample preparation equipped with an STM, from which samples can be transferred into the cryostat for XAS and XMCD measurements without breaking the vacuum. For this thesis, we used a measuring temperature of 2.5 K and a magnetic field of 6.8 T applied along the beam direction; measurements were performed in the total electron yield mode and XAS spectra were normalized to the intensity of the x-ray beam measured on a metallic grid placed upstream

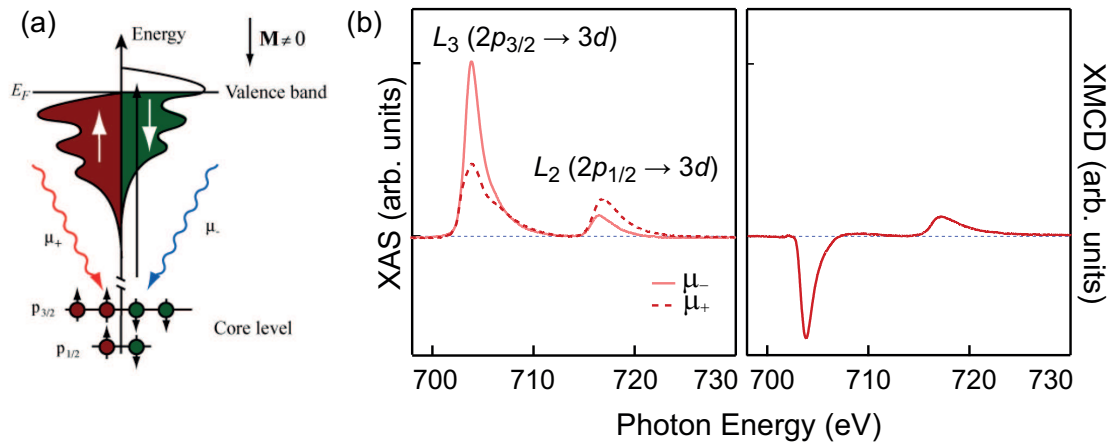


Figure 1.5: (a) Schematic representation of x-ray absorption at the L_2 and L_3 edges. (b) XAS and XMCD spectra at the Fe $L_{2,3}$ absorption edges for the 0.145 monolayers of Fe on Cu(111). Spectra were measured at $T = 2.5$ K, with magnetic field $B = 6.8$ T and with the sample normal aligned with the direction of the field.

of the sample. Rotation of the sample from a position with the beam parallel to the surface normal to one rotated by 60° was used for the acquisition of spectra in normal and grazing incidence, respectively. The base pressure in the XMCD chamber cooled at the liquid helium temperature is in the low 10^{-11} mbar range. The presence of an STM in the endstation gives the possibility to check the sample quality before XAS and XMCD measurements, which is particularly important for samples that require a relatively complicated preparation, as the one where organic molecules and Fe atoms are codeposited that is presented in Chapter 7.



Part I:

Molecular Self-Assembly

2 NC-Ph_n-CN/Cu(111): Deposition @ RT

2.1 Introduction

Thanks to self-assembly, complex structures can be created in a simple way; the process is driven by the information intrinsically contained in the building units and, in the case of surface-supported self-assembly, in the substrate. The reversibility of the interactions governing the process, as hydrogen bonding, van der Waals and metal-ligand interactions, results in the possibility of correcting errors in the assembly, so that the resulting structures can be highly regular.

The use of molecules containing functional groups, such as carboxyl [55, 56, 57], thiol [58], pyridyl [59, 60, 61] or carbonitrile [62, 63, 64], that are capable of coordination with metal atoms (Fe, Co, Mn, Cu...), gives the opportunity to create stable networks, since metal-organic bonds are stronger than those acting in purely organic supramolecular assemblies [25, 27]. However, in the absence of metal adatoms, the same functional groups can participate in the formation of hydrogen bonds [55, 65]. In this chapter we will discuss networks formed by cyano-terminated molecules with coordination Cu adatoms; in the following one we will explore the assemblies formed without them. Coordinated bonds between Cu atoms and N-containing groups have been reported, for example, for molecules comprising pyridyl groups co-deposited with Cu adatoms on HOPG [66, 67] or Au(111) [68, 69]. At sufficiently high temperature, however, copper substrates can spontaneously supply adatoms for coordination [59, 70, 63, 71, 72, 73, 74, 64, 61].

Most of the work presented in this thesis revolves around two molecules: NC-Ph₅-CN and NC-Ph₃-CN [62], pictured in Fig. 2.1. They are linear polyphenyl molecules terminated with a cyano group, differing only in the number of phenyl rings, five and three respectively. They were custom synthesized by the group of Mario Ruben, from the Forschungszentrum of Karlsruhe.

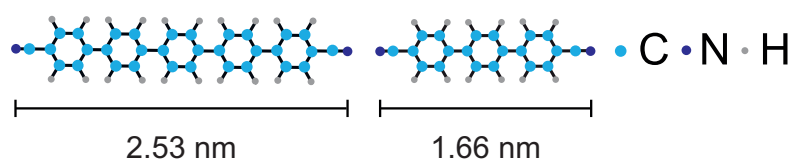


Figure 2.1: Structure of NC-Ph₅-CN and NC-Ph₃-CN.

In this chapter we will focus on the assemblies obtained evaporating the molecules on the Cu(111) surface kept at room temperature (RT). To extend the characterization of the observed metal-organic structures, we also report spectroscopic data for the molecular orbitals in the different assemblies. Finally, we discuss the dependence of the obtained structures on the molecular coverage and the patterns obtained upon codeposition of the two molecules.

Both NC-Ph₅-CN and NC-Ph₃-CN molecules deposited on Cu(111) at RT form metal-coordinated chain and honeycomb structures, thanks to the 2D gas of Cu adatoms that is present on the surface, as discussed in the next paragraph. However, the organization of the molecules is not the same in the two systems and there are some interesting differences between the obtained assemblies. The study of these self-assembled structures gives important insight into the hierarchy of the different interactions determining the self-organization of molecules on the substrate; as we shall see, the different number of phenyl rings in the two molecules results in the prevalence of different interactions in the determination of the molecular assemblies.

Density of Cu adatoms on Cu(111)

Cu(111) is an interesting substrate for studying molecular self-assembly, as a two-dimensional gas of Cu adatoms is present on the surface and can thus provide coordination centers to the molecules, allowing the formation of metal-organic networks. As the amount of available adatoms depends on the substrate temperature, changing the molecule deposition conditions significantly affects the properties of the obtained assemblies, as we will see in this and in the following chapter. To be more precise, the amount of Cu adatoms found on the surface is the result of an equilibrium between attachment and detachment processes at the kinks, and it is determined by the temperature, by the energy barrier for diffusion and detachment and by the density of steps and kinks on the surface.

The energy required for the detachment of an adatom from a kink and for its diffusion on a terrace has been determined experimentally to be 0.78 ± 0.04 eV from Cu adatom island decay [75], and 0.76 ± 0.15 eV from temperature dependent step fluctuations [76]. These values are in agreement with the theoretical one, 0.85 eV, obtained by density functional theory calculations [77]. For the attempt frequency, the typical value used for the pre-exponential factor is $\nu_0 = 10^{12} \text{ s}^{-1}$ [78], but a value of $1.6 \times 10^{10 \pm 1.7} \text{ s}^{-1}$ has also been reported [76]. Taking into account a kink density of $\approx 1 \times 10^{-3}$ ML, consistent with our data for the Cu(111) substrate, a deposition time of 300 s and a time interval before the sample complete cool down to the measuring temperature of 5 K of approximately ten minutes, we find with the parameters reported in Ref. [76] an adatom density of the order of 3×10^{-3} ML at room temperature. With the energy barrier of 0.78 ± 0.04 eV [75] and $\nu_0 = 10^{12} \text{ s}^{-1}$, an adatom density of 8×10^{-2} ML is obtained. These values are compatible, as we shall see, with the density of Cu coordination adatoms that we estimate from our measurements. It is thus not necessary to hypothesize an active role of the molecules in the detachment of the Cu adatoms from step edges as it was previously suggested [72].

Experimental details

For all samples, the Cu(111) surface was prepared by Ar⁺ sputtering ($2 \mu\text{A}/\text{cm}^2$, 800 eV, 20 min) and annealing (800 K, 20 min) cycles and the molecules were evaporated from a molecular effusion cell at 503 K and 418 K for the long and the short ligands, respectively. All measurements, if not differently specified, were performed at $T_{\text{meas}} = 5$ K. In all STS measurements the voltage modulation refers to peak-to-peak values and the differential conductance maps are extracted from a grid of 32×32 dI/dV spectra. The presented point spectra are the average of several spectra measured on equivalent locations.

2.2 NC-Ph₅-CN

When the Cu(111) temperature during molecular deposition (T_{dep}) is 300 K, NC-Ph₅-CN form two assemblies: one-dimensional chains and a two dimensional honeycomb network. We define one monolayer (ML) of molecules based on the denser assembly this molecules form: the compact structure that is observed upon measuring at RT and that is described in Section 2.2.3. The amount of molecules evaporated on the surface is, if not differently specified, 0.4 ± 0.1 ML.

2.2.1 Chain assembly

Figure 2.2(a) shows an overview of the chain assembly. The surface is covered by a homogeneous layer of one-dimensional chains. In this image it is possible to distinguish two rotational domains, and in total three domains, rotated by 120° with respect to one another, can be found, owing to the symmetry of the underlying substrate. The chains are not perfectly organized, as it can be observed in Fig. 2.2(b), where some defects in the assembly are indicated, like molecules aligned along directions that are not the dominant ones (highlighted in the white ellipses) or of nodes with coordination three (green circle). The chains follow the second nearest neighbors directions of the substrate, $\langle 11\bar{2} \rangle$. However, looking at this image one can note that they are not perfectly straight, but rather have a wavy appearance. This waviness can be understood considering the epitaxy of the molecules and of the Cu adatoms on the surface, illustrated in Figure 2.3 and discussed in the following paragraph.

Epitaxy of molecules and adatoms on the surface

In general, the adsorption of molecules on the surface and their assembly are controlled by several competing interactions [80, 81, 82]. For the case of interest for us, that of metal-organic porous networks, there are the forces acting directly on the molecules, the van-der-Waals forces between molecules and surface and the migration and rotation barriers felt by the molecules. Then there is the interaction of the metal coordination atoms with the substrate, through the potential energy surface felt by the atoms, *i.e.*, their preferred adsorption sites and their diffusion barriers. Finally, there are the bond angle, the distance and the coordination number of the metal-organic coordination bond. The registry of the molecules with the substrate clearly favors alignment along the $\langle 11\bar{2} \rangle$ directions, since the distance between consecutive phenyl rings, 4.410 \AA [62], is very close to the one between two Cu atoms in the $\langle 11\bar{2} \rangle$ directions, 4.427 \AA [83], allowing all phenyl rings to occupy equivalent sites, as seen in

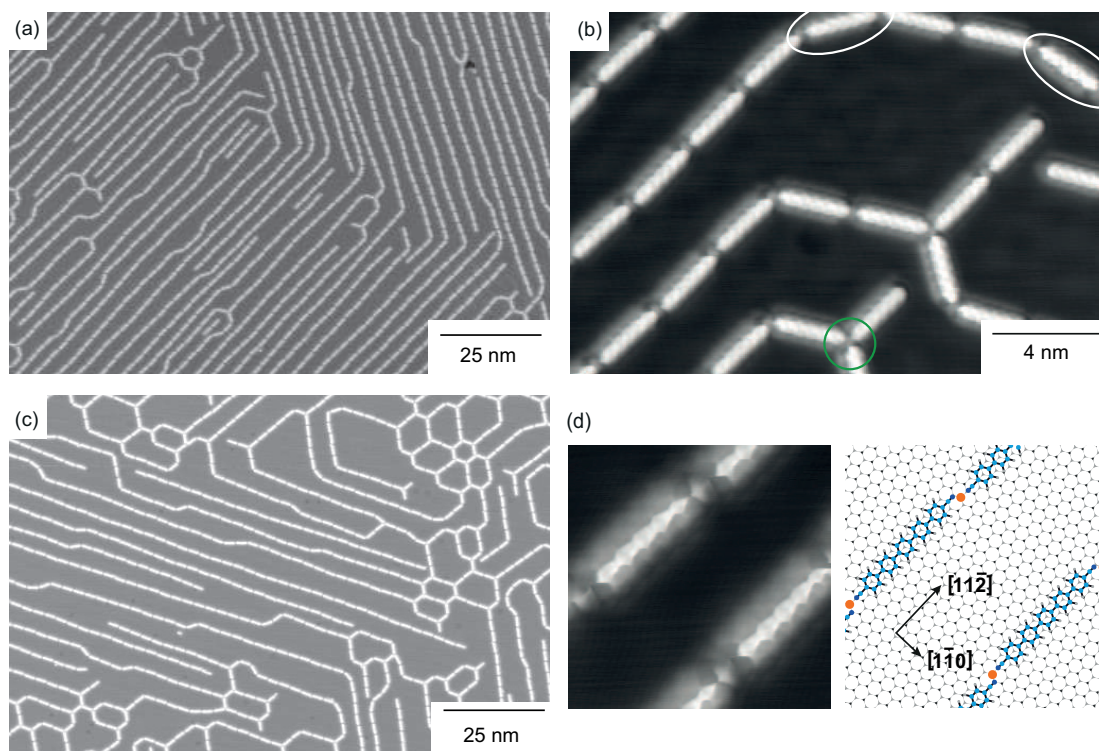


Figure 2.2: NC-Ph₅-CN chain assembly, $T_{\text{dep}} = 300$ K. (a) STM image of chain domains, 0.4 ML of molecules ($V_t = -200$ mV, $I_t = 20$ pA). (b) Close-up view of the chains ($V_t = -5$ mV, $I_t = 20$ pA). The white circles indicate molecules that deviate from the $\langle 11\bar{2} \rangle$ directions, the green circle surrounds a threefold node. (c) Assembly obtained by depositing 0.25 ML of molecules ($V_t = -200$ mV, $I_t = 20$ pA). (d) STM image showing the nodes and relative model ($V_t = -2$ mV, $I_t = 20$ pA). Adapted with permission from our paper, Ref. [79].

Fig. 2.3. These are the three-fold hollow sites, the preferred sites for benzene rings [84, 85]. In addition, this adsorption geometry permits to half the hydrogen atoms of the molecule to be located on their preferred fcc adsorption sites [86, 87]. Finally, in this configuration the N atoms are on hollow sites, that were reported to be favorable on Ag(111) [88]. The second part of the total energy comes from the positions of Cu adatoms and their bond distance and

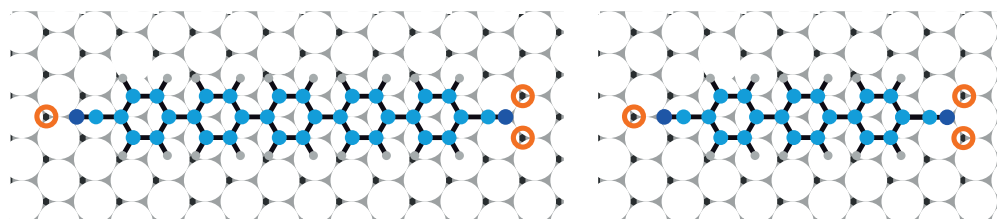


Figure 2.3: Model showing a NC-Ph₅-CN and a NC-Ph₃-CN molecule aligned along the $\langle 11\bar{2} \rangle$ direction of the Cu(111) surface. The orange circles indicate the possible positions of the Cu coordination adatoms.

angle to the terminal carbonitrile groups. Cu adatoms preferentially adsorb on fcc sites. DFT finds that the hcp and bridge sites are unstable [89], which would favor the fcc site by the diffusion barrier that amounts to 40 ± 1 meV [90]. In agreement, experiment observes exclusive occupation of fcc sites [91]. The result is that, as seen in Fig. 2.3, at one end of the molecule the adatoms is laterally displaced and can adsorb in two equivalent positions. However, the bond between a metal atom and the carbonitrile group is strongly directional along the CN axis. [92], thus energetically this lateral bond is unfavorable compared to a straight one. For NC-Ph₅-CN molecules the interaction between the molecules and the substrate dominates over the directionality of the metal coordination bond and the registry of the metal atoms with the surface. We will see later that for NC-Ph₃-CN the opposite is true.

Thus NC-Ph₅-CN molecules adsorb along $\langle 11\bar{2} \rangle$ and have one adatom aligned with the molecular axis, the other one laterally displaced. In the chain assembly, the different alignment of the Cu adatoms at the two ends of the molecules can be observed on the close-up image shown in Fig. 2.2(d). This image was obtained with a CO functionalized tip giving intramolecular contrast, so that the five phenyl rings are visible, and allowing the imaging of the Cu adatoms. The projected Cu-N bond length obtained from the model shown along with the image is 1.9 ± 0.2 Å, a value comparable with what was found for the same linkers with Co coordination adatoms on Ag(111) (1.6 Å [62] - 1.8 Å [93]) and for bipyridyl molecules coordinated by Cu atoms on Cu(100) (1.9 Å [59]). For this assembly we estimate an adatom density of, at most, 6×10^{-3} ML. The average distance between two neighboring chains is 3 ± 1 nm and hints toward the presence of a lateral repulsion between the molecules, as demonstrated by the fact that at lower coverages the chains are further apart from each other, see Fig. 2.2(c), while for higher coverages a more compact, 2D honeycomb network is formed, as presented in the following section. Probably, the origin of this repulsion lies in a charge transfer between the molecules and the substrate, as it was reported for other systems [94, 95, 90]. The coverage dependence of the chain distances leads to the exclusion of a surface state mediated interaction, as in that case the chain separation would be constant.

2.2.2 Honeycomb network

Coexisting with the chain assembly, a highly regular honeycomb network is observed on the surface. If T_{dep} is slightly decreased to 250 K, or if the molecular coverage is slightly increased, this structure becomes the dominant one, covering practically the whole surface. Fig. 2.4(a) shows an overview of this network, where two domains are visible, forming an angle of 5° with respect to each other. The origin of the existence of two different domains lies again in the alignment of the Cu adatoms with the molecular ends. Indeed, on the side of the ligand where the atom is aligned with the molecular axis, a straight node is formed, while on the other side the laterally aligned atom becomes the center of a rotated node. The rotation can be with equal probability clockwise or anticlockwise, giving rise to the two domains. We can thus speak of chiral domains, as they arise from the presence of chiral nodes. The aligned and rotated nodes can be discerned in the images, as seen in Fig. 2.4(b) (green and pink circles,

respectively), and they alternate at the corners of each hexagon. A high resolution image of the two kinds of nodes is displayed in Fig. 2.4(c), accompanied by the proposed model.

The unit cell of this network, sketched in Fig. 2.4(b), can be expressed in matrix notation as:

$$\begin{pmatrix} \mathbf{b}_1 \\ \mathbf{b}_2 \end{pmatrix} = \begin{pmatrix} 19 & 1 \\ -1 & 20 \end{pmatrix} \begin{pmatrix} \mathbf{a}_1 \\ \mathbf{a}_2 \end{pmatrix}$$

where \mathbf{a}_1 and \mathbf{a}_2 are the unit cell vectors of the Cu(111) surface, respectively. We find $|\mathbf{b}_1| = |\mathbf{b}_2| = 4.99$ nm. The experimental value for the periodicity, defined as the distance between parallel molecules in a given hexagon, is 4.97 ± 0.04 nm. The model yields an angle between the two domains of 5.08° and a density of adatoms of 5.2×10^{-3} ML. The density of molecules in this network is higher than for the chains, suggesting that coordination two is energetically favored, but when the density of molecules increases, or when the amount of available adatoms decreases, coordination three dominates, allowing for a denser structure with a

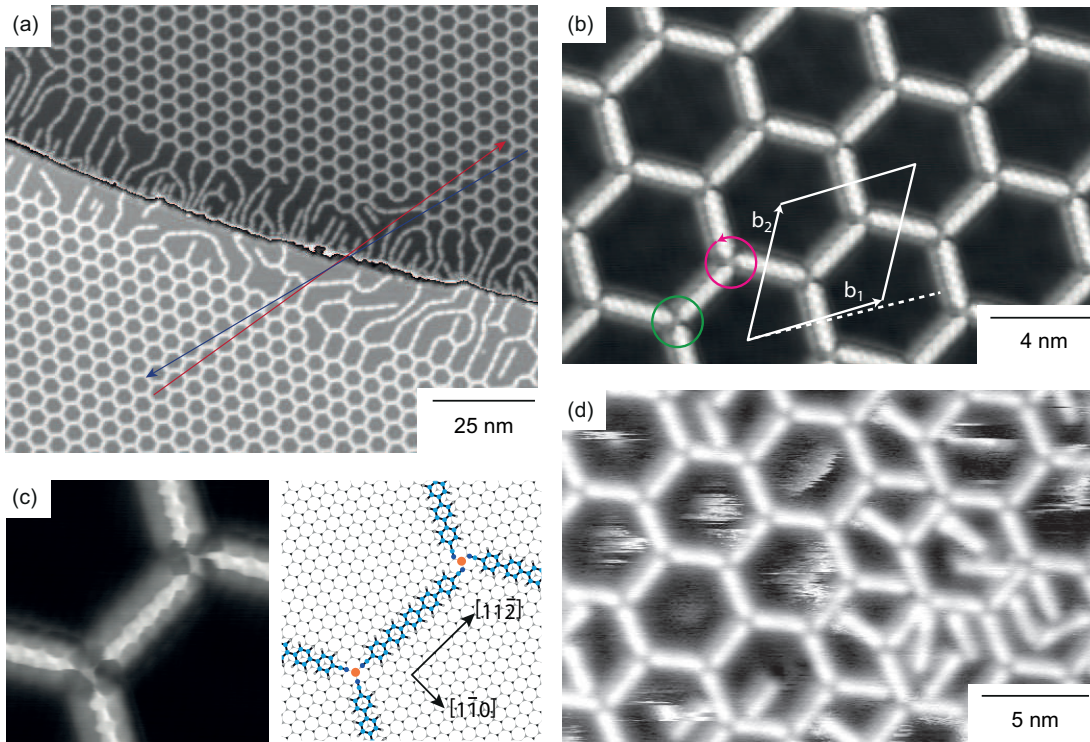


Figure 2.4: NC-Ph₅-CN honeycomb network, $T_{\text{dep}} = 250$ K. (a) Overview of the honeycomb network, 0.4 ML of molecules. The two islands correspond to the two chiral domains ($V_t = -25$ mV, $I_t = 20$ pA). (b) Close-up view of the assembly measured with a CO functionalized tip. The unit cell is indicated. Green circle: aligned node; pink circle: rotated node ($V_t = -5$ mV, $I_t = 20$ pA). (c) Detail of the structure of the nodes imaged with a CO functionalized tip showing the Cu adatoms, accompanied by the corresponding model ($V_t = -2$ mV, $I_t = 20$ pA). (d) Pattern formed by depositing 0.5 ML of molecules ($V_t = -150$ mV, $I_t = 20$ pA, $T_{\text{meas}} = 50$ K). Adapted with permission from our paper, Ref. [79].

smaller number of adatoms. Upon increasing of the molecular coverage to 0.5 ML we observe a honeycomb network having most of the cavities occupied by guest molecules, as seen in Fig. 2.4(d). The presence of the extra molecules also induces defects in the pattern.

2.2.3 Measurements @ RT: compact structure

Deposition and imaging at 300 K leads to the formation of a very dense molecular structure. The molecules form a compact assembly composed of parallel chains, shown in Fig. 2.5. The structure is rather unstable and very sensitive to the tunneling parameters. The sample is not completely covered by molecules and regions of bare Cu(111) substrate are present. The regular parts of the assembly have a rectangular unit cell with periodicity of 2.8 ± 0.2 nm and 1.3 ± 0.1 nm in the directions parallel and perpendicular to the chains, respectively.

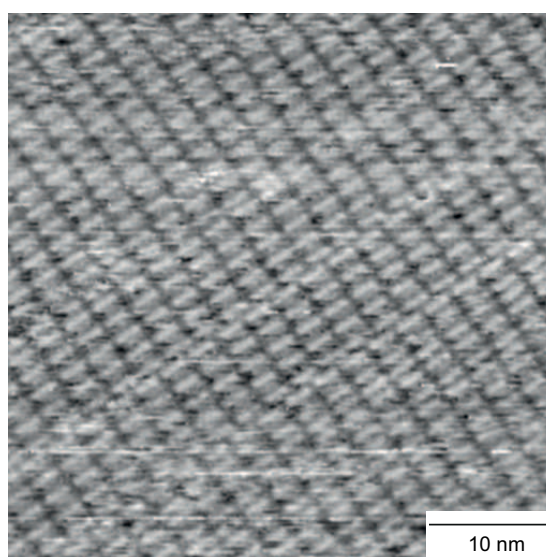


Figure 2.5: NC-Ph₅-CN compact structure, $T_{\text{dep}} = 300$ K, $T_{\text{meas}} = 300$ K. STM image of the assembly ($V_t = +1.4$ V, $I_t = 100$ pA). Adapted with permission from our paper, Ref. [79].

These chains have the same periodicity along the chain direction as the ones shown in Section 2.2.1, for which we know that Cu coordination atoms are present. Therefore we deduce that the molecules coordinate thanks to Cu atoms also in this compact structure. This interpretation is supported by the comparison with the dense-packed structure reported for NC-Ph₆-CN on Ag(111) [96], where in the absence of coordination atoms the molecules are not aligned, but rather the CN groups interdigitate, in line with the fact that two cyano groups repel each other.

The formation of this compact structure at 300 K indicates that at this temperature the prevailing interactions are different from the ones leading to the formation of the chains observed after cooling the sample. The mutual repulsion observed in the chain structure measured at 5 K is here clearly absent, indicating a different interaction with the surface and between the molecules. Unfortunately, our observations are not sufficient to precisely identify the interactions playing a major role in this assembly. It is also possible that at room temperature

some degrees of freedom, for example the tilting of the phenyl rings with respect to each other, are present while being inhibited at low temperature.

2.2.4 Spectroscopy on the honeycomb network

Scanning tunneling spectroscopy was used to probe the unoccupied orbitals of molecules in the honeycomb network. The differential conductance spectra acquired on different locations over a molecule (shown in the inset) are displayed in Fig. 2.6(a). The Lowest Unoccupied Molecular Orbital (LUMO) is situated at 1.3 eV and has its maximum intensity at the center of the molecule (red line) while the next orbital, the LUMO+1, is found at an energy of 1.7 eV and is localized at the molecular ends and at the nodes (blue curve). The LUMO+2 has again maximum intensity at the center of the molecule, and its energy is 2.5 eV. We cannot observe orbitals that lie higher in energy because of an experimental limitation of ≈ 2.5 V imposed by network damage at higher voltages. Interestingly, there is no difference between

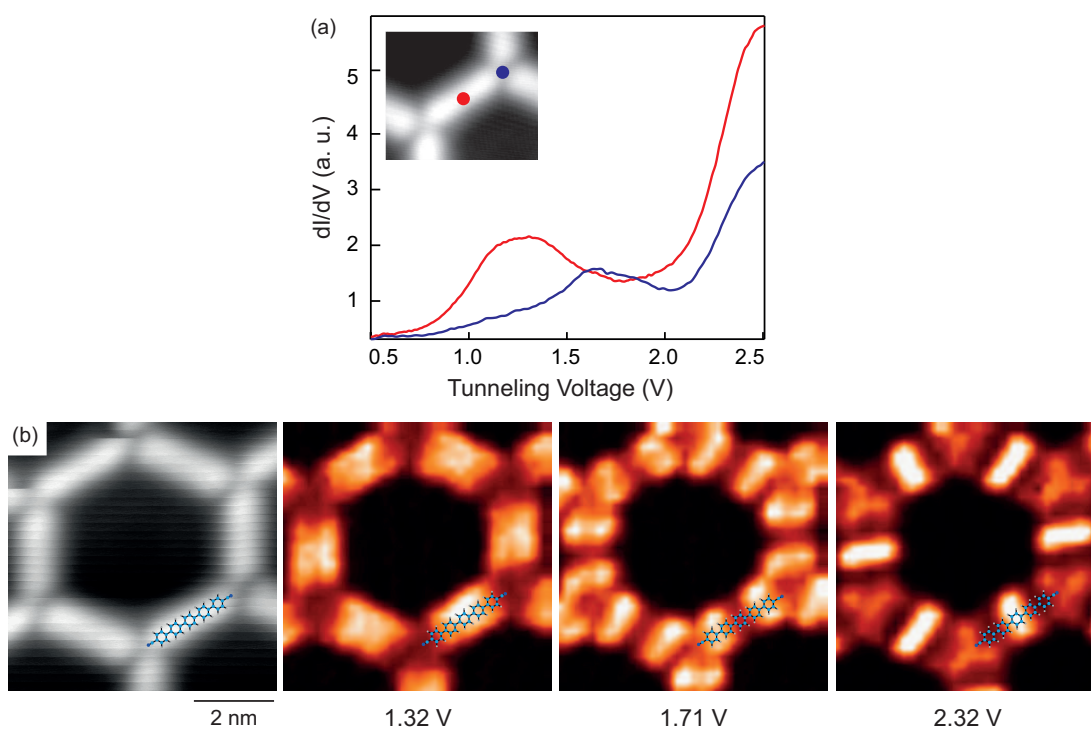


Figure 2.6: NC-Ph₅-CN: spectroscopy on the honeycomb network. (a) dI/dV spectra acquired on the center of the molecule (red) and on a node (blue) as shown in the inset. (b) Topography and corresponding STS maps recorded at 1.32 V, 1.71 V and 2.32 V (setpoint: $V_t = +500$ mV, $I_t = 20$ pA, $V_{\text{mod}} = 10$ mV at 483 Hz). One molecular backbone is overlaid for comparison.

the spectra acquired on the aligned and on the rotated nodes. STS maps are shown along with the corresponding topography in Fig. 2.6(b). We can immediately see that the lateral extension of the molecular orbitals goes far beyond the width of the molecules. The map recorded at 1.32 eV reproduces the LUMO, which is extended on the whole molecule and does not show nodal planes. At 1.71 eV we see the LUMO+1, whose intensity is concentrated

at the molecular ends and that has a nodal plane cutting across the center of the molecule perpendicularly to the axis. The LUMO+2, at 2.32 eV, clearly has an intensity maximum on the center of the molecule, plus some intensity over the ends of the molecules. This orbital exhibits two nodal planes perpendicular to the ligand axis. These features of the orbitals agree well with a qualitative description of the electronic structure derived by considering the molecule as a linear chain of three benzene rings [97].

2.3 NC-Ph₃-CN

NC-Ph₃-CN deposited on Cu(111) at $T_{\text{dep}} = 300$ K also form chain and honeycomb structures. For these molecules, we define one monolayer as the densest structure they form on Cu(111), *i.e.* the purely organic chevron pattern that is shown in Fig. 3.9. When not differently specified the molecular coverage is 0.30 ± 0.03 ML. At this coverage about half of the surface is covered with equidistant chains. The rest of the surface is covered by the honeycomb network.

2.3.1 Chain assembly

A large scale image showing the molecules arranged in parallel equidistant chains is displayed in Fig. 2.7(a). Two rotational domains are visible, and the lower left corner shows a small domain of the honeycomb network that will be discussed below. As for NC-Ph₅-CN three different rotational domains exist, forming an angle of 120° with respect to one another, owing to the symmetry of the underlying substrate.

Closer inspection reveals that the chains are not perfectly straight. The close-up view of Fig. 2.7(b) shows that the chains are aligned along $\langle 11\bar{2} \rangle$, however the molecules deviate from this direction: the histogram of orientation angles of the molecular axes with respect to the $\langle 11\bar{2} \rangle$ directions shows two peaks at $+4$ and -4 degrees. We label these directions 1 and $\bar{1}$, respectively. The wavy appearance of the resulting chains can thus be attributed to the alternance of molecules with slightly different orientations. The spacing between two adjacent chains is 2.08 ± 0.07 nm.

Figure 2.7(c) illustrates the epitaxy of the molecules for the relevant orientations of the molecular axis. As we saw for the five ring molecules, the molecule-substrate interaction is optimized when the molecule is aligned along the $\langle 11\bar{2} \rangle$ direction, as in the case of NC-Ph₅-CN, while the bond with the Cu adatoms favors a configuration with both adatoms right in front of the molecules. Because of the fact that Cu atoms adsorb on fcc sites [89, 90, 91], a straight bond at both ends cannot be formed when molecules are oriented along $\langle 11\bar{2} \rangle$. As illustrated in Fig. 2.7(c) the closest directions to $\langle 11\bar{2} \rangle$ allowing the molecule to have the two Cu adatoms in line with the molecular axis are the ones labeled 1 and $\bar{1}$, deviating from the high symmetry direction by $\pm 4^\circ$. This shows that for NC-Ph₃-CN the directionality of the metal coordination bond and the registry of the metal atoms with the substrate dominates over the registry of the organic molecule. The other possible alignments allowing a straight node at each end form angles of $\pm 11^\circ$, $\pm 18^\circ$ and $\pm 25^\circ$ with the second nearest neighbors directions (directions 2, 3 and 4 respectively).

In Fig. 2.7(d) we show a close up view of the chains accompanied by the proposed model. Although Cu coordination adatoms are not imaged, we infer their presence by comparison

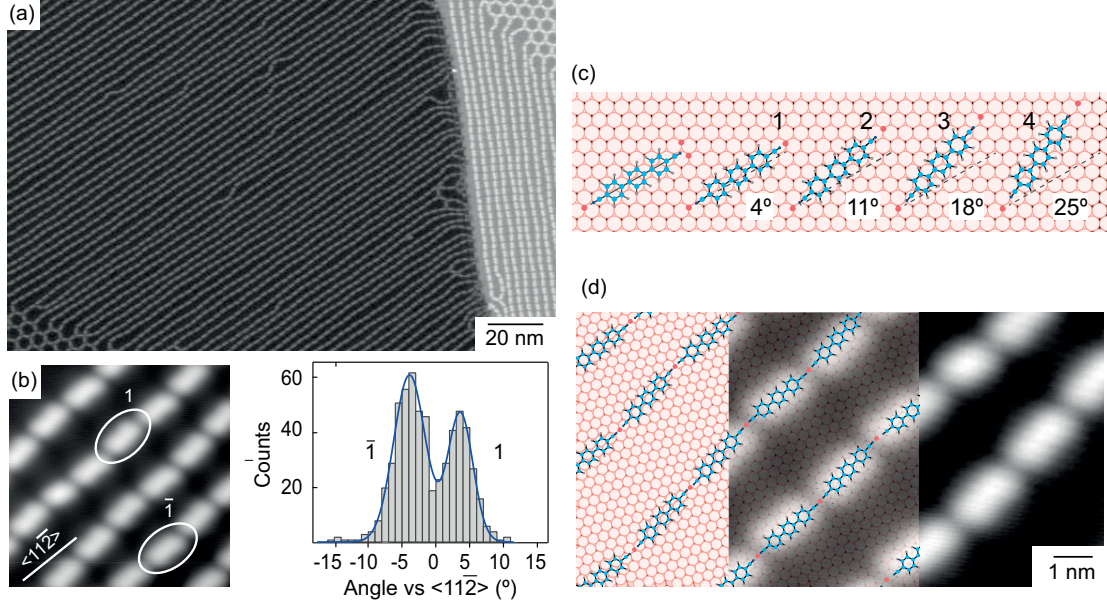


Figure 2.7: NC-Ph₃-CN chain assembly, $T_{\text{dep}} = 300$ K. (a) Large scale image, in which two domains of the chain assembly are visible. (b) Closer view of the chains, with two highlighted molecules that lie in directions 1 and $\bar{1}$ respectively. The histogram shows the distribution of molecular directions, the solid line is a double Gaussian fit to the data. (c) Model showing the possible directions the molecules can have with respect to the substrate, labeled 1, 2, 3 and 4, with the corresponding deviations from the $\langle 11\bar{2} \rangle$ direction (indicated by the dashed line). (d) Close up image and model ($V_t = -200$ mV, $I_t = 50$ pA).

with the networks formed by NC-Ph₅-CN on the same substrate [79] and from the fact that the measured CN-Cu bond length of 1.4 ± 0.1 Å agrees with reported values [62, 59, 93, 79]. The model presented along with the image shows the molecule alternating orientations deviating by $\pm 4^\circ$ from the $\langle 11\bar{2} \rangle$ directions.

2.3.2 Honeycomb network

Coexisting with the chains, we observe two types of honeycomb networks. The first is very regular and is shown in Fig. 2.8, while the second involves more variations between the honeycomb cells and is shown in Fig. 2.9.

The regular network exhibits two rotational domains forming an angle of 22° with respect to one another, see Fig. 2.8(a). A close-up view of each domain is shown in Fig. 2.8(b). These images, obtained with a CO functionalized tip, clearly reveal the three phenyl rings of each molecule and the coordination adatoms. Each of the rotational domains involves molecules that are rotated by $+ \text{ or } -11^\circ$ from the $\langle 11\bar{2} \rangle$ directions, respectively. Figure 2.8(c) shows our model of one domain together with a high resolution STM image. The unit cell for this network is:

$$\begin{pmatrix} \mathbf{c}_1 \\ \mathbf{c}_2 \end{pmatrix} = \begin{pmatrix} 12 & 3 \\ -3 & 15 \end{pmatrix} \begin{pmatrix} \mathbf{a}_1 \\ \mathbf{a}_2 \end{pmatrix}$$

with $c_1 = c_2 = 3.51$ nm.

However, it is more likely for molecules to form a network where different molecular orientations are mixed, producing an overall pattern that is more irregular, presented in Fig. 2.9. This network, an overview of which is shown in Fig. 2.9(a), involves in addition to the orientation 2 (70 % of the molecules) also the orientation 1 (30 %) and very few 3 and 4 defects, as seen from the histogram in Fig. 2.9(b). Also in this case two rotational domains are formed, that are again symmetric with respect to the second nearest neighbors directions.

The four molecular orientations differ not only by their alignment with respect to the substrate, but also by the bond length of the CN-Cu bond. Assuming that the linker length does not change upon adsorption of NC-Ph₃-CN onto the Cu(111) surface, we find a growing projected bond length with increasing deviation from the second nearest neighbor directions, with values of 1.4 ± 0.1 Å, 1.6 ± 0.1 Å, 1.9 ± 0.1 Å and 2.3 ± 0.1 Å for the directions 1, 2, 3 and 4 respectively. The first three values are comparable with the bond length found for the same linkers with Co coordination adatoms on Ag(111) (1.6 Å [62] - 1.8 Å [93]), for bipyridyl molecules coordinated by Cu atoms on Cu(100) (1.9 Å) [59], and for NC-Ph₅-CN molecules coordinated by Cu atoms on Cu(111) (1.9 Å), as seen in Section 2.2.1. The last orientation implies an energetically less favorable very long distance between Cu and NC. We suggest that this difference in bond length has the major contribution to the total energy of the respective molecular orientations. To rationalize the fact that in the chains the favored orientation results in a shorter bond length compared to the one mostly found in the honeycomb, we observe that there is a clear trend linking a decreasing coordination number at the nodes and a

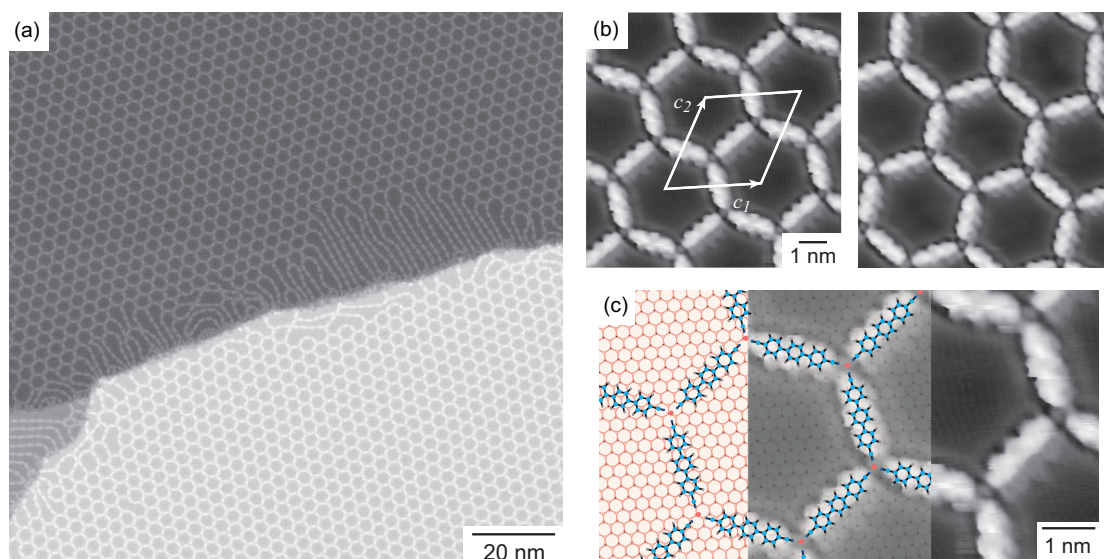


Figure 2.8: NC-Ph₃-CN regular honeycomb network, $T_{\text{dep}} = 300$ K. (a) Overview of the assembly on two Cu(111) terraces separated by a double step; two different rotational domains are formed ($V_t = -600$ mV, $I_t = 100$ pA). (b) High resolution close-up images obtained with a CO functionalized tip. The unit cell is indicated in white ($V_t = -2$ mV, $I_t = 2$ nA). (c) Proposed model with superimposed image.

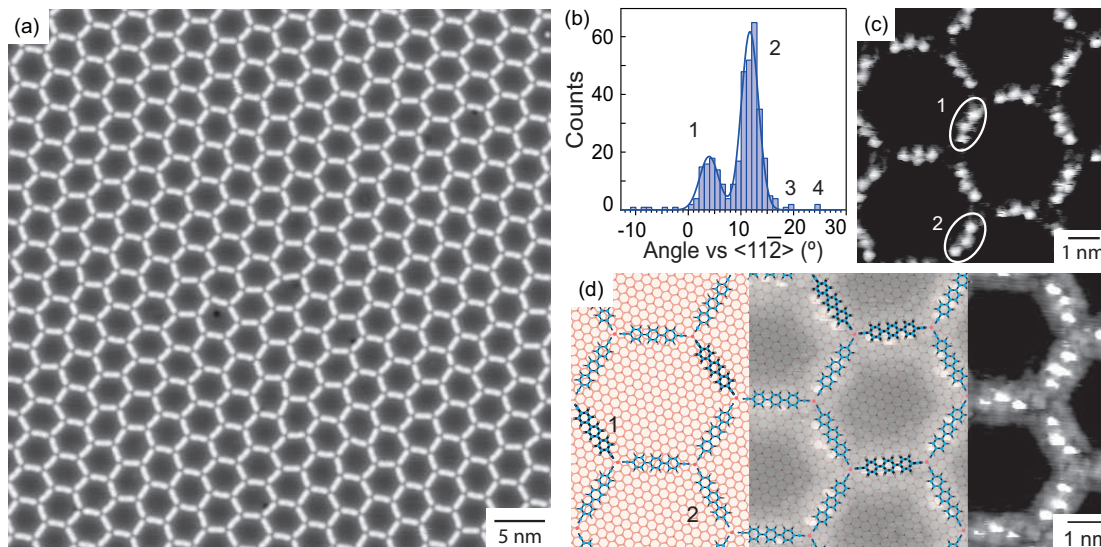


Figure 2.9: NC-Ph₃-CN irregular honeycomb network, $T_{\text{dep}} = 300$ K. (a) Overview of the assembly ($V_t = +20$ mV, $I_t = 200$ pA). (b) Histogram illustrating the distribution of the orientations with respect to $\langle 11\bar{2} \rangle$, solid line: double-Gaussian fit. (c) Small scale image measured with a D₂ functionalized tip with molecules in orientations 1 and 2 highlighted. These molecules appear bent. (d) Detail of the network and structure model. Those molecules with orientation 1 are indicated in bold ($V_t = -10$ mV, $I_t = 100$ pA).

shorter bond length. Reported values include 2.4 Å for NC-Ph₃-CN five-fold coordinated to Ce adatoms on Ag(111) [98], 2.15 Å for TCNQ four-fold coordinated to Mn atoms on Cu(100) [99], 1.9 Å for NC-Ph_n-CN three-fold coordinated to Co atoms on Ag(111) [100], and for NC-Ph₅-CN three-fold coordinated to Cu atoms on Cu(111), Section 2.2.1.

A model for the irregular honeycomb pattern together with a high-resolution STM image measured with a D₂ terminated tip [39, 38] is shown in Fig. 2.9(d), with the molecules aligned along direction 1 represented in bold.

Upon closer inspection, the STM images reveal that NC-Ph₃-CN molecules have a slightly curved appearance. This effect, although seen also in STM images recorded with unfunctionalized tips, is particularly prominent in the images measured dosing D₂ in the STM chamber, as seen in Figs. 2.9(c) and (d). There is a direct relationship between the direction a molecule is aligned along and its apparent curvature; in Fig. 2.9(c) it is possible to see that molecules lying in directions 1 and 2, for example the ones in the circles, have different apparent curvatures with respect to one another. Dicarbonitrile-polyphenyl molecules are known to exhibit an alternating tilt of consecutive phenyl rings, even when they are adsorbed on surfaces [101]. Thus, we suggest that in NC-Ph₃-CN the central ring has a tilt angle with respect to the plane of the other two rings and that its value can change depending on the interaction with the underlying substrate, as was already reported for sexiphenyl molecules on Ag(111) [102]. We ascribe the opposite apparent curvatures of the molecules aligned in directions 1 and 2 to an opposite tilt of the central phenyl ring. We note, moreover, that while for molecules in direction 2 this arc shape is observed for 93% of the ligands, molecules in direction 1 have a

curved appearance only in 46% of the cases, and the curvature is less evident, indicating that in this case the tilt of the central phenyl ring is less pronounced or sometimes even absent.

2.3.3 Coverage-dependent structures

We also investigated molecular coverages below and above the one discussed so far of 0.30 ML. At 0.10 ± 0.01 ML the surface is entirely covered by an irregular network, Fig. 2.10(a). We can assimilate this pattern to widely spaced chains, that frequently bend and meet to form three-fold nodes. By increasing the coverage to 0.24 ± 0.03 ML this structure becomes denser, forming cavities that are smaller, Fig. 2.10(b), approaching the dimension of the honeycomb cavities. Domains of parallel chains coexist with this structure. Their separation is, with 2.47 ± 0.06 nm, larger than the one between the chains coexisting with the honeycomb structure at 0.30 ML. Finally, if the coverage is raised to a value beyond 0.30 ML, namely 0.40 ± 0.04 ML, a very dense pattern is obtained, with four- five- and six-fold nodes, Fig. 2.10(c). This network stems from the need of accommodating a higher number of molecules than in the hexagonal assembly and is strongly irregular. The nodes are probably partly metal-coordinated, partly purely organic.

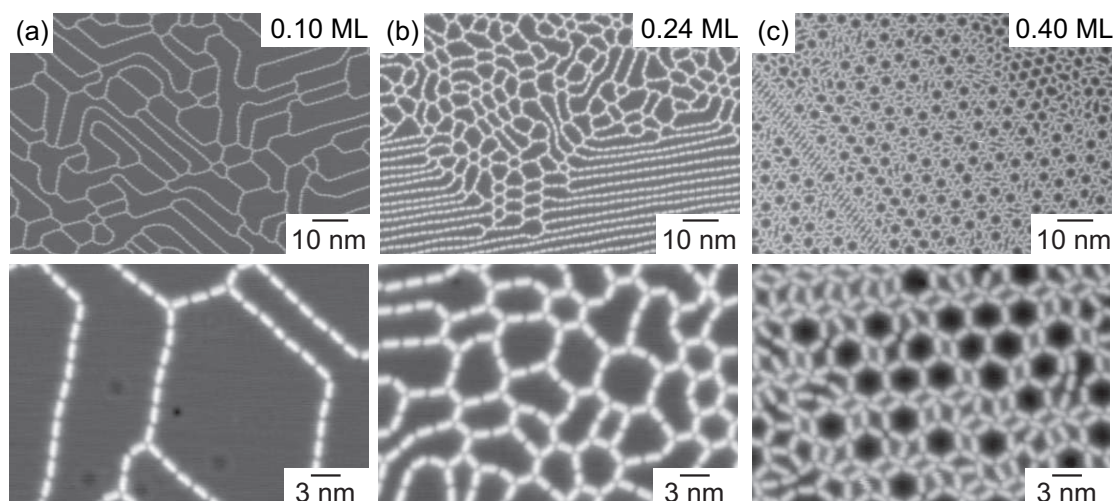


Figure 2.10: Coverage dependence for NC-Ph₃-CN assemblies, $T_{\text{dep}} = 300$ K. (a) 0.10 ± 0.01 ML (b) 0.24 ± 0.03 ML (c) 0.40 ± 0.03 ML ($V_t = -500$ mV, $I_t = 20$ pA).

2.3.4 Spectroscopy on the chain and honeycomb structures

Scanning tunneling spectroscopy was used to probe the unoccupied orbitals of molecules for both the chains and the honeycomb structures. The differential conductance spectra acquired on different locations over a molecule in a chain are shown in Fig. 2.11(a). The LUMO is extended over the whole molecule and has its maximum intensity on the central part of the ligand, slightly off-center (green line) and is situated at an energy of 1.45 eV. The LUMO+1, on the contrary, is localized at the molecular ends and at an energy of 2.30 eV (blue line). In Fig. 2.11(c) differential conductance maps at 1.45 V and 2.31 V are shown along with the corresponding topographic STM image. The presence of a shorter molecule, with only two

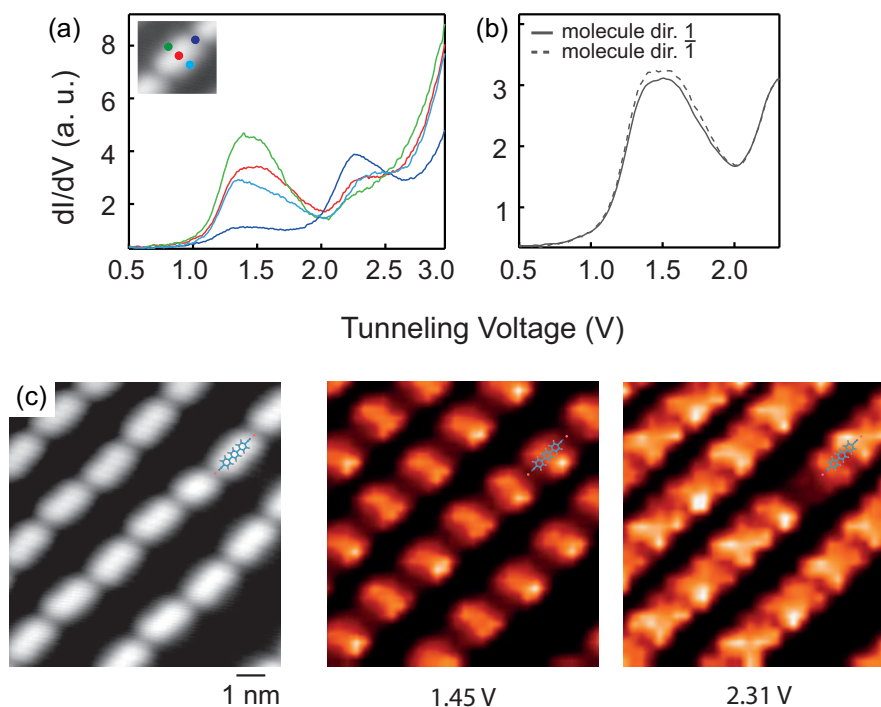


Figure 2.11: NC-Ph₃-CN: spectroscopy on the chain assembly. (a) dI/dV spectra acquired on the locations shown in the inset (red: center of the molecule, green: left side, light blue: right side, blue: node). (b) dI/dV spectra measured on the center of molecules in direction 1 and $\bar{1}$ respectively. (c) Topography and corresponding STS maps at 1.45 and 2.31 V showing the LUMO and LUMO+1 of the molecules, respectively. A molecular backbone is superimposed for comparison (setpoint: $V_t = +500$ mV, $I_t = 10$ pA, $V_{\text{mod}} = 20$ mV at 523 Hz). All spectra are background subtracted.

phenyl rings, is particularly evident in the map representing the LUMO+1, where it appears dark.

Thus, the general features of the molecular orbitals are those of the longer molecules, but the tilt of the central phenyl ring and the presence of molecules having different orientations add some complexity to the picture. In most molecules the LUMO shows a higher intensity on one side. This effect is also seen in the honeycomb networks and will be discussed in detail further below. Figure 2.11(b) compares spectra acquired on the center of two molecules with the two most abundant orientations 1 and $\bar{1}$, respectively, + and -4° with respect to the $\langle 1\bar{1}\bar{2} \rangle$ direction. There is no appreciable difference in the position and intensity of the LUMO, as expected for the two symmetrically equivalent orientations.

The spectra acquired over the molecules in the honeycomb network are presented in Fig. 2.12(a). As in the chains, the LUMO is located at the center of the molecule and has its highest intensity on one side of the molecular axis. The LUMO+1 is also recognized, however its maximum is just beyond the scanned voltage range. As illustrated in Fig. 2.12(b), molecules oriented along direction 1 show the LUMO at 1.45 eV, consistently with the result obtained for ligands in the chain assembly, while the LUMO of molecules lying in direction 2 is shifted upwards, to

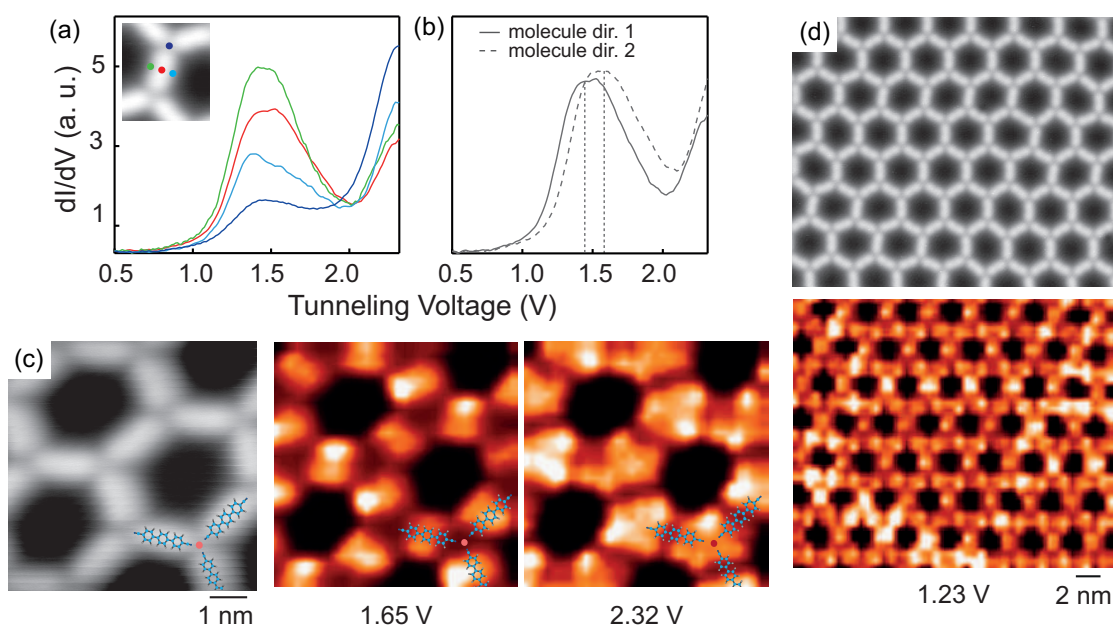


Figure 2.12: NC-Ph₃-CN: spectroscopy on the irregular honeycomb network. (a) dI/dV spectra acquired on the locations shown in the inset (red: center of the molecule, green: left side, light blue: right side, blue: node). (b) dI/dV spectra measured on the center of molecules in direction 1 and 2. (c) Topography and corresponding STS maps at 1.65 V and 2.32 V. Three molecular backbones are superimposed for comparison. (d) Topography and corresponding STS map at 1.23 V (setpoint: $V_t = +500$ mV, $I_t = 10$ pA, $V_{mod} = 20$ mV at 523 Hz). All spectra are background subtracted.

1.60 eV. Differential conductance maps recorded on a small area of the network are presented in Fig. 2.12(c) along with the corresponding STM image. The first map is recorded at 1.65 V, thus around the energy of the LUMO of molecules with orientation 2. Accordingly, these ligands appear bright while molecules with orientations 1 appear dark. In addition, one clearly sees that the LUMO of the molecules with orientation 2 has the highest intensity on one side of the ligand. The second map, at 2.32 V, shows that the LUMO+1 is located on the ends of the molecules. It merges at the meeting point of three ligands, where it forms triangular shaped bright spots. Fig. 2.12(d) shows a large scale dI/dV map recorded at 1.23 V, together with the topographic image. At this energy the spectra of molecules in direction 1 are more intense than the ones of molecules in direction 2, thus the former can be easily identified from their bright color. This map reveals that, for geometrical reasons, the presence of one molecule in direction 1 tends to generate a row of ligands in that same direction.

We now address the question why the LUMO has its maximum intensity on one side of the molecule and why this is the case for many but not all the ligands, see Figs. 2.11(c) and 2.12(c). The LUMO asymmetry is observed for 73% of the molecules, while for the remaining 27% the intensity of the orbital is highest at the center of the ligand and decreases symmetrically moving away from it to either side. From the finding that the fraction of molecules displaying the LUMO asymmetry is close to the fraction of molecules that appear bent in STM images (80

%), we conclude that the tilt of the central phenyl ring that gives rise to the bent appearance is very likely also the cause of the LUMO asymmetry. For technical reasons, we can't make a one-to-one correlation on a given molecule, since spectra are measured with a tip that is optimized for spectroscopy and not for high-resolution imaging, making it difficult to resolve the curvature of the molecules. Our conclusion is that the tilt angle depends on the position of the molecule with respect to the substrate. When large, it causes an apparent curved shape and an asymmetry in the distribution of the LUMO, owing to the fact that on one side of the molecule the central ring is closer to the tip. Notice that the relative tilt of phenyl rings was already identified as the cause for the zig-zag appearance of dicyanitrile-sexiphenyl molecules on Ag(111) [101].

2.4 Comparison between the two molecules for deposition @ RT

It is interesting to compare our results with what was observed for NC-Ph₅-CN and NC-Ph₃-CN on Ag(111) with codeposition of Co adatoms to provide coordination centers. A honeycomb network is obtained in this case for both ligands. NC-Ph₃-CN form two domains with the molecules aligned along the first or second nearest neighbors directions, respectively, while the orientation of NC-Ph₅-CN is not discussed [62, 93]. Coordination two is not reported. In the case of Ag(111) the registry between molecules and substrate is not perfectly matching as for Cu(111), and the Co atoms can occupy both the fcc and hcp sites [100], which explains the different molecular orientations observed on this substrate compared to Cu(111).

On Cu(111), the comparison between the assemblies formed by the two molecules reveals a richer landscape. The results presented above show that both NC-Ph₃-CN and NC-Ph₅-CN have an almost perfect epitaxial agreement with the $\langle 11\bar{2} \rangle$ directions of the Cu(111) surface. Both molecules, upon deposition on the substrate kept at room temperature, form coexisting honeycomb and chain structures. However, the orientation of the ligands in such assemblies is different: while NC-Ph₅-CN molecules align along the $\langle 11\bar{2} \rangle$ directions, NC-Ph₃-CN adsorb with the orientations labeled 1 and 2, deviating by $\pm 4^\circ$ and $\pm 11^\circ$ from $\langle 11\bar{2} \rangle$. We explain the origin of these different orientations in terms of competition between the interaction with the substrate, favoring the alignment along second nearest neighbor directions, and the one with the adatoms, favoring a configuration with both atoms right in front of the molecular ends. The longer molecule, with its five phenyl rings and twenty H atoms, has its most stable configuration on the substrate when it optimizes the adsorption geometry, while the shorter molecule favors the straight bond at both ends. For these shorter linkers the alignment along the $\langle 11\bar{2} \rangle$ directions is never observed upon deposition at RT. On the other hand, as we shall see in the following chapter, upon deposition on the substrate kept at a lower temperature the reduced availability of Cu coordination adatoms leads to the formation of patterns with only one adatom per molecule or no adatoms at all. In these structures the adsorption energy and the bond configuration can be optimized at the same time and NC-Ph₃-CN are oriented along $\langle 11\bar{2} \rangle$. As a consequence of the different orientations of the molecules, the assemblies formed by the two ligands after deposition on Cu(111) at room temperature have some features that are apparently common, but that have different origins. For example both molecules form chains with a wavy appearance, however the reason behind the waviness is different for the

2.5. Codeposition of NC-Ph₅-CN and NC-Ph₃-CN

Table 2.1: Summary of the characteristics of the self-assembled structures obtained upon deposition at RT. The NC-Ph₅-CN compact network is measured at 300 K.

Structure	Unit cell size (Cu atoms)	Molecules per un. cell	Cu adatoms		
			per un. cell	coordination	10 ⁻³ ML
NC-Ph ₅ -CN chains	-	-	-	2	< 6
NC-Ph ₅ -CN honeycomb	381	3	2	3	5.2
NC-Ph ₅ -CN compact	64	1	1	2	16
NC-Ph ₃ -CN chains	-	-	-	2	< 12
NC-Ph ₃ -CN honeycomb	189	3	2	3	11

two ligands. In the case of NC-Ph₅-CN it is a consequence of the different alignment of the Cu adatom with the molecular axis at the ends of the ligands, while for NC-Ph₃-CN it originates from the alternance of molecules with different orientations. As for the honeycomb network, in both cases two domains are formed, but for NC-Ph₅-CN they are chiral domains, originating from the chiral nature of the non-aligned nodes, for NC-Ph₃-CN rotational domains, arising from different orientations of the molecules. The characteristics of the different networks are summarized in Table 2.1

We note that while it has been reported that linear molecules differing only by the number of their constituent units can form structures with different stabilities and geometric properties depending on their commensurability with the substrate [59], in our case the long and the short molecules enjoy the same almost perfect epitaxial coincidence with the surface. The differences in the patterns they form on the surface have their origin in the different interactions that prevail in the two cases.

2.5 Codeposition of NC-Ph₅-CN and NC-Ph₃-CN

We also investigated what happens when both types of molecules are evaporated on the surface, one after the other, at $T_{\text{dep}} = 300$ K. We used an amount of molecules of each type corresponding to half of the quantity we normally used for a sample with a single specie, *i.e.* 0.2 ML of NC-Ph₅-CN and 0.14 ML of NC-Ph₃-CN. The resulting structures are shown in Fig. 2.13. The two molecules mix to form a structure with nanosized cavities and three-fold nodes, which is a sort of highly irregular honeycomb network, or equidistant one-dimensional chains. NC-Ph₅-CN molecules are, as in the other networks, aligned along the second nearest neighbor directions. On the other hand, NC-Ph₃-CN in a same region are oriented along all four directions ± 1 and ± 2 , with some molecules along the first nearest neighbor directions. However, rotational domains are formed also for this assembly and one set of directions, forming either positive or negative angles with the second nearest neighbor directions, is favored in each domain.

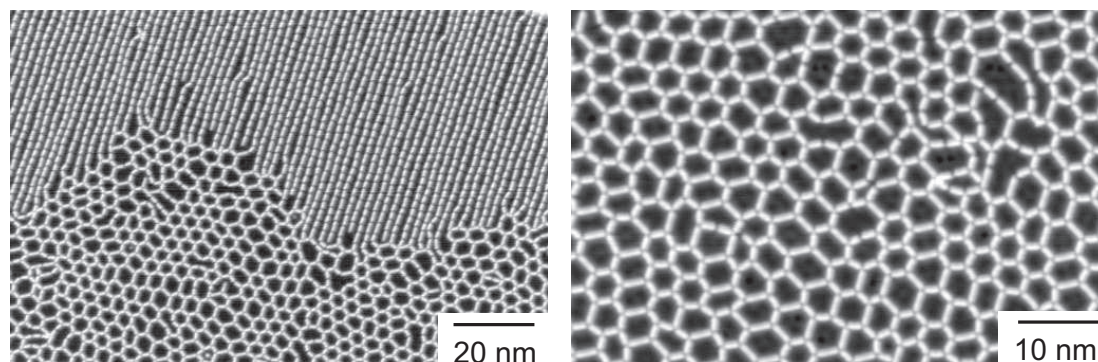


Figure 2.13: NC-Ph₃-CN + NC-Ph₅-CN, $T_{\text{dep}} = 300$ K. Two STM images obtained by codepositing both molecules on the substrate kept at room temperature ($V_t = -50$ mV, $I_t = 50$ pA). Coverage: 0.2 ML of NC-Ph₅-CN and 0.14 ML of NC-Ph₃-CN.

2.6 Conclusions

Deposition of NC-Ph_n-CN molecules on Cu(111) at RT results, thanks to the presence of Cu adatoms supplied by the surface, in the formation of metal-coordinated assemblies. Different structures are obtained: chains and a honeycomb network are formed by NC-Ph₅-CN at 5 K, and a compact structure at 300 K; NC-Ph₃-CN form chains and a honeycomb network that is regular in some areas and shows more variations between neighboring hexagons in others. Interestingly, although both molecules have the same almost perfect epitaxial match with the second nearest neighbor directions of the substrate, only the longer molecules adsorb with this orientation. This happens because the Cu adatoms only adsorb on fcc sites, so if the molecules are in the second nearest neighbor directions the adatoms can not be aligned with the molecular axis at both ends. Thus, a competition arises between a favorable alignment on the substrate along the second nearest neighbor directions, which prevails for NC-Ph₅-CN, and an energetically convenient straight CN-Cu bond at both molecular ends with a favorable bond length, that dominates the assembly of NC-Ph₃-CN molecules. These align along two main directions that are not high symmetry ones. The different orientations of the molecules in these networks have an influence both on the molecule appearance and on the energy position of the unoccupied molecular orbitals.

Chapter summary

On Cu(111) at RT Cu adatoms are present and can provide coordination centers to molecules with appropriate functional groups.

Deposition of **NC-Ph₅-CN** on Cu(111) kept at RT results in the formation of:

- a chain assembly ($T_{\text{meas}} = 5 \text{ K}$)
- a highly regular honeycomb network ($T_{\text{meas}} = 5 \text{ K}$)
- a compact structure ($T_{\text{meas}} = 300 \text{ K}$)

- molecules are always aligned along the second nearest neighbor directions
- the molecule-substrate interaction dominates in the assembly process

Deposition of **NC-Ph₃-CN** on Cu(111) kept at RT results in the formation of:

- a chain assembly ($T_{\text{meas}} = 5 \text{ K}$)
- a regular honeycomb network ($T_{\text{meas}} = 5 \text{ K}$)
- an irregular honeycomb network ($T_{\text{meas}} = 5 \text{ K}$)

- molecules can have two different orientations
- different orientations give rise to different molecule appearances and LUMO energies
- the molecule-adatom interaction dominates in the assembly process

Codeposition of the two molecules results in an irregular porous network

3 NC-Ph_n-CN/Cu(111): Temperature-dependent Assemblies

3.1 Introduction

In self-assembled molecular structures the character of the bond is not completely predetermined by the functional groups, since kinetic effects can also take place to influence the formation of the assembly [64]. Moreover, as we saw in the previous chapter, the availability of Cu coordination adatoms coming from Cu surfaces is temperature dependent. Thus, subject to the substrate temperature during deposition [63, 103] or annealing [72], purely organic or metal-organic networks can be obtained, or a mixture of both. In particular, on Cu(111) the temperature dependence of the type of bonding observed in the assemblies, changing from Cu coordination to hydrogen bond with lowering temperature, was discussed for different systems [63, 72, 104, 73, 79].

In the previous chapter we saw how the metal-organic structures formed upon deposition of NC-Ph_n-CN on the substrate kept at room temperature self-assemble thanks to the availability of a sufficient number of Cu adatoms. Upon lowering of the substrate temperature, the diminished amount of metal centers at disposal of the molecules determines the formation of networks with different geometries, where part of the nodes, or all of them, are purely organic and stabilized by intermolecular hydrogen bonds. At the same deposition temperature different structures can coexist. In this chapter we will explore the assemblies formed when T_{dep} is lowered below 300 K and see how STS reflects some of the differences among the resulting structures.

3.2 NC-Ph₅-CN

When NC-Ph₅-CN molecules are deposited on Cu(111) kept at $T_{\text{dep}} < 300$ K three different assemblies are obtained as a function of the decreasing temperature: a truncated triangular, a kagome and a triangular network.

3.2.1 Truncated triangles network

When $T_{\text{dep}} = 220$ K, NC-Ph₅-CN molecules form a highly ordered network whose cavities have a truncated triangle shape, an overview of which is shown in Fig. 3.1(a). Two domains with different orientations, differing by 17° , are visible on the two substrate terraces. We note that at this deposition temperature, as well as at lower ones, with a coverage of 0.4 ML of molecules,

Chapter 3. NC-Ph_n-CN/Cu(111): Temperature-dependent Assemblies

the same used in Chapter 2, the substrate is no more entirely covered by molecules. Rather, the ligands form compact islands surrounded by regions of bare substrate.

Looking at the close up view in Fig. 3.1(b) the presence of two different kind of nodes is immediately clear. The node enclosed by the green circle is the aligned node already observed in the honeycomb structure, with the Cu atom visible as small bright dot. The node marked by the yellow circle, with the endgroup of one ligand pointing toward the side of the other molecule, is chiral with a counterclockwise rotation, and is formed without coordination atom. We observe with the same probability nodes that are rotated clockwise, forming the other chiral domain. The two nodes alternate at the corners of the cavities. The model we propose for this structure is illustrated in Fig. 3.1(c): as for the honeycomb network, the molecules are adsorbed along $\langle 11\bar{2} \rangle$, and the Cu atoms occupy fcc sites. The unit cell can be represented in

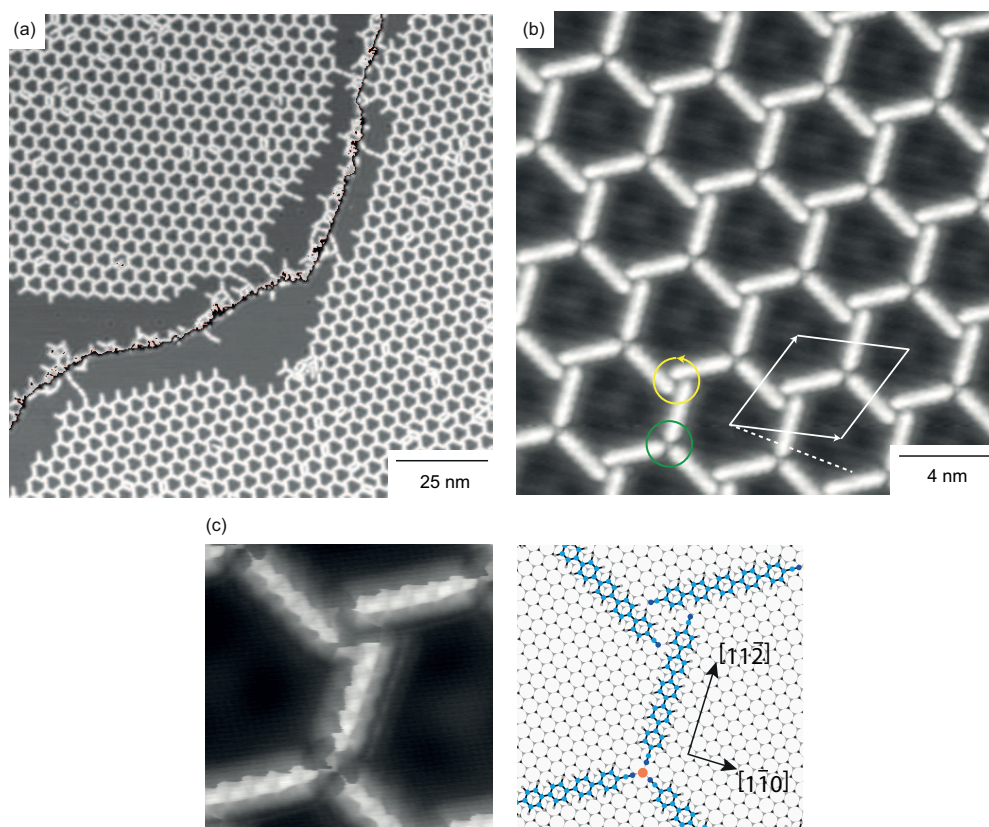


Figure 3.1: NC-Ph₅-CN truncated triangles network, $T_{\text{dep}} = 220$ K. (a) STM image showing the two domains of the truncated-triangle network on two Cu(111) terraces separated by a step ($V_t = -250$ mV, $I_t = 20$ pA). (b) STM image of a truncated triangle domain ($V_t = -20$ mV, $I_t = 20$ pA). Green circle: aligned node; yellow circle: rotated node. Dotted line: $\langle 11\bar{2} \rangle$ direction, the unit cell is indicated. (c) STM image of the two types of nodes ($V_t = -2$ mV, $I_t = 20$ pA) and relative model. Adapted with permission from our paper, Ref. [79].

matrix notation as:

$$\begin{pmatrix} \mathbf{d}_1 \\ \mathbf{d}_2 \end{pmatrix} = \begin{pmatrix} 16 & 3 \\ -3 & 19 \end{pmatrix} \begin{pmatrix} \mathbf{a}_1 \\ \mathbf{a}_2 \end{pmatrix}.$$

The unit cell is sketched in Fig. 3.1(b). The model yields $d = 4.52$ nm; the measured periodicity is 4.53 ± 0.03 nm. This network has a (NC-Ph₅-CN)₃Cu₁ stoichiometry.

For comparison, Pawin *et al.* described a compact structure formed by carbonitrile-modified anthracene molecules on Cu(111) at ≈ 180 K, where the Cu adatom density is too low to ensure the formation of the fully coordinated phase and thus only one adatom every three molecules is available [63]. Recently, the formation of complex structures formed by tripodal molecules containing pyridyl groups and Cu coordination atoms on Ag(111) was observed, where both Cu-pyridyl and pyridyl-HC linkages are present [74, 105]. The truncated triangle network we describe here, however, is the first observation of a regular porous network with alternating metal-coordinated and hydrogen-bonded nodes.

3.2.2 Kagome network

Further lowering of T_{dep} to 160 K results in the formation of purely molecular assemblies. In Fig. 3.2(a) we can see two islands formed by smaller patches of different patterns, linked by transition regions. Among them, it is possible to recognize a kagome motif and some hexagonal patterns. The fact that these structures coexist points towards similar formation energies [96]. Some additional molecules are present in the larger cavities and lead to denser regions. From the rotation of the nodes we can see that in each of the two domains all the assemblies possess the same handedness, while the two domains have opposite chirality.

Figure 3.2(b) shows a close up view of the kagome network. In this structure nodes are constituted by the junction of four molecules (blue circle). Nodes formed by three molecules as in the truncated-triangular network, yellow circle, are also present and constitute defects in the kagome pattern. Figure 3.2(c) shows the detail of the kagome nodal structure, obtained using a CO functionalized tip. In each node the four molecules are arranged in such a way as to form several H-NC bonds. The arrangement of the molecules on the surface is sketched in the model that accompanies the STM image. Also in this network the molecules are adsorbed along the $\langle 11\bar{2} \rangle$ directions. The kagome structure is represented in matrix notation as:

$$\begin{pmatrix} \mathbf{e}_1 \\ \mathbf{e}_2 \end{pmatrix} = \begin{pmatrix} 22 & -5 \\ 5 & 17 \end{pmatrix} \begin{pmatrix} \mathbf{a}_1 \\ \mathbf{a}_2 \end{pmatrix}$$

with $e = 5.10$ nm. The measured periodicity is 5.11 ± 0.03 nm.

A kagome pattern was already reported for NC-Ph₅-CN on Ag(111) [65]: it is the only assembly these molecules form if Co adatoms are not co-evaporated on the surface. In this network the molecules form two slightly different types of nodes, originating from a non-planar adsorption of the molecules together with the stacking on the Ag(111) surface. NC-Ph₆-CN, on the other hand, form a kagome network on Ag(111) that has only one kind of node, which was attributed to a more planar adsorption configuration [96]. On Cu(111), we don't observe any difference

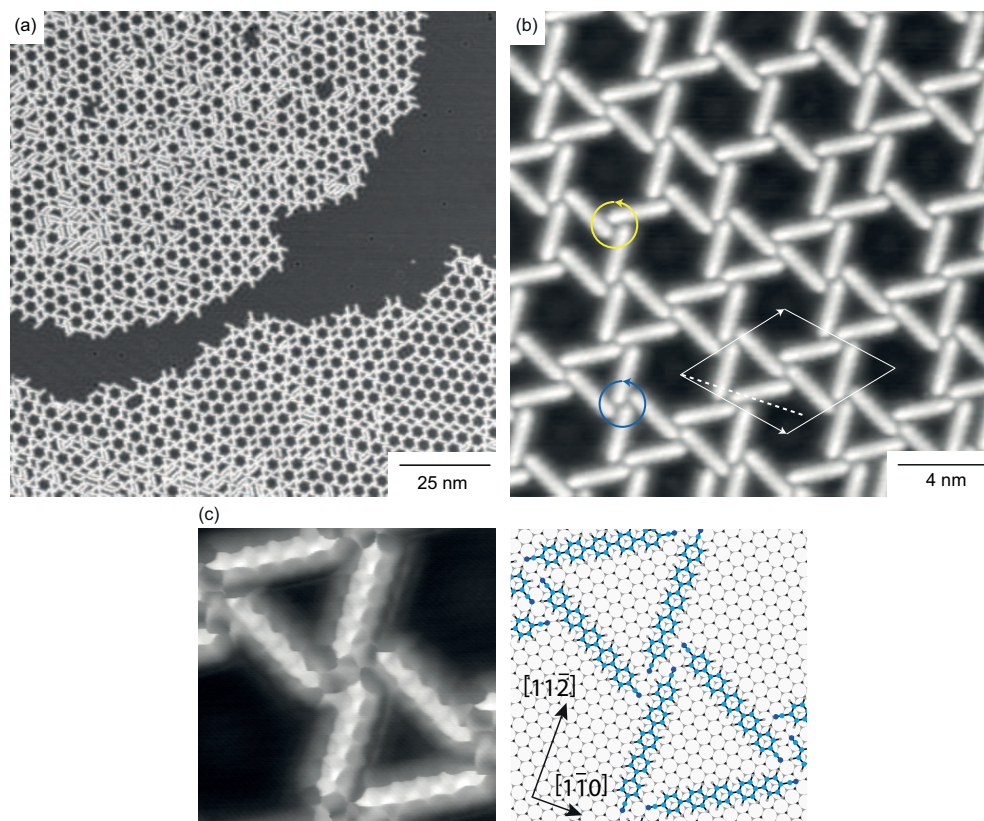


Figure 3.2: NC-Ph₅-CN kagome network, $T_{\text{dep}} = 160$ K. (a) STM image showing two domains of purely organic assemblies ($V_t = -100$ mV, $I_t = 20$ pA). (b) STM image of a kagome domain ($V_t = -20$ mV, $I_t = 20$ pA). Blue circle: fourfold node; yellow circle: rotated threefold node. Dotted line: $\langle 1\bar{1}0 \rangle$ direction; the unit cell is indicated. (c) Closeup view of the fourfold node and corresponding model ($V_t = -2$ mV, $I_t = 20$ pA). Adapted with permission from our paper, Ref. [79].

in the nodes in the kagome structure formed by NC-Ph₅-CN.

3.2.3 Triangular structure

A second phase coexists with the kagome network when the molecules are deposited on the sample kept at $T_{\text{dep}} = 160$ K: a triangular structure, formed by triangles and rhombi, that is illustrated in Fig. 3.3. The central part of the island seen in the large scale image in Fig. 3.3(a) appears denser because of additional molecules hosted in the cavities; as indicated by the arrow, adjacent triangles are aligned along $\langle 1\bar{1}0 \rangle$. Figure 3.3(b) presents a closeup view of the network. The triangles are composed of three-fold purely organic nodes, as the ones of the truncated-triangle phase. Here, however, in each triangle nodes of opposite handedness alternate, producing an achiral structure. The rhombi appear as defects which induce a change in the orientation of the triangles (upper part of the image: triangles pointing up, lower part: triangles pointing down). Another type of imperfection is enclosed by the white circle: two opposite nodes are not well aligned and induce the formation of triangles with the opposite

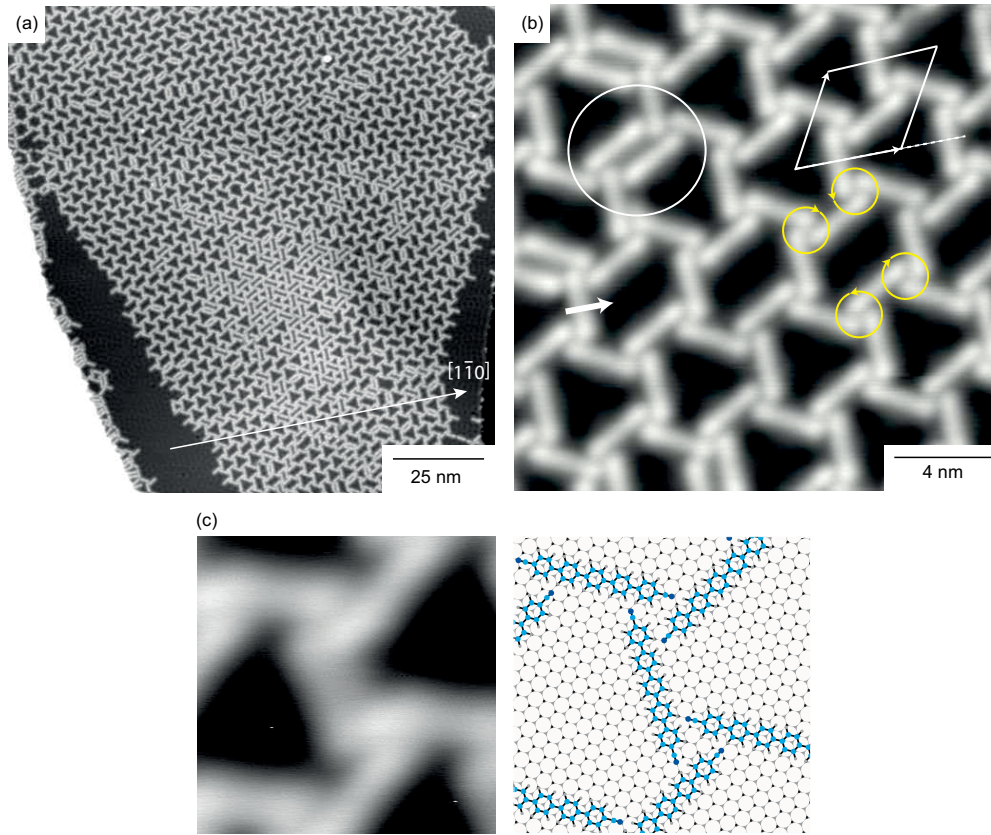


Figure 3.3: NC-Ph₅-CN triangular structure, $T_{\text{dep}} = 160$ K. (a) STM image of a domain of the triangular network. (b) Closeup view: a row of rhombi, inducing a boundary between two differently oriented regions, is indicated by the arrow. Yellow circles: threefold nodes; the white circle encloses a typical defect. Dotted line: $\langle 1\bar{1}0 \rangle$, the unit cell is indicated. (c) Closeup view of the nodes and corresponding model. Tunneling parameters for all images: ($V_t = -20$ mV, $I_t = 20$ pA). Adapted with permission from our paper, Ref. [79].

orientation. The regular triangular structure (discarding the presence of the rhombi) can be represented in matrix notation as:

$$\begin{pmatrix} f_1 \\ f_2 \end{pmatrix} = \begin{pmatrix} 15 & 0 \\ 0 & 15 \end{pmatrix} \begin{pmatrix} a_1 \\ a_2 \end{pmatrix}.$$

with $f = 3.83$ nm. The measured periodicity is 3.84 ± 0.03 nm; molecules are aligned along the $\langle 11\bar{2} \rangle$ directions.

The exclusive formation of purely organic assemblies at $T_{\text{dep}} = 160$ K reflects the fact that at this temperature the adatom density is extremely low. Although we still observe the formation of some metal-organic nodes, or the decoration of steps by short chains, the overall adatom density is negligible.

3.2.4 Spectroscopy on the NC-Ph₅-CN temperature-dependent assemblies

On each of the structures described above we performed STS measurements to reveal the influence of the molecular organization on the position and features of the unoccupied molecular orbitals.

dI/dV spectra acquired on molecules in the truncated triangle network are displayed in Fig. 3.4(a). We observe the LUMO at 1.10 eV with maximum intensity on the center of the molecules. The LUMO+1, which is especially intense on the molecular ends and on the nodes of the structure, reflects the difference between the metal-coordinated and the purely organic nodes, with the latter showing a higher intensity. The energy position of this orbital is 1.70 eV. In Fig. 3.4(b) an STM image accompanied by the relative STS maps recorded at 1.10, 1.70 and 2.50 V, respectively, shows the spatial distribution of these orbitals. The LUMO+1 map at 1.70 V reflects the difference in the intensity of the spectra on the node with and without the Cu adatom seen in the spectra. The map at 2.50 eV probably does not capture perfectly the LUMO+2, but damage to the network produced at higher voltages limits the energy range we can explore. Nevertheless, we can recognize the characteristic distribution of this orbital, as seen in Section 2.2.4, with maximum intensity on the center of the molecules and on the nodes.

The general features of the orbitals observed on the truncated triangle structure are common

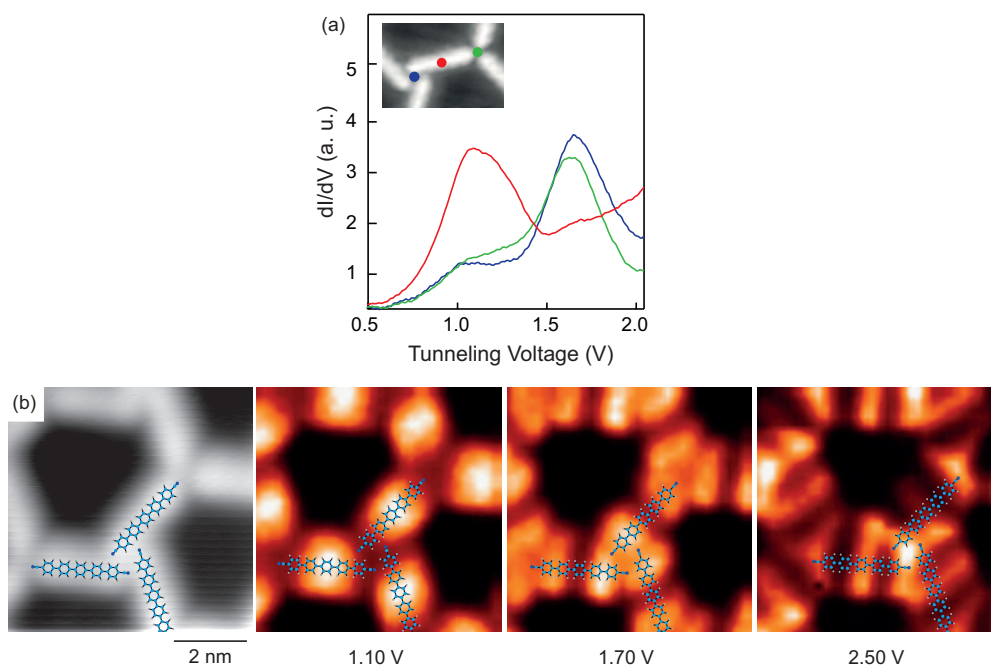


Figure 3.4: NC-Ph₅-CN: spectroscopy on the truncated triangle network. (a) dI/dV spectra acquired on the locations shown on the inset (red: center, blue: rotated node, green: aligned node). (b) Topography and corresponding STS maps recorded at 1.10, 1.70 and 2.50 eV showing the LUMO, the LUMO+1 and the LUMO+2, respectively. Three molecular backbones are superimposed for comparison. (Setpoint: $V_t = +500$ mV, $I_t = 20$ pA, $V_{\text{mod}} = 20$ mV at 523 Hz).

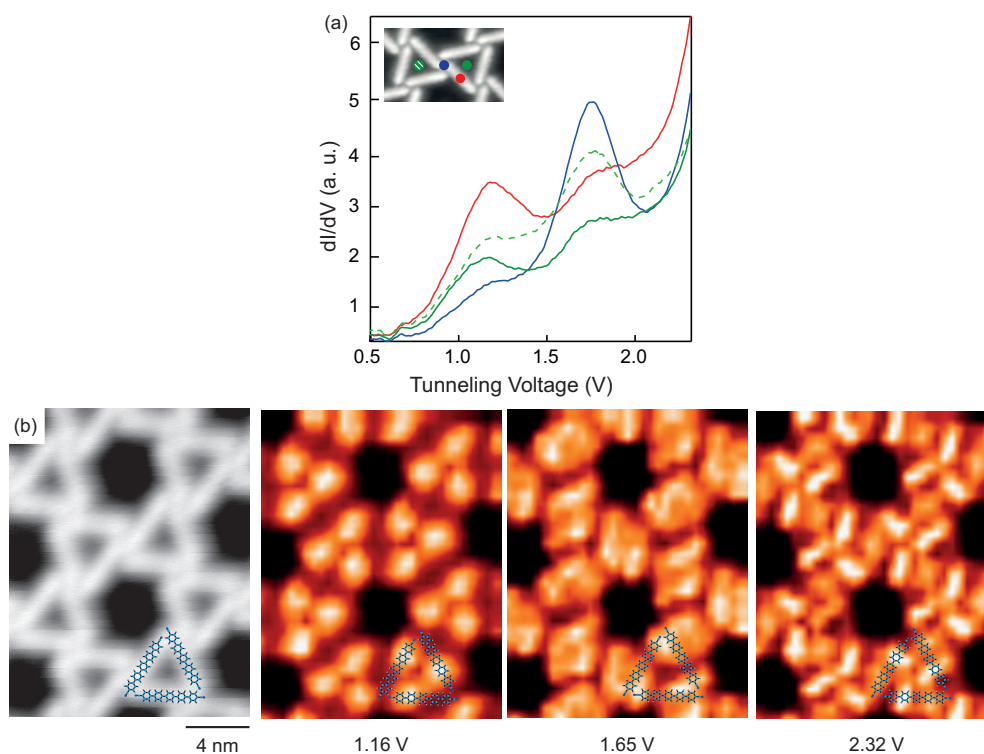


Figure 3.5: NC-Ph₅-CN: spectroscopy on the kagome network. (a) dI/dV spectra acquired on the locations shown on the inset (red: center, blue: node, green solid and green dashed: centers of two inequivalent triangles). (b) Topography and corresponding STS maps recorded at 1.16, 1.65 and 2.32 eV showing the LUMO, the LUMO+1 and the LUMO+2, respectively. Three molecular backbones are superimposed for comparison. (Setpoint: $V_t = +500$ mV, $I_t = 20$ pA, $V_{\text{mod}} = 20$ mV at 523 Hz).

to molecules assembled in the kagome network. Figures 3.5(a) and (b) show that also in this case the LUMO is located at an energy of 1.10 eV and is localized on the center of the molecules, the LUMO+1 has an energy of 1.70 eV and maximum intensity on the molecular ends and on the nodes, and the LUMO+2 is located at an energy which is higher than the one we can reach without damaging the network, even though a map recorded at 2.32 V can already capture the high intensity on the center of the ligands. The interesting feature that can be observed on this network is that the spectra measured on the triangular cavities are inequivalent (solid and dashed green lines in Fig. 3.5(a)). This is a consequence of the fact that, as can be seen by carefully looking at the model for this network presented in Fig. 3.2(c), the two types of triangles have a slightly different registry with the substrate.

Finally, spectra and maps acquired on the triangular structure are shown in Figs. 3.6(a) and (b). While the general features of the molecular orbitals are the same seen above for the other networks, we note that both the spectra and the LUMO+1 map show a difference between the nodes of opposite chirality of this structure even though, unlike in the truncated triangle network, in this case both nodes are purely organic. To understand the origin of this difference we have to take into consideration the model shown in Fig. 3.3(c): while both nodes are

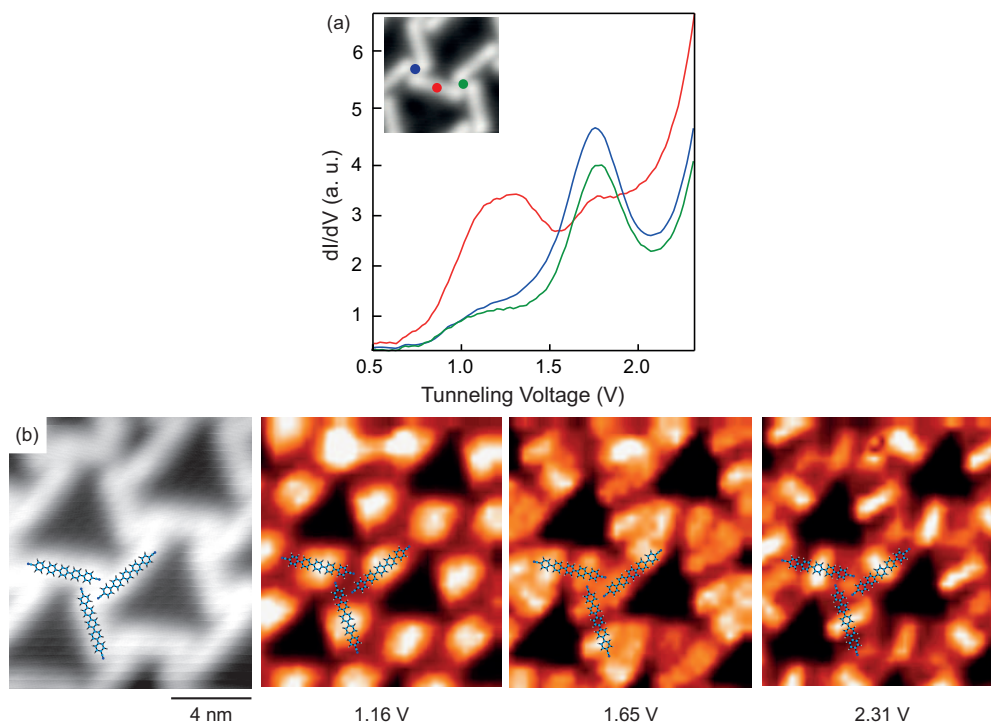


Figure 3.6: NC-Ph₅-CN: spectroscopy on the triangular network. (a) dI/dV spectra acquired on the locations shown on the inset (red: center, blue: node rotated clockwise, green: node rotated counterclockwise). (b) Topography and corresponding STS maps recorded at 1.16, 1.65 and 2.31 eV showing the LUMO, the LUMO+1 and the LUMO+2, respectively. Three molecular backbones are superimposed for comparison. (Setpoint: $V_t = +500$ mV, $I_t = 20$ pA, $V_{\text{mod}} = 20$ mV at 523 Hz).

centered around an hcp site of the substrate, in one case the H atoms are found on fcc sites, in the other on top.

These results show how scanning tunneling spectroscopy can be used to reveal and amplify differences, sometimes even very small ones, among different regions of the system, going from the presence of a metal-coordination atom to a different registry of the molecular structure with respect to the surface. The general characteristics of the orbitals, on the other hand, are independent from the way the molecules are assembled.

3.3 NC-Ph₃-CN

As in the case for the longer ligands, also NC-Ph₃-CN molecules, when evaporated on the substrate kept at temperatures lower than 300 K, form different assemblies depending on T_{dep} : a truncated triangular, a kagome, a chevron and an open kagome structure are observed.

3.3.1 Truncated triangles network

Deposition of the molecules on the substrate kept at $T_{\text{dep}} = 220$ K results in the formation of a truncated-triangles network, in which metal coordinated and purely organic nodes alternate

at the corners of each cavity (orange and green circles, respectively, in Fig. 3.7(b)). This network is perfectly equivalent to the one observed for NC-Ph₅-CN molecules presented in section 3.2.1. Fig. 3.7(a) shows a large-scale image of the network which is highly regular, even though a number of guest molecules are found in the cavities. As for NC-Ph₅-CN, the purely organic nodes are chiral, as they can be rotated clockwise or counter-clockwise, thus two chiral domains are formed. In the close up view of Fig. 3.7(b) the two domains are presented. The unit cell, indicated in white on the image, is represented in matrix notation as:

$$\begin{pmatrix} \mathbf{g}_1 \\ \mathbf{g}_2 \end{pmatrix} = \begin{pmatrix} 13 & -3 \\ 3 & 10 \end{pmatrix} \begin{pmatrix} \mathbf{a}_1 \\ \mathbf{a}_2 \end{pmatrix}$$

with $g = 3.01$ nm.

In Fig. 3.7(c) an image obtained with a CO functionalized tip shows intramolecular resolution. The superimposed model shows the alignment of the molecules along $\langle 11\bar{2} \rangle$.

Indeed, for deposition temperatures in the range investigated in this part of the work, $220 \text{ K} > T_{\text{dep}} > 140 \text{ K}$, the amount of adatoms is strongly reduced compared to RT, thus there is either one adatom every two nodes, as in the case of the truncated triangle network, or no adatoms

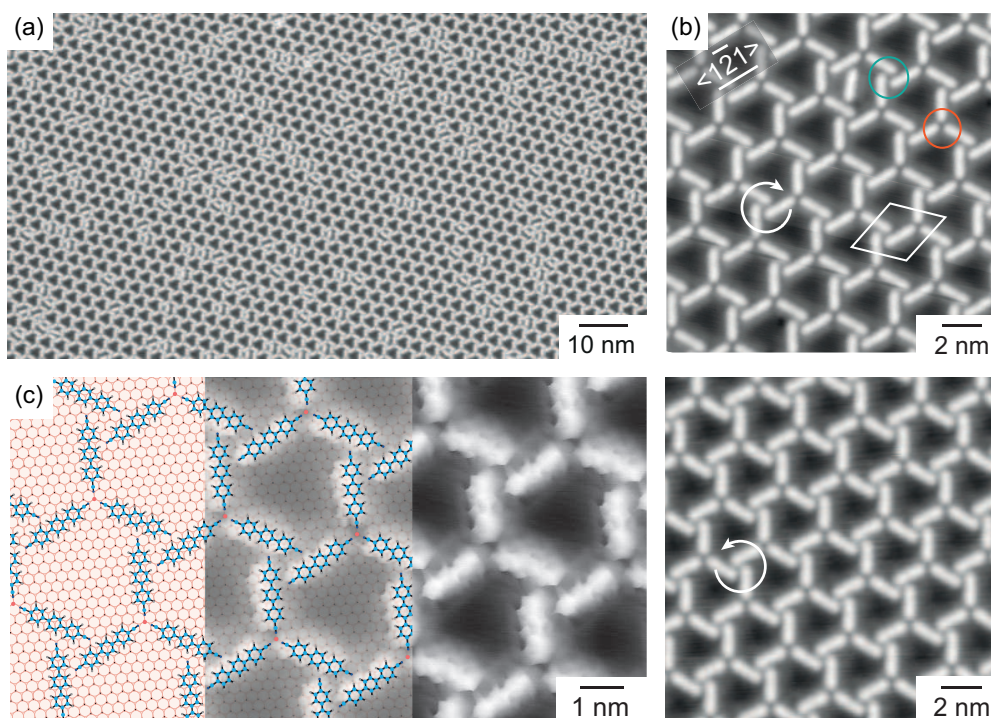


Figure 3.7: NC-Ph₃-CN truncated triangle network, $T_{\text{dep}} = 220$ K. (a) Large area image of the assembly ($V_t = -500$ mV, $I_t = 100$ pA). (b) The two chiral domains, with the unit cell indicated. The orange and the green circle show the metal coordinated and the purely organic node, respectively. Tunneling parameters as in (a). (c) Image measured with a CO functionalized tip showing intramolecular resolution accompanied by the network model ($V_t = -5$ mV, $I_t = 200$ pA).

at all, as we will show below. In this situation the competition between the molecule-substrate and the molecule-adsorbate interaction vanishes, as the molecules can at the same time be oriented along the $\langle 11\bar{2} \rangle$ directions and have the only Cu adatom in line with the molecular axis.

3.3.2 Kagome network

Lowering T_{dep} to ≈ 190 K leads to the formation of two coexisting structures, a kagome network and a chevron pattern, both purely organic assemblies.

An overview of the kagome structure is shown in Fig. 3.8(a). This network, as the one formed by NC-Ph₅-CN molecules to which is perfectly equivalent, is characterized by hexagonal cavities around which six small triangular cavities are arranged. The nodes are four-fold and have a chiral nature, implying the existence of two chiral domains as shown in Fig. 3.8(b). The unit cell, indicated on the image, is expressed as:

$$\begin{pmatrix} \mathbf{h}_1 \\ \mathbf{h}_2 \end{pmatrix} = \begin{pmatrix} 14 & -1 \\ 1 & 13 \end{pmatrix} \begin{pmatrix} \mathbf{a}_1 \\ \mathbf{a}_2 \end{pmatrix}$$

with $h = 3.45$ nm. The molecules are aligned along $\langle 11\bar{2} \rangle$, as shown on the model in Fig. 3.8(c). The difference with the kagome network formed by NC-Ph₅-CN is that in that the case of the

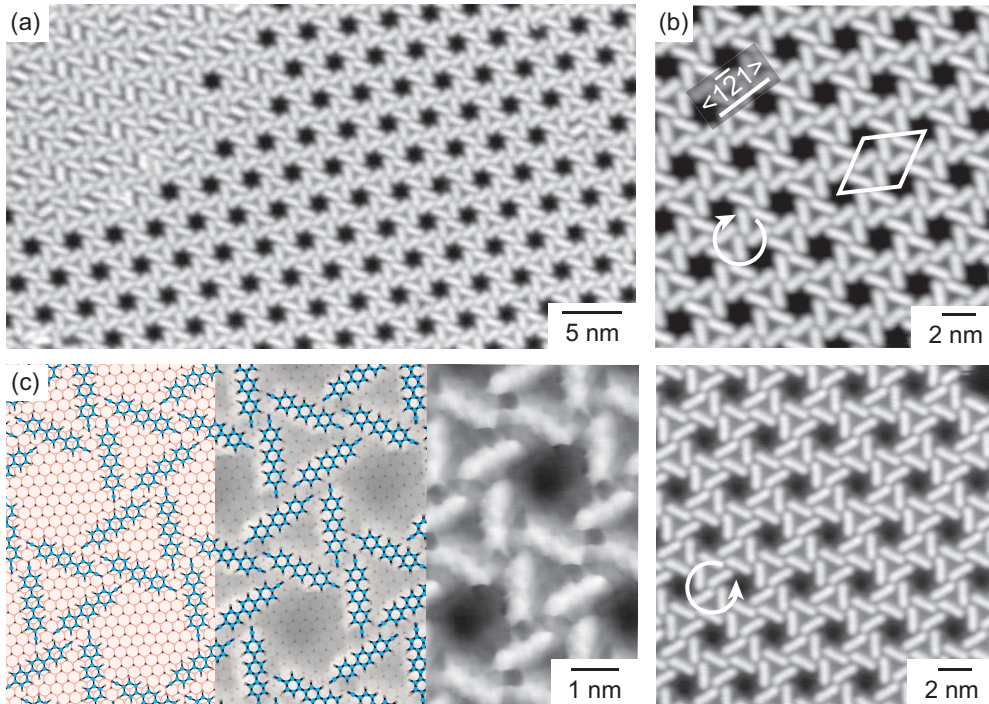


Figure 3.8: NC-Ph₃-CN kagome network, $T_{\text{dep}} = 190$ K. (a) Image of the network with an area of denser pattern ($V_t = -200$ mV, $I_t = 200$ pA). (b) Detail of the two chiral domains. The unit cell is indicated, tunneling parameters as in (a). (c) High resolution image acquired with a CO functionalized tip and model of the network ($V_t = -5$ mV, $I_t = 200$ pA).

longer molecules only small patches of ordered kagome are observed, while here the network extends over large areas with a low concentration of defects, even though in some regions, like in the left corner of Fig. 3.8 (a), a higher density pattern is formed owing to the insertion of guest molecules in the hexagonal cavities.

3.3.3 Chevron pattern

The second structure that is obtained at $T_{\text{dep}} \approx 190$ K is a chevron pattern, a very dense assembly that is shown in Fig. 3.9. Also in this network all nodes are purely organic, stabilized by hydrogen bonds. As can be seen in Fig. 3.9(a) the pattern extends over large areas, covering entire terraces without forming defects (the dark spots observed in the image are due to the presence of adsorbates, probably CO molecules, on the surface). Owing to the underlying symmetry of the substrate, the network can have three equivalent orientations with respect to it, and thus three mirror domains rotated by 120° with respect to one another are formed (Fig. 3.9(b)). The molecules, as can be seen from the model in Fig. 3.9(c), are aligned half along $\langle 11\bar{2} \rangle$ and half along $\langle 1\bar{1}0 \rangle$. The unit cell, indicated in Fig. 3.9(b), can be expressed as:

$$\begin{pmatrix} \mathbf{i}_1 \\ \mathbf{i}_2 \end{pmatrix} = \begin{pmatrix} 2 & 5 \\ -6 & 4 \end{pmatrix} \begin{pmatrix} \mathbf{a}_1 \\ \mathbf{a}_2 \end{pmatrix}$$

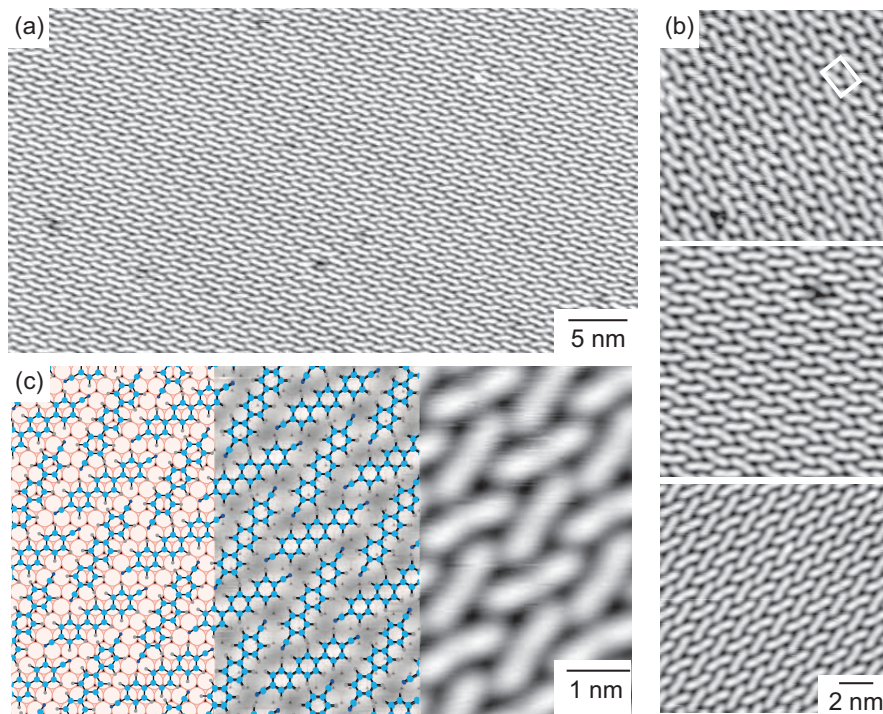


Figure 3.9: NC-Ph₃-CN chevron pattern, $T_{\text{dep}} = 190$ K. (a) Overview of the assembly (b) The three mirror domains, the unit cell is indicated. (c) Close-up view and model showing the molecules aligned half along $\langle 11\bar{2} \rangle$ and half along $\langle 1\bar{1}0 \rangle$. Tunneling parameters for all images: $V_t = -200$ mV and $I_t = 100$ pA.

with $i_1 = 1.59$ nm and $i_2 = 1.35$ nm.

This network is not observed for NC-Ph₅-CN molecules on Cu(111). On the other hand, when NC-Ph₃-CN molecules are deposited on Ag(111) without codeposition of Co atoms a chevron pattern is the only assembly they form, with the molecules aligned half along the $\langle 1\bar{1}0 \rangle$ direction and half along the $\langle 7\bar{3}4 \rangle$ one [65]. Thus this pattern seems to be specific to NC-Ph₃-CN.

3.3.4 Open kagome network

When the substrate temperature is further lowered to $T_{\text{dep}} \approx 140$ K an hitherto unobserved organic pattern, that we called open kagome, is formed, Fig 3.10. While having a structure reminiscent of that of the kagome pattern, as it is composed by hexagonal cavities surrounded by six triangles each, this network has a nodal geometry that is quite different from the one observed in the kagome. Moreover, the hexagonal cavities are much bigger, while the triangular ones are very small. This network, as seen in Fig. 3.10(a), does not form extended domains, but rather small patches separated by regions of bare substrate. As the nodes have, also for this network, a chiral nature, two chiral domains are formed and in Fig. 3.10(a) they are both present. A more detailed view of the two domains is presented in Fig. 3.10(b), where the unit

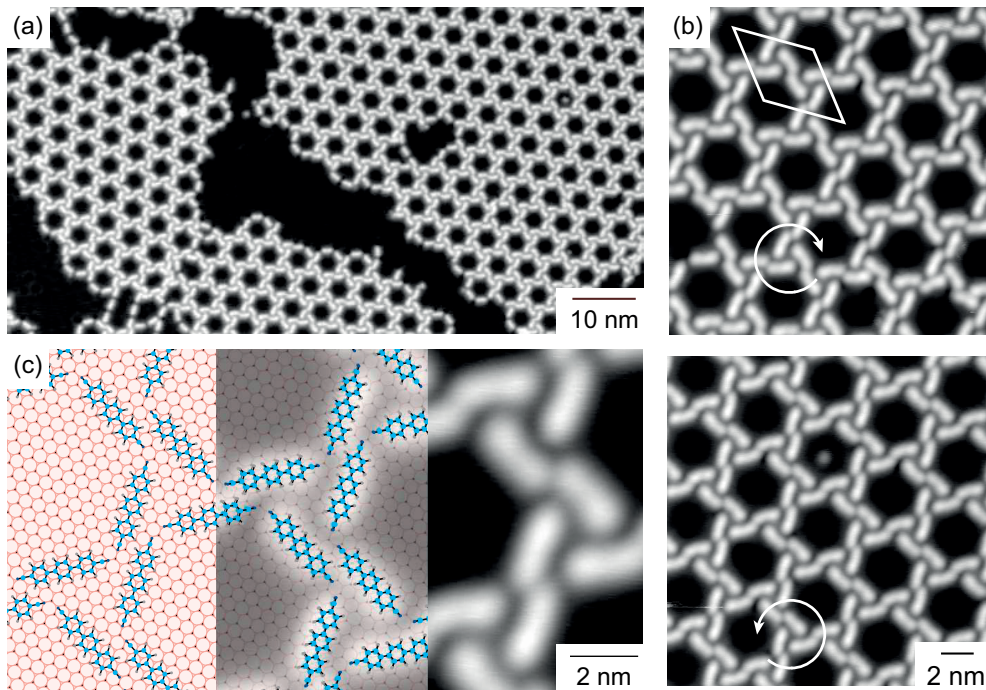


Figure 3.10: NC-Ph₃-CN open kagome network, $T_{\text{dep}} = 140$ K. (a) Large scale image showing islands with different chiral domains. (b) Close up view of the two domains with a sketch of the unit cell. (c) Proposed model of the network. Tunneling parameters for all images are $V_t = 200$ mV and $I_t = 50$ pA.

cell is indicated. The matrix expression of the unit cell is:

$$\begin{pmatrix} \mathbf{j}_1 \\ \mathbf{j}_2 \end{pmatrix} = \begin{pmatrix} 19 & -6 \\ 6 & 13 \end{pmatrix} \begin{pmatrix} \mathbf{a}_1 \\ \mathbf{a}_2 \end{pmatrix}$$

with $j = 4.28$ nm. The molecules, as seen on the model in Fig. 3.10(c), are aligned along the $\langle 11\bar{2} \rangle$ directions.

3.3.5 Annealing @ RT

When a sample on which molecules have been deposited at $T_{\text{dep}} \approx 190$ K, thus covered with purely organic assemblies, is annealed at RT for 10 minutes, honeycomb and chain structures are obtained, with an adatom at each node, Fig. 3.11. The sample appears perfectly equivalent to the ones obtained by deposition of the molecules at RT. This confirms the importance of thermal activation of the process of adatom production and the high mobility of the molecules at RT.

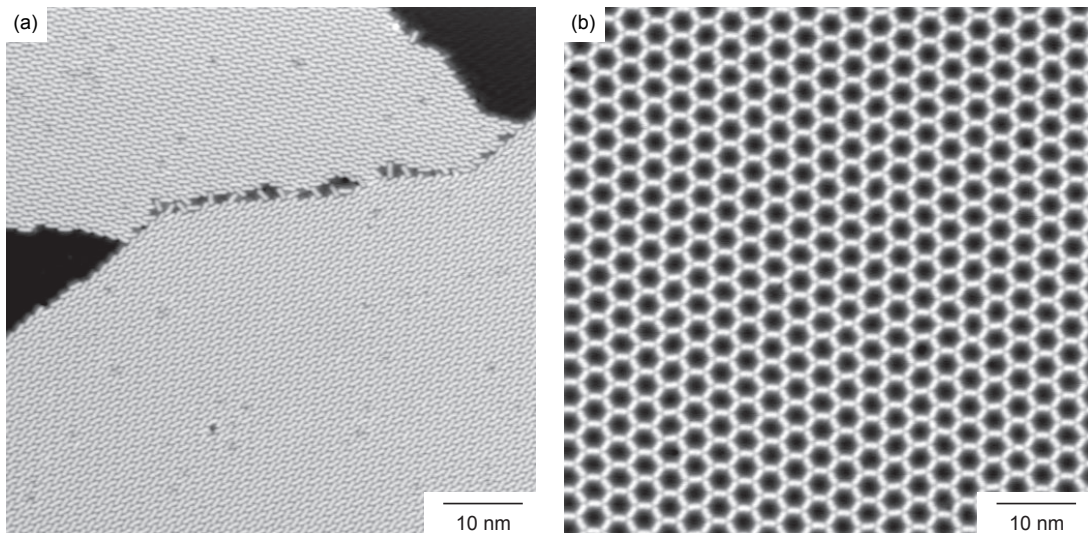


Figure 3.11: NC-Ph₃-CN: annealing at RT. (a) STM image of the sample before the annealing: a huge patch of chevron pattern is visible ($T_{\text{dep}} = 190$ K). (b) STM image of the sample after 10 minutes annealing at 300 K. The result is the same as depositing the molecules at RT. For both images $V_t = -500$ mV and $I_t = 50$ pA.

3.3.6 Spectroscopy on the NC-Ph₃-CN temperature-dependent assemblies

Spectroscopic measurements for the truncated triangle network are presented in Fig. 3.12. As seen in the spectra of Fig. 3.12(a) and in the differential conductance map of the panel (c) of the same figure, we observe the LUMO at an energy of 1.4 eV, mainly located on the center of the molecule (red curve). The LUMO+1, on the other hand, is found at an energy of 2.4 eV and has its maximum intensity on the molecular ends and on the nodes. The different nodal geometry at the two ends of the molecule is reflected in a difference in the intensity of the LUMO+1 orbital (green and blue curves), which has its maximum intensity on the uncoordinated node (green). Unfortunately, the bias voltage corresponding to this orbital is too high to record differential conductance maps without damaging the network, thus we are not able to image its spatial distribution. Since this network hosts a certain number of guest molecules, it is also interesting to see what is the effect on the electronic structure of the different environment experienced by these molecules. In Fig 3.12(c) the dI/dV signal acquired on the center of a guest molecule, depicted in blue, is compared to the one of a ligand that is part of the network, in red: the LUMO is not only shifted upwards of about 0.2 eV, it also has a higher intensity.

For the kagome network, as in the case of the longer ligands, we observe a difference between

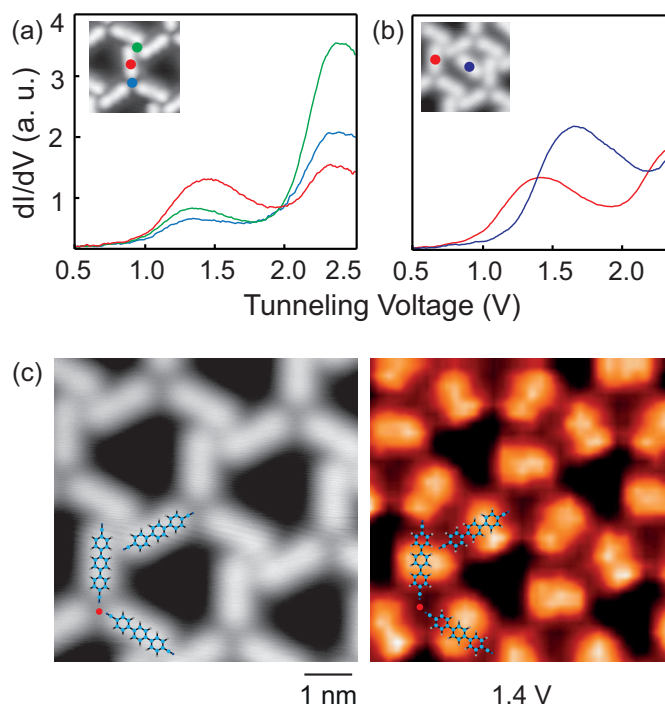


Figure 3.12: NC-Ph₃-CN: spectroscopy on the truncated triangle network. (a) dI/dV spectra acquired on the locations shown on the inset (red: center, blue: rotated node, green: aligned node). (b) Spectra acquired on the center of a guest molecule (blue) and of a molecule in the network (red). (c) Topography and corresponding STS map recorded at 1.4 eV showing the LUMO. Three molecular backbones are sketched for comparison. (Setpoint: $V_t = +500$ mV, $I_t = 10$ pA, $V_{mod} = 20$ mV at 523 Hz).

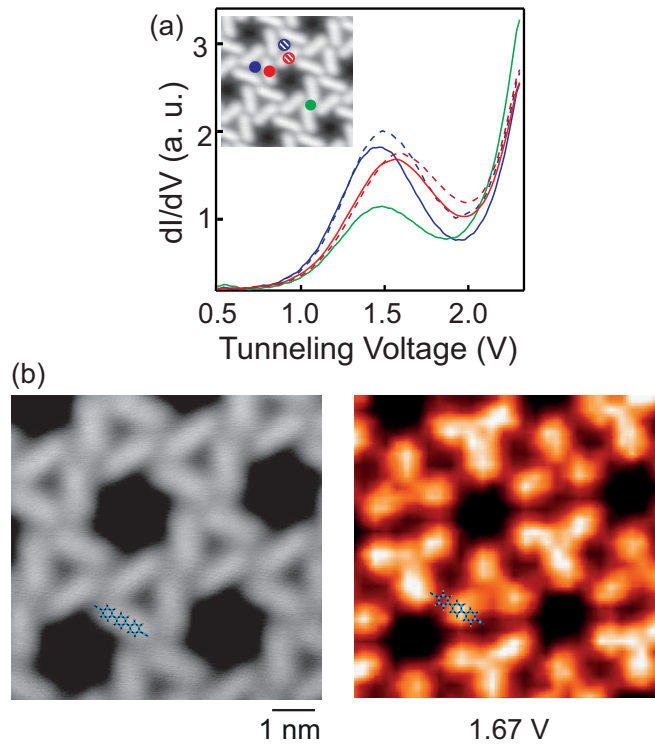


Figure 3.13: NC-Ph₃-CN: spectroscopy on the kagome network. (a) dI/dV spectra acquired on the locations shown on the inset (red solid and red dashed: centers of molecules around inequivalent triangles, green: node, blue solid and blue dashed: centers of two inequivalent triangles). (b) Topography and corresponding STS map recorded at 1.67 eV showing the LUMO. One molecular backbone is sketched for comparison. (Setpoint: $V_t = +500$ mV, $I_t = 25$ pA, $V_{\text{mod}} = 20$ mV at 523 Hz).

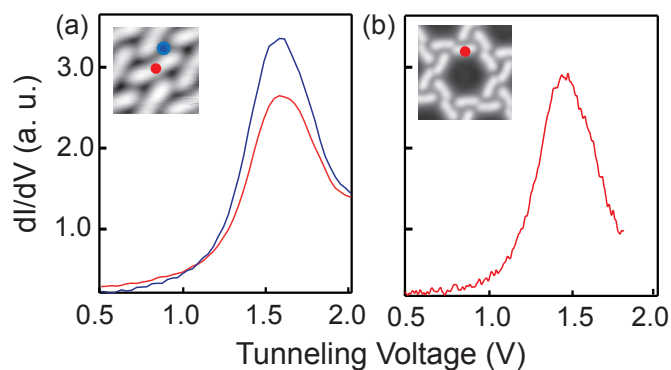


Figure 3.14: NC-Ph₃-CN: spectroscopy on the chevron and open kagome structures. (a) dI/dV spectra acquired on the locations shown on the inset on the chevron pattern (red: center, blue: space between molecules) (setpoint: $V_t = +500$ mV, $I_t = 20$ pA, $V_{\text{mod}} = 20$ mV at 523 Hz). (b) dI/dV spectrum acquired on the location shown on the inset on the open kagome network (red: center) (setpoint: $V_t = +500$ mV, $I_t = 2$ pA, $V_{\text{mod}} = 10$ mV at 523 Hz).

the spectra recorded on the two inequivalent type of triangles, for which we use, in Fig. 3.13(a), solid and dashed lines respectively. Both for the center of one of the molecules enclosing the cavity, red spectra, and for the center of the triangular cavity itself, blue spectra, there is a small difference in energy and intensity of the LUMO, which is found at around 1.5 eV for the center of the triangles and 1.6 eV for the molecules around them. The difference in the spectra recorded over the two types of triangles is due to a slight difference in the way the two cavities are disposed with respect to the substrate, and it is reflected in a difference of contrast between neighboring triangles, as observed in the dI/dV map shown in Fig. 3.13(b). In this network the localization of the LUMO on the center of the molecules is even more marked than in the truncated triangles assembly, and the LUMO of each molecule has an almost circular shape. STS measurements on the chevron pattern, Fig. 3.14(a), show that the LUMO has an energy of 1.6 eV and is again located on the center of the molecule. In this very compact assembly, intensity is observed also in the space between molecules (blue curve). Spectra recorded on the open kagome network are presented in Fig. 3.14(b). This network is easier to damage while recording spectra, thus the signal is more noisy and the maximum voltage used is 1.8 V. However, also in this case a LUMO located on the center of the molecule and with an energy of 1.5 eV is observed.

3.4 Conclusions

In summary, lowering the substrate temperature during deposition results in a diminished amount of Cu adatoms available for the formation of metal-coordinated structures. At 220 K the number of adatoms is still sufficient for the formation of a porous network with half the nodes Cu-coordinated and half purely organic. At lower temperatures, we observe purely organic assemblies with a variety of geometries. All the structures but one are chiral. In all these assemblies molecules are aligned along the second nearest neighbor directions. The characteristics of the observed assemblies are summarized in Table 3.1

STS is used to reveal that the general features of the molecular orbitals do not depend much on the kind of structure molecules form. However, we discern different fingerprints for the metal-coordinated and the purely organic nodes, and we observe differences in the spectra that reflect slight disparities in the structures registry with the substrate.

Table 3.1: Summary of the characteristics of the self-assembled structures obtained upon deposition at low temperature.

Structure	Unit cell size (Cu atoms)	Molecules per un. cell	Cu adatoms		T_{dep} (K)
			per un. cell	coordination	
NC-Ph ₅ -CN trunc. triangles	313	3	1	3	220
NC-Ph ₅ -CN kagome	399	6	0	-	160
NC-Ph ₅ -CN triangles	255	3	0	-	160
NC-Ph ₃ -CN trunc. triangles	139	3	1	3	220
NC-Ph ₃ -CN kagome	183	6	0	-	190
NC-Ph ₃ -CN chevron	38	2	0	-	190
NC-Ph ₃ -CN open kagome	283	6	0	-	140

Chapter summary

The lower T_{dep} , the less Cu adatoms are available for nodal coordination.

Deposition of **NC-Ph₅-CN** on Cu(111) results in the formation of:

- @ $T_{\text{dep}} = 220$ K a truncated triangles network (1 Cu adatom every two nodes)
- @ $T_{\text{dep}} = 160$ K a kagome network (no Cu adatoms)
- @ $T_{\text{dep}} = 160$ K a triangular structure (no Cu adatoms)

Deposition of **NC-Ph₃-CN** on Cu(111) results in the formation of:

- @ $T_{\text{dep}} = 220$ K a truncated triangles network (1 Cu adatom every two nodes)
- @ $T_{\text{dep}} = 190$ K a kagome network (no Cu adatoms)
- @ $T_{\text{dep}} = 190$ K a chevron pattern (no Cu adatoms)
- @ $T_{\text{dep}} = 140$ K an open kagome network (no Cu adatoms)

Molecules are always oriented along the second nearest neighbor directions

STS shows a difference between metal-coordinated and organic nodes and between structures with a different registry with the substrate

Annealing at RT of assemblies formed at low temperature results in the recovery of chain and honeycomb structures, as upon deposition at RT.

4 Er(trensal) single molecule magnets

4.1 Introduction

In Chapters 2 and 3 we have seen how changing the molecular coverage and the substrate temperature during molecule deposition can result in a rich variety of different assemblies. In this chapter we will investigate the effect of using different substrates or, to be more precise, to use decoupling layers [106, 107, 108, 109] to change the balance between molecule-substrate and molecule-molecule interaction, allowing the transition from a disordered system to an organized one. We will investigate the self-organization of a special type of molecule, a single ion magnet. As the reason why this class of molecules is so interesting lies in their magnetic properties, being able to control their organization is very important, as it means being able to exploit their potential at best.

Single molecule magnets (SMM) [110, 111, 112] are metal-organic complexes that exhibit very long magnetization relaxation times at low temperature. They have a huge potential for possible applications such as information storage and spintronics [113, 17]. Single ion magnets (SIM) are a subclass of SMM. They are structurally rather robust and therefore can be evaporated on surfaces without damage. For the magnetic core, lanthanide ions are especially promising, because of their large magnetic moments and large anisotropies [114, 115, 116, 117].

The molecule studied in this work is the Er(trensal) [118, 119, 120].

4.2 Magnetic properties of Er(trensal)

The motivation behind this STM study of the self-assembly of Er(trensal) stems from synchrotron studies conducted at the EPFL-PSI X-treme beamline at the Swiss Light Source by members of our group. Studies of the magnetic properties of complex molecules on decoupling layers are still few [121, 122], and the subject is one of high interest.

The measurements show that while Er(trensal) molecules adsorbed on Ru(0001) have a very weak magnetic anisotropy, in the presence of a graphene (g) decoupling layer on Ru(0001) [123] and Ir(111) [124] the anisotropy becomes very large.

The structure of the Er(trensal) molecule, which is trigonal pyramidal, is shown in Fig. 4.1.

The Ru(0001) and Ir(111) surfaces were prepared by Ar⁺ sputtering and annealing at 1400 K. Graphene was grown by dosing 100 Langmuirs of C₂H₄ on the substrate kept at the annealing

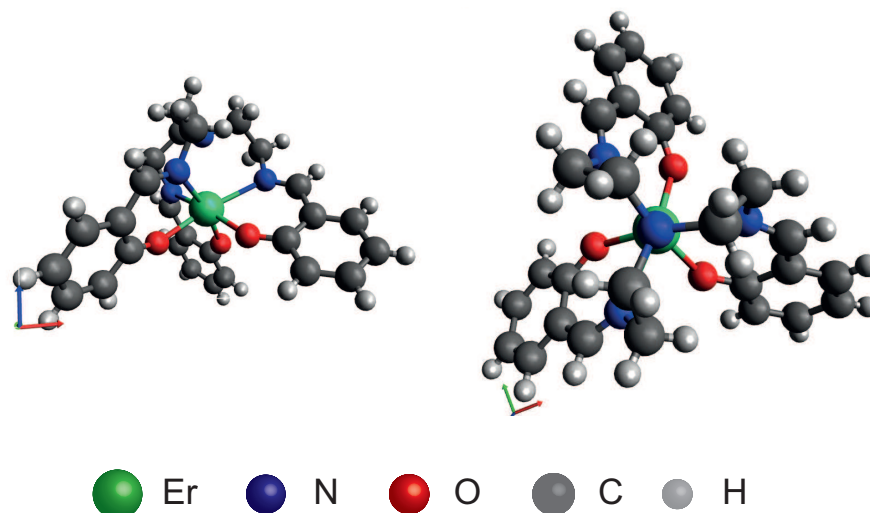


Figure 4.1: Structure of the Er(trensal) molecule, sideview and topview.

temperature; Er(trensal) molecules were evaporated at 560 K on the substrate kept at RT. A molecular monolayer is defined as the closely packed assembly formed by the molecules on g/Ru(0001) and on g/Ir(111) shown in Figs. 4.5(b) and (c). Figure 4.2 shows polarization dependent XAS spectra and corresponding XMCD measured at the $M_{4,5}$ adsorption edges of Er on 0.3 ML of Er(trensal)/g/Ru(0001). The XAS spectra at the M_5 edge show the typical three peaks originating from transitions from the $3d_{5/2}$ to the partially filled $4f$ levels. The strong XMCD signal reveals an intense Er magnetic moment. The fact that the signal is much stronger in normal than in grazing incidence indicates a strong magnetic anisotropy and an

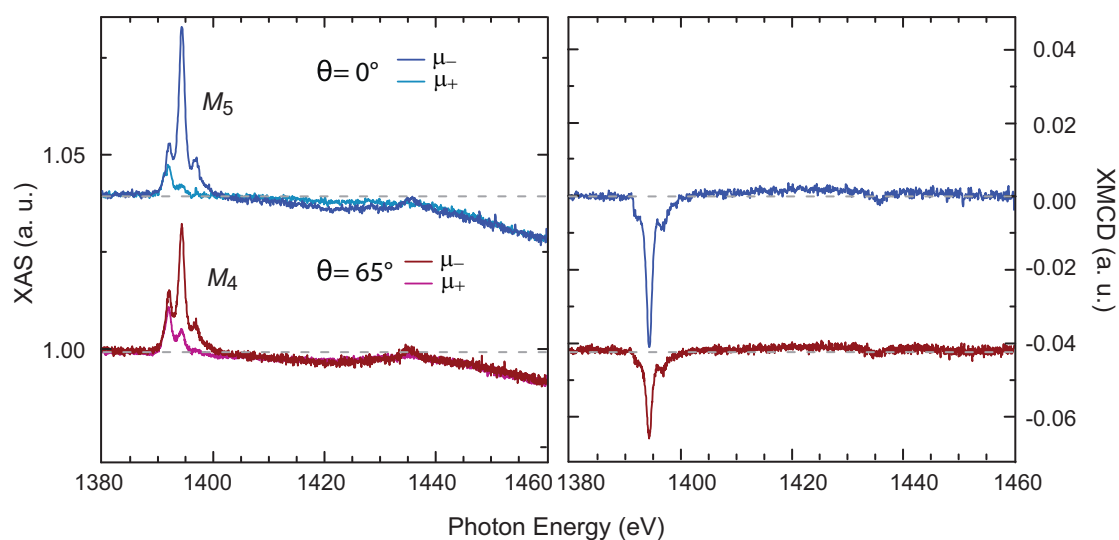


Figure 4.2: XAS and XMCD signal recorded at the $M_{4,5}$ adsorption edges of Er acquired on a sample with 0.3 ML of Er(trensal) on g/Ru(0001). Spectra are shifted for clarity. $T = 3$ K, $B = 6.8$ T collinear with the x-ray beam.

out-of-plane easy axis. Application of the sum rules [51, 52] reveals a total magnetic moment $\mu_{\text{tot}} = 7.2 \mu_B$ in normal and $\mu_{\text{tot}} = 4.1 \mu_B$ in grazing incidence.

The XAS and XMCD spectra recorded at the Er M_5 peak for samples with Er(trensal) on Ru(0001), on g/Ru(0001) on g/Ir(111) are shown in Fig. 4.3. A difference between the normal and grazing signal implies the presence of magnetic anisotropy, indicating that the molecules are organized on the surface. We can thus infer that the molecules are randomly distributed on Ru(0001) [Fig. 4.3(a)], but that the presence of the graphene decoupling layer results in the formation of self-assembled patterns both on g/Ru(0001) and on g/Ir(111) [Fig. 4.3(b) and (c)].

Accordingly, magnetization curves (Fig. 4.4) are almost identical in the case of Er(trensal)/Ru(0001) in normal and grazing incidence (panel a), while they show a strong angular dependence for submonolayer coverages of Er(trensal) on both g/Ru(0001) and g/Ir(111), as seen in panels (b) and (c). This indicates that the system has a strong anisotropy, such that in grazing incidence the maximum applied value of the magnetic field, 6.8 T, is not sufficient to completely orient the magnetic moments and saturation is not reached.

From an analysis of the magnetization curves using a spin Hamiltonian with Stevens parameters (not shown here) it is possible to see that the magnetic behavior of Er(trensal) molecules on g/Ru(0001) and on g/Ir(111) is the same as that of Er(trensal) in the molecular crystal [119].

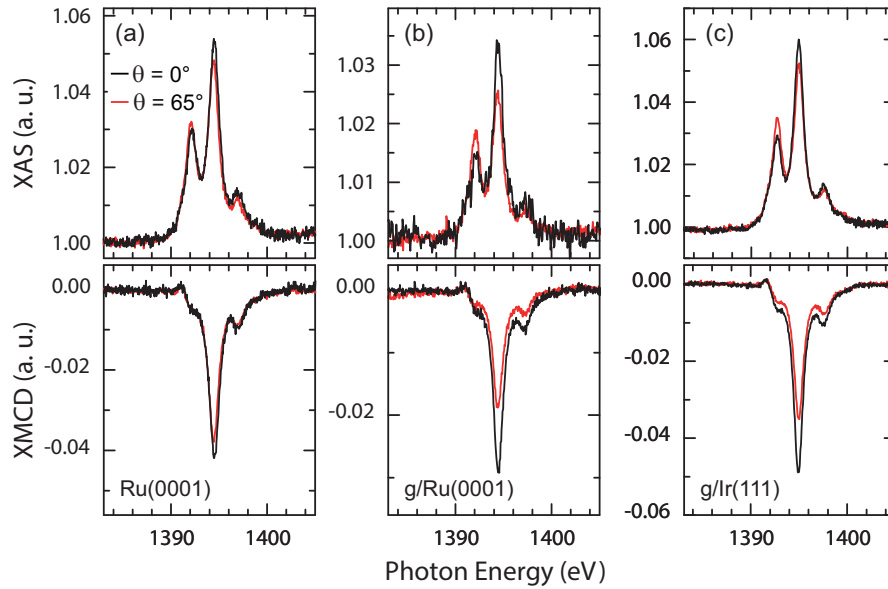


Figure 4.3: XAS and XMCD signal recorded at the Er M_5 edge at normal and grazing incidence, black and red lines respectively, for the following systems: (a) 0.3 ML of Er(trensal)/Ru(0001), (b) 1.2 ML of Er(trensal)/g/Ru(0001) and (c) 0.5 ML of Er(trensal)/g/Ir(111). In all panels, grazing incidence XMCD spectra were multiplied by a factor obtained from the ratio of the M_5 peak area in normal and grazing incidence to facilitate the comparison with normal incidence XMCD spectra. $T = 3$ K, $B = 6.8$ T collinear with the x-ray beam.

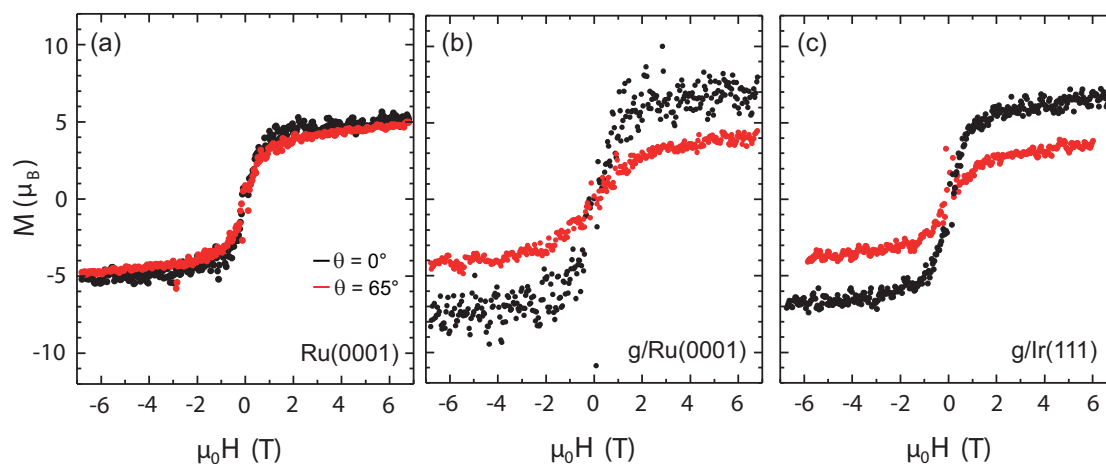


Figure 4.4: Magnetization curves as a function of the magnetic field recorded for normal and grazing incidence (black and red curves respectively) for the following systems: (a) 0.3 ML of Er(trensals) on Ru(0001), (b) 0.20 ML of Er(trensals) on g/Ru(0001) and (c) 0.25 ML of Er(trensals) on g/Ir(111). $T = 3$ K, $B = 6.8$ T collinear with the x-ray beam. The dots represent the amplitude of the M_5 XMCD peak divided by the pre-edge intensity.

4.3 STM measurements

To explain the magnetic behavior of the Er(trensals) molecules on the different substrates and to correlate the magnetic properties of the samples with the degree of molecular organization, we performed STM measurements on 0.25 ML of Er(trensals) molecules on Ru(0001), on g/Ru(0001) and on g/Ir(111).

Large and small scale images of the molecules deposited on the three substrates are presented in Fig. 4.5. Panel (a) shows clearly that on the bare ruthenium substrate the molecules do not organize, and have different adsorption configurations, which explain the absence of magnetic anisotropy for this sample. A more detailed analysis of the possible adsorption configurations of the molecules on Ru(0001) is displayed in Fig. 4.6. Figure 4.6(a) shows an STM image with enhanced contrast. We observe three kind of configurations: in most cases, the molecules have a sort of T shape which exhibits a chirality. These molecules are indicated with blue letters on the image, distinguishing between left and right chiral configuration. They might be adsorbed on one face of the pyramidal structure, with a phenyl leg pointing up. Other molecules, as the one indicated by the pink arrow, have a regular triangular shape and we interpret them as adsorbed with the C_3 symmetry axis perpendicular to the surface. Finally, there are molecules that show different appearances and that probably correspond to molecules randomly adsorbed on the surface. An analysis of the apparent heights of the different observed configurations, Fig. 4.6(b), reveals that most molecules have an apparent height of 0.245 nm, corresponding to the one of the T shaped molecules (peak indicated by the blue arrow on the histogram). A second smaller peak is observed at the apparent height of the triangular shaped molecules, 0.3 nm, indicated on the histogram with a pink arrow. Thus most molecules have their C_3 symmetry axis roughly parallel to the surface, and they are oriented along directions forming 120° with respect to each other. This explain the absence of a net

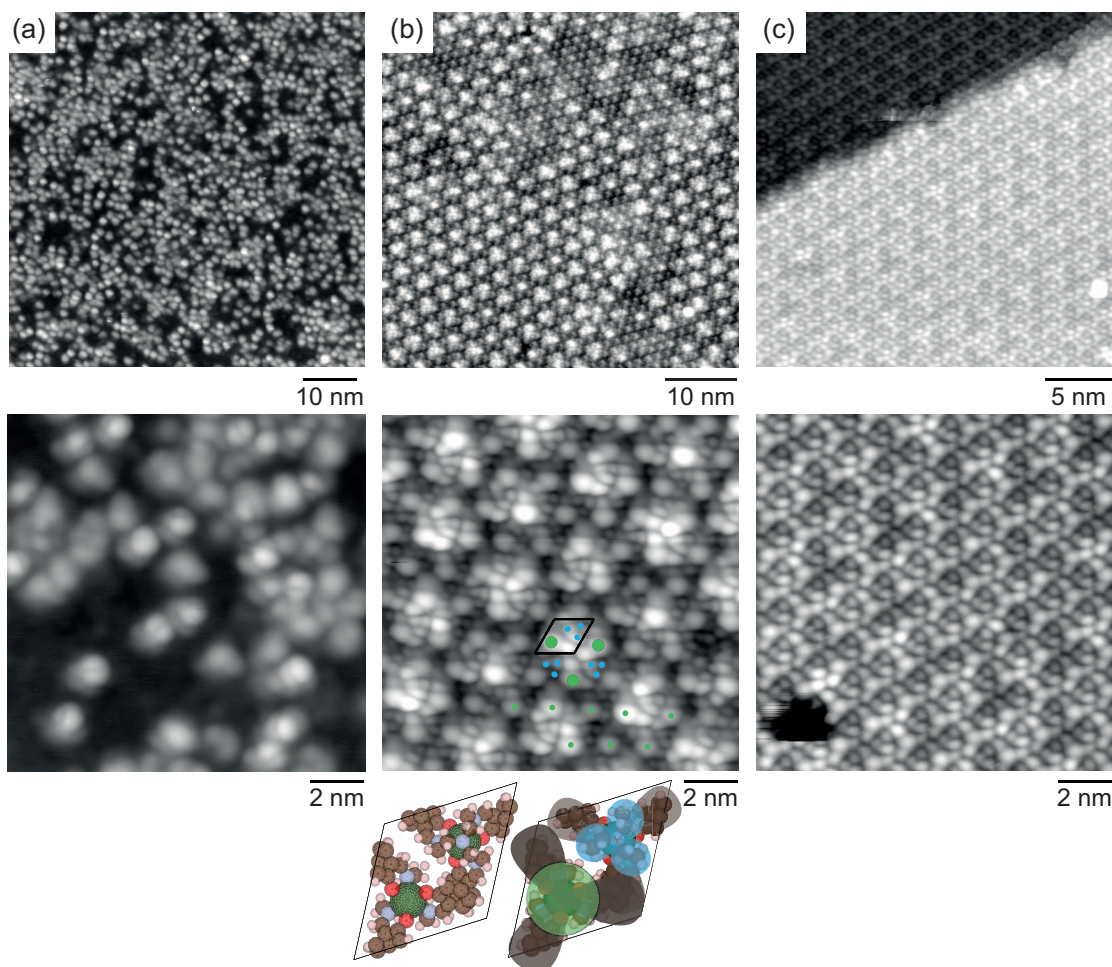


Figure 4.5: Large and small scale STM images of 0.25 ML of Er(trensal) on the following substrates: (a) Ru(0001) ($V_t = -300$ mV, $I_t = 50$ pA), (b) g/Ru(0001) ($V_t = -2.5$ V, $I_t = 30$ pA, large scale: $T_{\text{meas}} = 50$ K), (c) g/Ir(111) ($V_t = -2.5$ V, $I_t = 30$ pA). A sketch of the disposition of the molecules is shown, for clarity the main features are identified with colored circles that are reported on the STM image to facilitate the comparison.

magnetic anisotropy observed for this sample.

On the other hand, Fig. 4.5(b) and (c) show that on the graphene layer the molecules are organized in a highly ordered way. We note that in the presence of the graphene decoupling layer, the molecules are easily disturbed by the measurement, and entire islands can disappear after the scan, as in the example shown in Fig. 4.7. Graphene grown on Ru(0001) has a higher corrugation compared to g/Ir(111), thus in panel (b) the moiré is visible through the layer of molecules. In the large scale image the moiré is not perfect and in some areas is absent, so that the Er(trensal) molecules (small bright dots) are more easily visible. In the small scale image we can recognize a complex pattern of trigonal elements; its unit cell, indicated in black on the figure, has a lateral size of 13.6 ± 0.5 Å, virtually identical to that of a single crystalline sheet of the bulk structure of 12.95 Å. A careful analysis of the images reveals that, as in the molecular

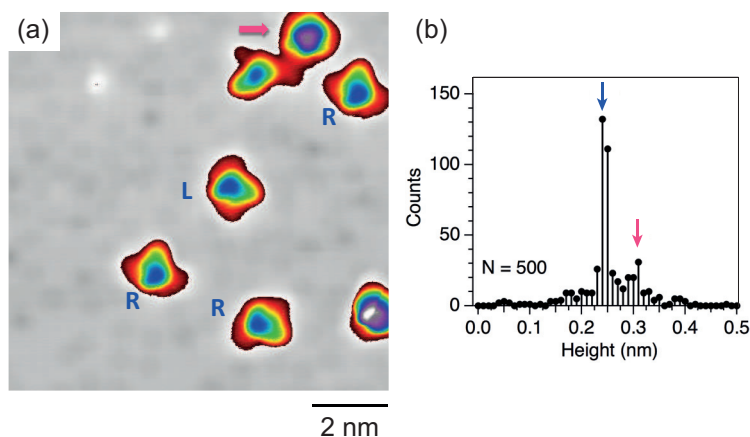


Figure 4.6: (a) High resolution image with enhanced contrast of Er(trensal) molecules on Ru(0001), accompanied by (b) a histogram of the apparent height of the molecules. N is the number of analyzed molecules. ($V_t = +1.5$ V, $I_t = 150$ pA).

crystal, the molecules are organized with their main axis pointing alternatively up and down, as shown in the sketch accompanying Fig. 4.5(b). To make the comparison clearer we highlighted the protruding features of the two molecules, pointing respectively up and down, with green and blue circles that we reproduced on the STM image. The assembly formed by Er(trensal) on g/Ir(111), Fig. 4.5(c) is easier to see thanks to the lower corrugation of the moiré compared to the one of g/Ru(0001) [124]. The molecular organization is exactly the same as on g/Ru(0001), leading to the conclusion that the moiré, unlike in other systems [125, 126, 106, 127], does not play any role in directing the assembly of the molecules. For both assemblies two chiral

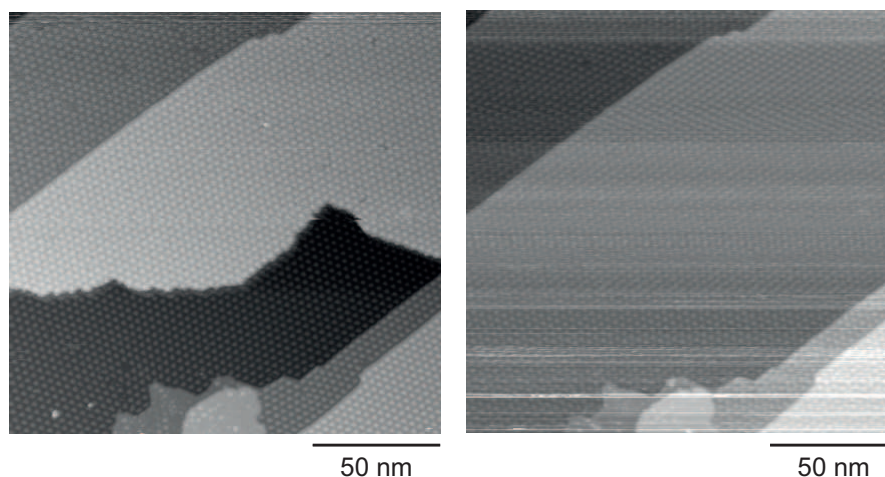


Figure 4.7: Successive images of 0.25 ML of Er(trensal) on g/Ru(0001). In the image on the left an island of Er(trensal) molecules extending on two substrate terraces is visible, but after one scan it has disappeared, as seen on the image on the right ($V_t = -700$ mV, $I_t = 20$ pA, $T_{\text{meas}} = 50$ K).

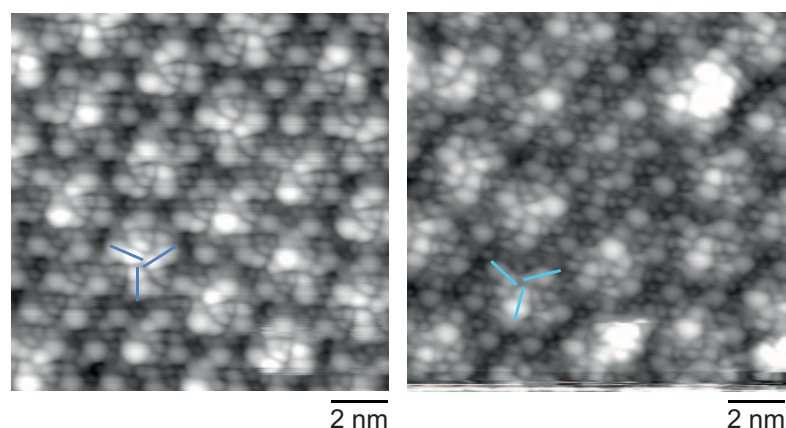


Figure 4.8: STM images showing the two chiral domains formed by Er(trensal)/g/Ru(0001) ($V_t = -2.5$ V, $I_t = 30$ pA).

domains are formed; an example for the case of Er(trensal)/g/Ru(0001) is shown in Fig. 4.8.

Thus, on both g/Ru(0001) and g/Ir(111) the molecules are organized with their C_3 symmetry axis normal to the surface, which is in perfect agreement with the observation that on both substrates a strong magnetic anisotropy is observed. The fact that the Er magnetic moment is higher in normal than in grazing incidence indicates that the magnetic easy axis is parallel to the C_3 axis of the molecules.

4.4 Conclusions

In conclusion, these results demonstrate that on Ru(0001) the molecule-surface interaction is strong, resulting in migration barriers that trap the molecules in their landing positions and in fix conformations. The presence of the graphene decoupling layer reduces such migration barriers, allowing the occurrence of molecular self-organization, which is driven in this case by molecule-molecule interactions. Unlike in other systems, the graphene layer does not provide a templating effect; in the present case the self-assembly is dominated by the $\pi - \pi$ interaction between the phenyl rings. The molecules assemble as in a layer of the bulk crystal, with their symmetry axes aligned in the direction normal to the surface, thus the anisotropy of the system is maximized.

Chapter summary

XAS and XMCD measurements show that Er(trensals) molecules:

- on Ru(0001) have low anisotropy
- on g/Ru(0001) have high anisotropy and out of plane easy axis
- on g/Ir(111) have high anisotropy and out of plane easy axis as well

STM measurements show that Er(trensals) molecules:

- on Ru(0001) have different adsorption configurations, mostly with their symmetry axes parallel to the surface
- on g/Ru(0001) self assemble in a regular structure
- on g/Ir(111) self assemble in a regular structure as on g/Ru(0001)

On g/Ru(0001) and on g/Ir(111) the molecules have the same magnetic properties and the same molecular organization as in the molecular crystal.



Part II:

Use of the networks as templates for the organization of metal atoms and clusters

5 Use of the molecular networks as templates

5.1 Introduction

Being able to induce the self organization of atoms and clusters is important, as magnetic and optical properties are often enhanced by a regular size and spatial distribution, and catalytic properties are strongly size-dependent. Well ordered nanostructure arrays can be created, for example, by the nucleation and growth on template surfaces exhibiting long period adatom binding energy variations, such as equidistant pinning sites [128], or networks of repulsive line defects [129]. Besides surface reconstructions and stress relief patterns of epitaxial thin films, nanoporous metal-organic networks [62, 88] are potential candidates for such templates. Decoration of the organic molecules themselves or of the coordination nodes [130] have both been reported, as well as adsorption of atoms within the cavities [131].

An additional source of order can be introduced by the 2D electron gas of the surface state mediating long-range adsorbate interactions [132, 133, 134]. On homogeneous surfaces they stabilize atomic superlattices [132, 133, 134, 135]. Surface state confinement results in local density of states (LDOS) patterns that influence the adsorbate binding energy. In 1D structures formed by substrate steps or strings of adsorbed atoms or molecules, this leads to 1D confinement of adsorbed atoms [136, 137, 138, 139]. It was demonstrated that the surface state LDOS patterns formed in a network of hexagonal molecular cavities influences the binding sites of adsorbed CO molecules [140].

In this chapter we will see how the metal-organic networks presented in Chapters 2 and 3 produce a confinement of the Cu(111) surface state, resulting in preferred adatom locations at the center of each cavity due to the LDOS pattern. Upon annealing, these atoms aggregate into a single cluster per network cavity, thus giving rise to a cluster array with the periodicity of the molecular template. We will see how we can produce in this way transition metal, rare earth metal and mixed clusters.

5.2 Confinement of the surface state

The confinement of surface state electrons in the cavities of the honeycomb network formed by NC-Ph₅-CN molecules is presented in Fig. 5.1. The dI/dV spectra, Fig. 5.1(a), show strong spatial dependence and the differential conductance maps reveal the LDOS patterns of the confined states [141, 142, 143], Fig. 5.1(b). The cavity geometry is close to the one of adatom

and vacancy islands of the (111) surfaces of Ag [144] and Cu [145], but in our case confinement is accomplished by the metal-organic network [101]. We can clearly discern five eigenstates identified and labeled as state 1, 2, 4, 7, and 10 [144]. The complexity of their spatial distribution increases with energy, as demonstrated by the dI/dV maps of Fig. 5.1(b). Notice that the threefold symmetry of the cavity, originating from the two types of coordination nodes, is also reflected in the DOS pattern. This effect is especially visible for states having more complex spatial distribution, as states 7 and 10. No quantum state coincides with the Fermi level E_F . However, state 4 at -70 mV has high intensity at the cavity center and thus contributes to the LDOS maximum at the center of the hexagon at E_F .

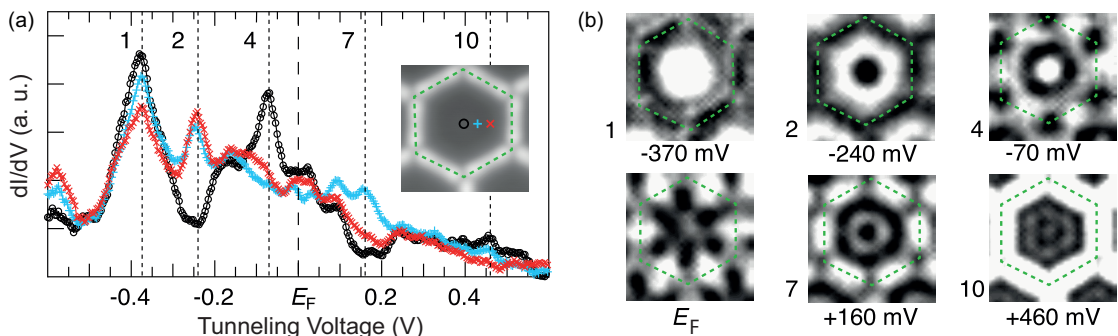


Figure 5.1: Confinement of the surface state in the NC-Ph₅-CN honeycomb network. (a) dI/dV spectra acquired on the locations in the hexagonal cavity indicated in the inset. (b) dI/dV maps recorded at the indicated voltages (setpoint: $V_t = -600$ mV, $I_t = 400$ pA, $V_{\text{mod}} = 10$ mV at 437 Hz). Adapted with permission from our paper, Ref. [103].

5.3 Deposition of Fe on the NC-Ph₅-CN honeycomb template

Deposition of minute amounts of Fe onto the metal-organic network at $T_{\text{dep}} \approx 10$ K leads to the coexistence of three species, as seen for the system with NC-Ph₃-CN molecules in Fig. 5.2 and for NC-Ph₅-CN in Fig. 5.3(a). Atoms landing in the hexagonal cavities stick on their site of impact without thermal diffusion toward the molecules. They appear as well localized protrusions (turquoise dashed circle). On the organic ligands two Fe-related features are discerned by their apparent height. The very bright features (yellow full circle) readily disappear through repeated STM imaging, even at moderate tunnel parameters, as illustrated in the set of subsequent STM images of Fig. 5.2. The results are alike for the template composed by the longer molecules. We systematically observe after the displacement of one of these bright objects that empty cavities in the immediate vicinity of the displaced element become occupied by a single atom. Thus the bright protrusions are identified as individual Fe atoms adsorbed onto the organic molecules. In contrast, the less bright features (see red dotted circle) are very robust against manipulation with the STM tip and attributed to Fe atoms below the organic molecules.

An Fe coverage of $\Theta = 3.5 \times 10^{-3}$ ML (1 ML is defined as one Fe atom per substrate Cu atom) deposited onto the NC-Ph₅-CN honeycomb network at $T_{\text{dep}} \approx 10$ K results in the system shown in Fig. 5.3(a). Considering the size of the network unit cell, one would expect 1.33 Fe atoms

5.3. Deposition of Fe on the NC-Ph₅-CN honeycomb template

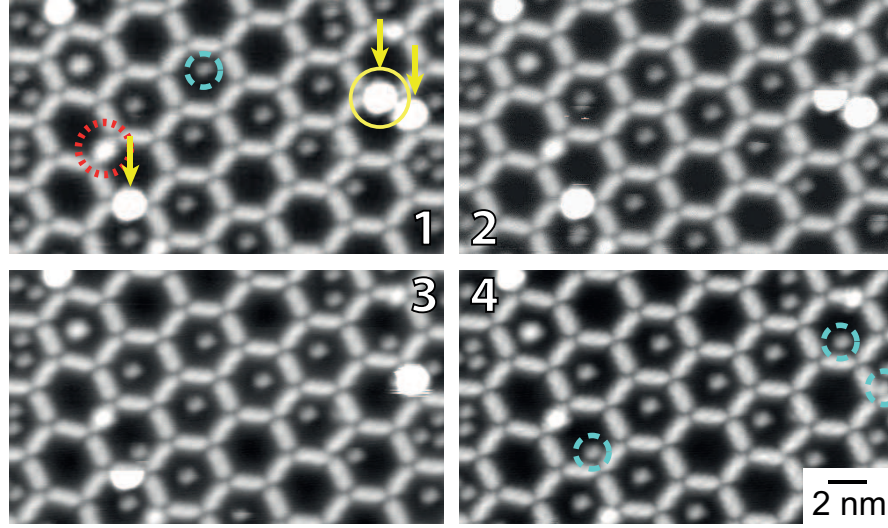


Figure 5.2: Sequence of consecutive images showing the successive descent of Fe atoms from on-top of NC-Ph₃-CN molecules down to the Cu(111) substrate ($\Theta = 7 \times 10^{-3}$ ML, $V_t = -300$ mV, $I_t = 50$ pA). Dashed turquoise circle: Fe atom on the substrate; solid yellow circle: Fe atom on-top of molecule; dotted red circle: Fe atom below molecule.

per hexagon at the used Fe coverage. From a statistical analysis carried out on more than thousand cavities, we find that there are only 1.03 ± 0.03 atoms. This number is expected if we remove the sites occupied by network components (23 %), leading to a inner cavity size of 293 sites. This result indicates that atoms landing on linkers and nodes do not diffuse to the pores. We also observe that $\approx 70\%$ of the atoms landing on molecules rebound, owing to a low sticking coefficient.

Statistical analysis yields the pore occupancy histogram presented in Fig. 5.3(b). The black dots show the filling expected from a binomial distribution $P(k, n, \Theta) = \binom{n}{k} \Theta^k (1 - \Theta)^{n-k}$, where Θ is the adatom coverage, n the inner cavity size expressed in substrate unit cells, and $k \in \{0, 1, \dots, 6\}$ the occupancy [129]. There is excellent agreement between experiment and binomial statistics, indicating that those adatoms landing on the substrate are trapped in the cavities.

Figure 5.3(c) reveals that the Fe atoms in pores with an occupancy $k \geq 2$ have preferred nearest neighbor distances and thus for $k \geq 3$ they form small patches of a superlattice. The origin of this ordering is the long-range oscillatory interaction mediated by the surface state electrons. The period of this interaction is given by half the Fermi wavelength of the surface state; the adatom nearest neighbor distance d_{nn} is the position of its first minimum given by the adatom scattering phase [132, 133] and the overlap with the short range repulsion inhibiting cluster formation [89, 134]. The formation of these patches at $T_{dep} \approx 10$ K is consistent with the reported experimental, 22 meV [146] and 23.8 meV [147], and theoretical, 25 meV [148], values for the diffusion barrier and with the short range repulsive barriers [146] for Fe adatoms on Cu(111). The mean distance deduced from the histogram shown in Fig. 5.3(c) is $d_{nn} = 1.1 \pm 0.1$ nm, in agreement with the values of 1.2 nm [146] and 1.1 nm [147] reported for Fe on bare Cu(111). The distance distribution is significantly narrower than the ones reported

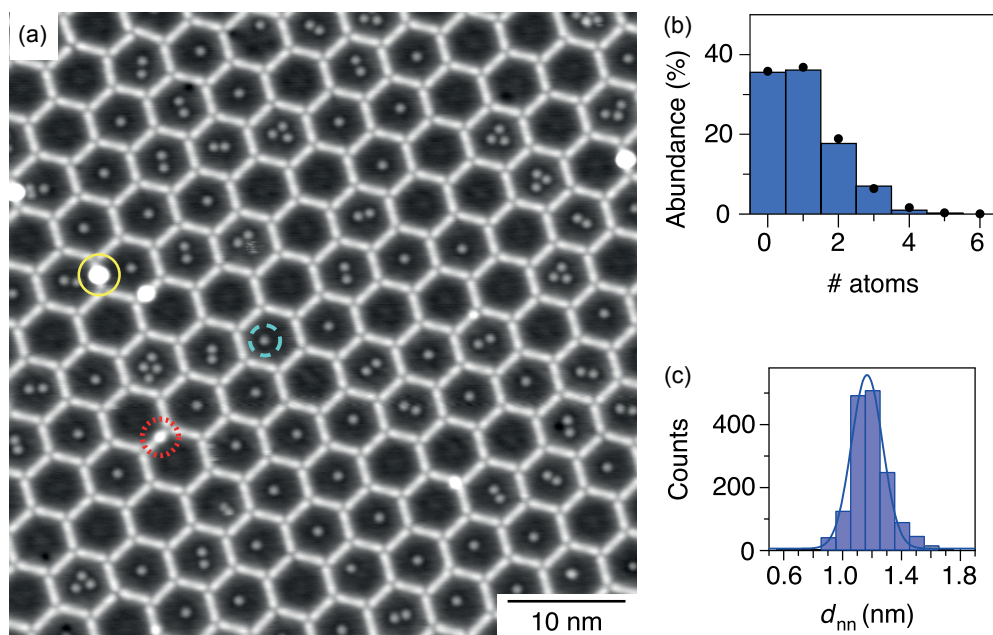


Figure 5.3: Fe adatoms on the NC-Ph₅-CN honeycomb template. (a) STM image showing $\Theta = 3.5 \times 10^{-3}$ ML of Fe on the honeycomb network, $T_{\text{dep}} \approx 10$ K ($V_t = -200$ mV, $I_t = 20$ pA). (b) Measured pore occupancy histogram (bars) and calculated binomial distribution (dots). (c) Nearest-neighbor distance histogram for cavity occupation above one. Solid line is a Gaussian fit. Adapted with permission from our paper, Ref. [103].

for adatom superlattices on free surfaces, providing experimental evidence for the predicted enhancement of the surface state mediated interaction by its confinement [149].

Further inspection of Fig. 5.3(a) reveals that the Fe atoms, as well as the center of mass of the dimers and trimers, are centered in the cavities, and that the assemblies show preferred orientations. Figure 5.4 shows the Fe adsorption site statistics, in the form of 2D plots and of normalized radial abundance with respect to the quasi-hexagon center. The normalization compensates for the increasing number of adsorption sites per bin with increasing radius. The results for single occupancy are shown in Fig. 5.4(a). Random distribution would give rise to the horizontal dashed line, while the observed positions are strongly peaked in the cavity center. The inset displays a 2D plot where each black dot represents a measured Fe position. The dots are isotropically distributed in the immediate vicinity of the center. The results for cavities occupied by two Fe atoms are presented in Fig. 5.4(b). The radial histogram exhibits a broad peak centered at 0.5 nm. The adsorption site map indicates that the pairs occupy the center of the cavity, while keeping their preferential distance of 1.1 nm; the dimers show no preferential azimuthal orientation. The radial distribution of cavities hosting three Fe atoms, Fig. 5.4(c), shows a broad peak at 0.65 nm, in agreement with the value expected for adatoms occupying the vertices of an equilateral triangle of 1.1 nm side centered in the cavity. Moreover, the two-dimensional map reveals a preferential azimuthal orientation with threefold symmetry. The adatom position distribution observed in Fig. 5.4(c) reflects the threefold symmetry of the cavity. The preferred triangle orientation is such that the adatoms

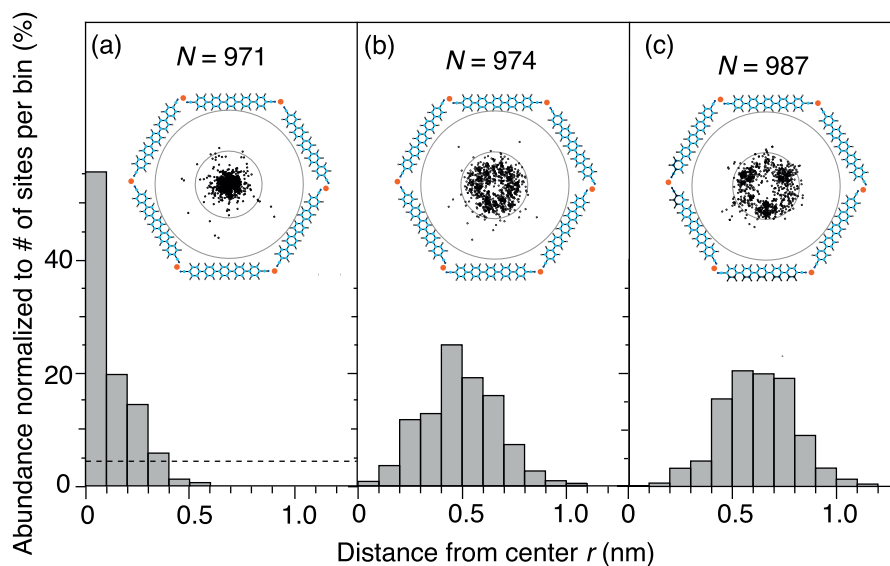


Figure 5.4: Positioning of the Fe adatoms in the NC-Ph₅-CN hexagonal cavities. Radial distribution histograms normalized to the number of adsorption sites for each bin and 2D plots of adatom positions for occupancies of (a) one, (b) two, and (c) three Fe atoms. N is the number of analyzed adatoms. Each dot represents the measured position of one atom, the plotted circles have radii of $r = 1.0$ and 2.2 nm. Adapted with permission from our paper, Ref. [103].

are close to the short hexagon sides. The isotropic dimer distribution can be understood taking into account the incompatibility of twofold dimer and threefold cavity symmetry. We attribute the steering of Fe adatoms towards the cavity center to the fact that the LDOS at E_F has a maximum there [133, 149, 138]. For cavities hosting more than one adatom, the superposition of two attractive potentials has to be considered, one arising from the confinement due to the molecules, the other created by the adatoms themselves [137, 139].

5.3.1 Cluster formation

Figure 5.5(a) shows a sample prepared like the one discussed so far, but with double coverage, thus with an average of 2.06 atoms per cavity. The occupation histogram in Fig. 5.5(c) follows again a binomial distribution. Figure 5.5(b) shows the same sample after annealing to 18 K. Almost all the occupied cells (97 %) host now a single object, while the proportion of empty pores is unchanged, see red bars in Fig. 5.5(c). As for the adatoms before annealing, also the clusters are preferentially located at the center of the hexagon, as demonstrated by the plot of cluster positions in Fig. 5.5(d). Moreover, the number of adatoms/clusters adsorbed on the molecules has not changed significantly after annealing.

In Fig. 5.5(e) we show the apparent height histogram of the Fe atoms before the annealing, shown with blue dots. The apparent height distribution of the clusters obtained after annealing is displayed as red circles. The number and apparent height of single atoms before and after annealing is identical, therefore the number of singly occupied cavities remained unchanged. Remarkably, additional well distinct peaks in the apparent height distribution are visible at 85, 112, and 137 pm. They are identified as dimer, trimer, and tetramer clusters respectively,

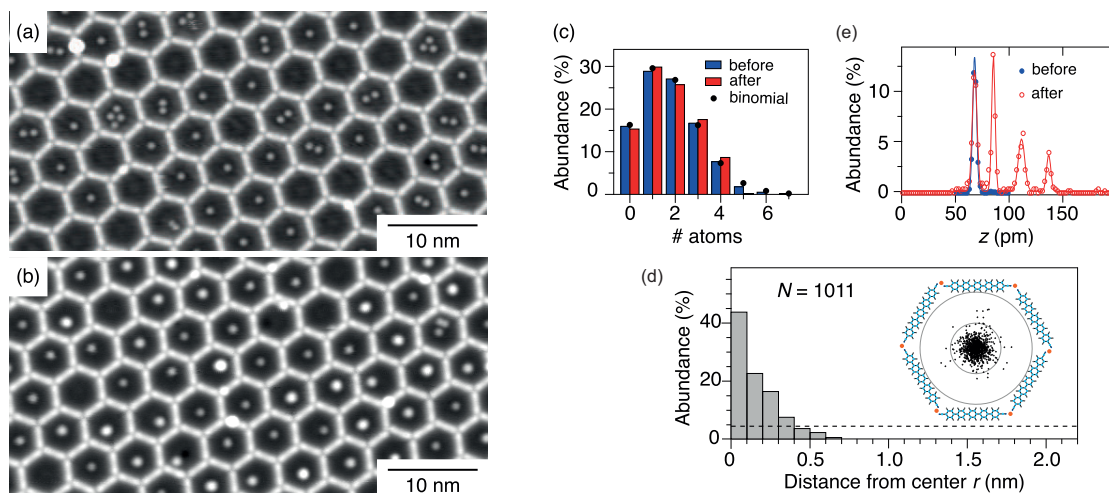


Figure 5.5: Cluster formation. STM images of Fe on NC-Ph₅-CN template before (a) and after (b) annealing at 18 K ($\Theta = 7.0 \times 10^{-3}$ ML, $V_t = -500$ mV, $I_t = 50$ pA). (c) Measured occupancy histogram before and after annealing (bars) compared with calculated binomial distribution (dots). (d) Positions of the Fe clusters in the cavity, as in Fig. 5.4. (e) Apparent height histogram before and after annealing. Adapted with permission from our paper, Ref. [103].

as the peak areas are in agreement with the cavity occupancy before annealing, see the red bars in Fig. 5.5(c). Thus, at the chosen annealing temperature the thermal energy is enough for the Fe adatoms to overcome the repulsive barrier and to aggregate, consistently with the observations reported for Fe on bare Cu(111) [146, 147].

5.3.2 Higher Fe coverage

When the Fe coverage is increased to four times the value of the sample in Fig. 5.5, to $\Theta = 28 \times 10^{-3}$ ML, most of the pores are filled with small patches of ordered superlattice, as seen in Fig. 5.6(a). However, a number of clusters are also found in the pores. When a cluster is already present in the pore, upon annealing it tends to remain separate from the cluster formed by the other atoms present in the same cavity, so an annealing at 20 K gives the results presented in Fig. 5.6(b). Many pores contain two or even three clusters, and no ordered cluster array is formed. To obtain a sample with well organized clusters it is necessary to proceed in successive steps, evaporating a small quantity of Fe atoms, $\Theta = 7 \times 10^{-3}$ ML, annealing at 20 K, depositing more Fe and annealing again until the desired coverage is reached. The result of such a procedure for a total coverage of $\Theta = 28 \times 10^{-3}$ ML is shown in Fig. 5.6(c), and for $\Theta = 56 \times 10^{-3}$ ML in Fig. 5.6(d). Figures 5.6(e) and (f) show the expected filling of the pores (and thus the distribution of cluster sizes) calculated with a binomial distribution for the two coverages.

5.3.3 Fe deposition at 18 K

Deposition of Fe on the sample kept at a temperature between 18 and 50 K results in the adsorption of all Fe atoms under the molecules, thanks to the activation of Fe diffusion within

5.3. Deposition of Fe on the NC-Ph₅-CN honeycomb template

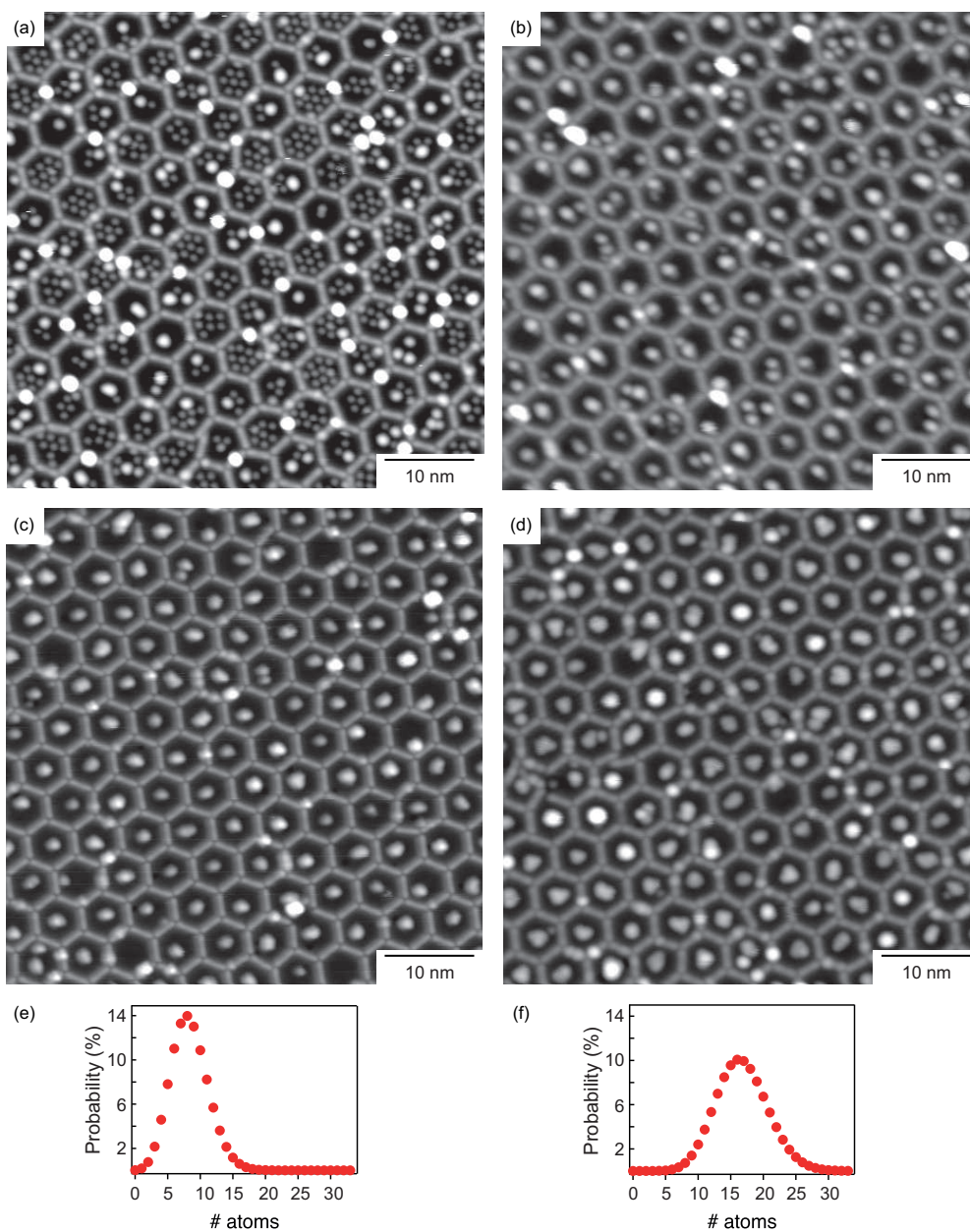


Figure 5.6: Higher Fe coverages on NC-Ph₅-CN honeycomb template. (a) STM image of the system obtained after deposition of $\Theta = 28 \times 10^{-3}$ ML of Fe and (b) same system after annealing at 20 K. (c) Sample obtained by four subsequent depositions of $\Theta = 7 \times 10^{-3}$ ML and annealing at 20 K (total coverage $\Theta = 28 \times 10^{-3}$ ML). (d) Same sample after four more depositions and annealings (total coverage $\Theta = 56 \times 10^{-3}$ ML). (e) and (f) expected pore occupancy as obtained with a binomial distribution for coverages corresponding to (c) and (d), respectively. Tunneling parameters for all STM images: $V_t = -500$ mV and $I_t = 50$ pA.

the cavities, Fig. 5.7. This observation leads us to the conclusion that the buried adsorption site is the most stable one, while the other two, on the substrate and on top of molecules,

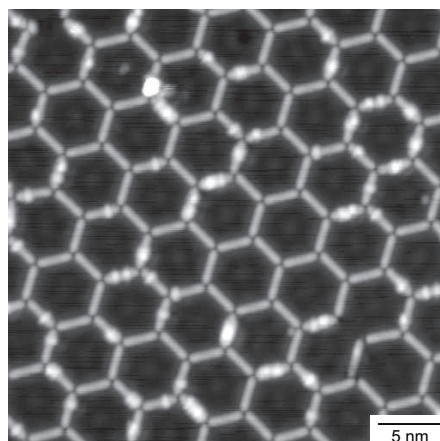


Figure 5.7: Deposition of Fe at a temperature $50 \text{ K} > T_{\text{dep}} > 18 \text{ K}$ leads to decoration of the molecules by Fe atoms adsorbed below them. $\Theta = 7 \times 10^{-3} \text{ ML}$, $T_{\text{dep}} = 32 \text{ K}$ ($V_t = -3 \text{ mV}$, $I_t = 100 \text{ pA}$).

are metastable [150]. The most likely adsorption site for the Fe atom is under the second (or fourth) phenyl ring of the molecule, with an overall probability of 88%, while the central and extremal rings account for the absorption of about 5% of the atoms each. Thus, the network can be used as a template also for the organization of atoms under the molecules. We observe, however, that under many molecules two atoms, or a small cluster, are found.

5.3.4 Thermal stability

To investigate the thermal stability of the cluster array in the metal-organic network we annealed the sample at different temperatures. The STM image in Fig. 5.8(a) demonstrates

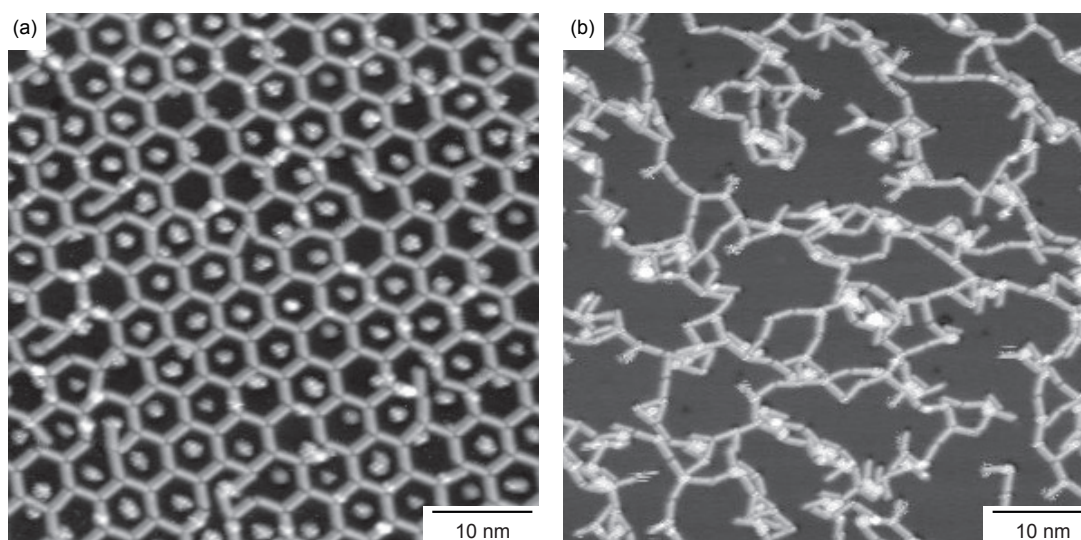


Figure 5.8: Thermal stability. STM images of the system after annealing at (a) 78 K and (b) 300 K. For both images $\Theta = 28 \times 10^{-3} \text{ ML}$, $V_t = -500 \text{ mV}$, $I_t = 50 \text{ pA}$, $T_{\text{meas}} = 78 \text{ K}$.

that the system is stable up to a temperature of 78 K, even though some defects start to appear and some molecules are displaced. Owing to the characteristics of our STM we cannot perform controlled annealing at any temperature, thus we cannot test what happens if the sample is heated at an intermediate temperature between that of liquid nitrogen and room temperature. What we know is that after annealing the system at RT for five minutes the honeycomb network disappears and at its place a disordered pattern is formed, probably with both Cu and Fe coordination, Fig. 5.8(b). If the Fe did not participate to the formation of the metal-organic structure we would expect to observe a honeycomb network as in the case of annealing of RT of NC-Ph₃-CN molecules without co-deposited Fe adatoms, as in Fig. 3.11 in Chapter 3. Thus, we can establish an inferior limit of 78 K and a superior one of 300 K for the thermal stability of the array of Fe cluster hosted in the NC-Ph₅-CN honeycomb network.

5.3.5 Other NC-Ph₅-CN networks used as templates

Also the networks formed by NC-Ph₅-CN molecules upon deposition on the substrate kept at lower temperature, see Chapter 3, confine the Cu(111) surface state, inducing the adatom and cluster organization. Figure 5.9(a) shows the differential conductance spectra acquired in the pores of the truncated triangular network, on the locations indicated in the inset. We can see that also in this system different eigenstates can be discerned, labeled 1, 2 and 4. Their spatial distribution is revealed by the differential conductance maps shown in Fig. 5.9(b). As for the honeycomb network, near the Fermi energy the LDOS has a maximum in the center of the cavities. Thus, also for this network deposition of Fe atoms results in the organization of the atoms at the center of the cavities, Fig. 5.10. The neat organization of the atoms in the pores can be appreciated in Fig. 5.10(a), but is particularly evident in the radial distribution histogram and in the plot of the adatom positions into the pores shown in Fig. 5.10(b). The kagome and the triangular networks also induce the self organization of the Fe atoms that, also on these networks, tend to occupy the center of the pores, as can be seen on the STM images presented in Fig. 5.11.

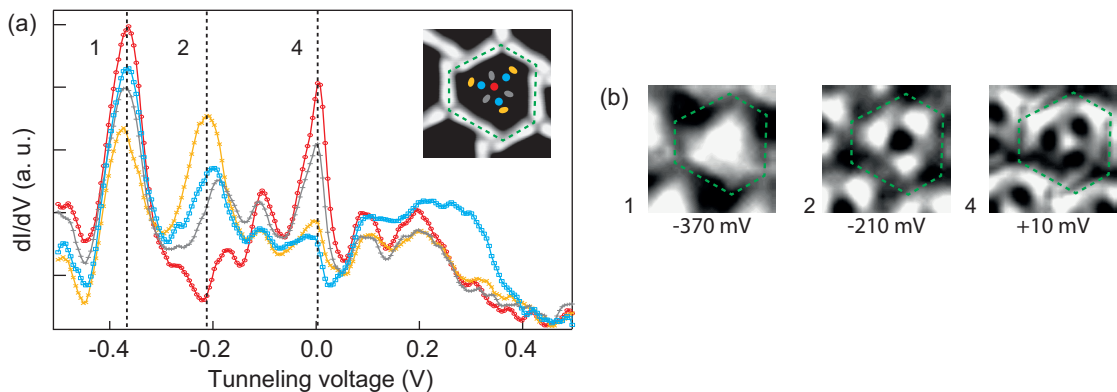


Figure 5.9: Surface state confinement in the truncated triangular network. (a) dI/dV spectra acquired on the locations in the cavity indicated in the inset. (b) dI/dV maps recorded at the indicated voltages (setpoint: $V_t = -500$ mV, $I_t = 400$ pA, $V_{\text{mod}} = 10$ mV at 467 Hz).

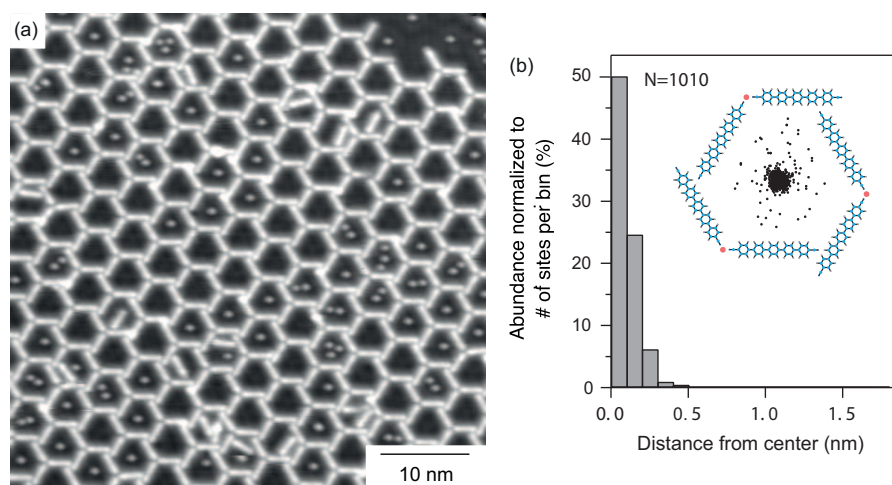


Figure 5.10: Self organization of Fe atoms in the truncated triangular template. (a) STM image, $V_t = -200$ mV, $I_t = 20$ pA, $\Theta = 3.5 \times 10^{-3}$ ML. (b) Radial distribution histogram normalized to the number of adsorption sites for each bin and 2D plot of the adatom positions into the cavities for pores occupied by a single atom.

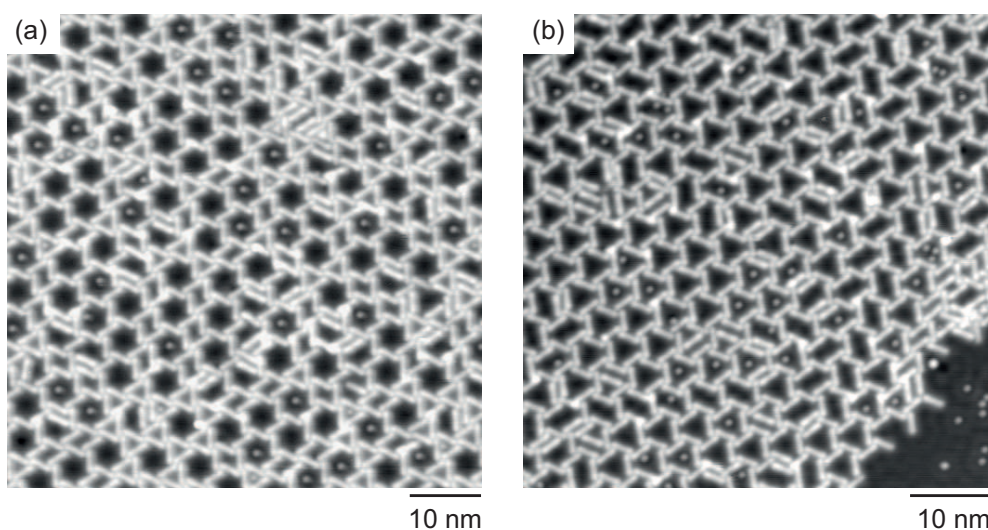


Figure 5.11: Self organization of Fe atoms in the cavities of the kagome (a) and triangular (b) networks. For both STM images $V_t = -200$ mV, $I_t = 20$ pA, $\Theta = 3.5 \times 10^{-3}$ ML.

5.4 Deposition of Fe on the NC-Ph₃-CN honeycomb template

The honeycomb network formed by NC-Ph₃-CN molecules has a periodicity of 3.38 nm, compared to the 4.97 nm of the NC-Ph₅-CN one. Smaller cavities mean that the confined states in the quantum well are shifted toward higher energies. The result is that we cannot detect them as nicely as in the case of the longer molecules, and that there is not such a strong LDOS maximum at the center of the hexagons. As we shall see, this changes the properties of the network when it comes to using it as a template for the organization of metal clusters.

5.4. Deposition of Fe on the NC-Ph₃-CN honeycomb template

Deposition of Fe at $T_{\text{dep}} \approx 10$ K gives similar results as with the bigger template, Fig. 5.12, with the atoms landing in the cavities sticking on their site of impact, Fig. 5.12(a), a cavity occupation following a binomial distribution, Fig. 5.12(b), and a most likely distance between neighboring atoms of 1.1 nm, Fig. 5.12(c). The atoms landing on molecules, owing to a low sticking coefficient, adsorb only in $\approx 30\%$ of cases.

There is also in this system a clear tendency for atoms to adsorb in the center of the cavities, and in the case of two or three atoms in a single cavity to organize in order to have the center of mass on the center of the hexagon. A statistical analysis of the position of the atoms in the template cavities, analogous to that shown in Fig. 5.4, is shown in Fig. 5.13. In singly occupied cavities the atomic positions are a bit more scattered than in the bigger template, which we attribute to the fact that the network is less regular, thus different cavities have slightly different shapes and center positions.

The influence of the different confinement of the surface state with respect to the NC-Ph₅-CN network can be clearly seen upon attempting to produce Fe clusters in the network cavities. Annealing at 18 K for 1 min gives a result that is quite different from the one obtained with the NC-Ph₅-CN template. While with the longer molecules all atoms remain in the cavities, either forming clusters or as single atoms, when the shorter ligands are used to constitute the template only about half of the atoms are found in the cavities after the annealing. The rest diffuses under the molecules. We can draw the conclusion that in this system the attraction toward the center of the cavity is comparable with the attraction atoms feel toward the stable adsorption position under molecules. Thus the network formed by NC-Ph₃-CN is not a good template for steering the organization of Fe clusters in the cavities. However, as we will see

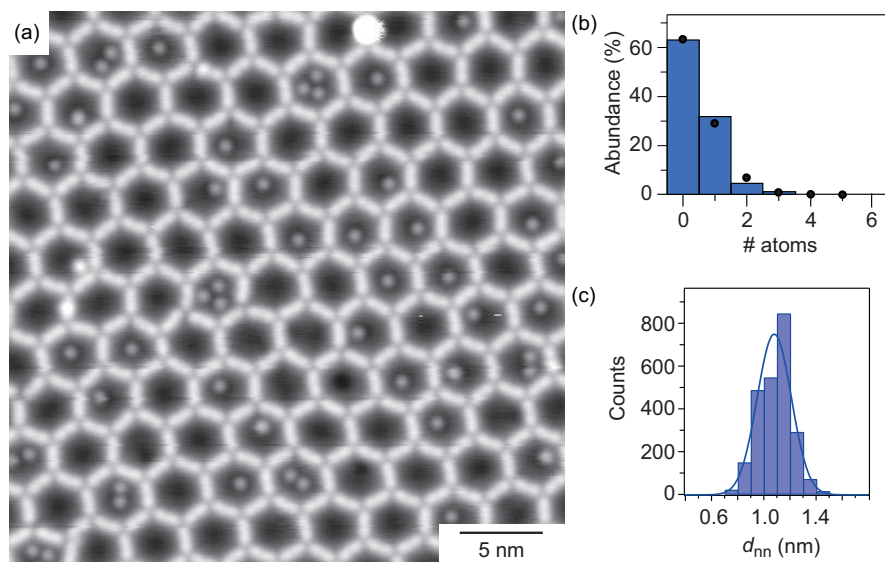


Figure 5.12: Fe adatoms on the NC-Ph₃-CN honeycomb template. (a) STM image showing individual Fe adatoms in the cavities of the network ($\Theta = 3.5 \pm 0.1 \times 10^{-3}$ ML, $V_t = -200$ mV, $I_t = 100$ pA). (b) Measured occupancy histogram (bars) and calculated binomial distribution (dots). (c) Nearest-neighbor distance histogram for cavity occupation above one.

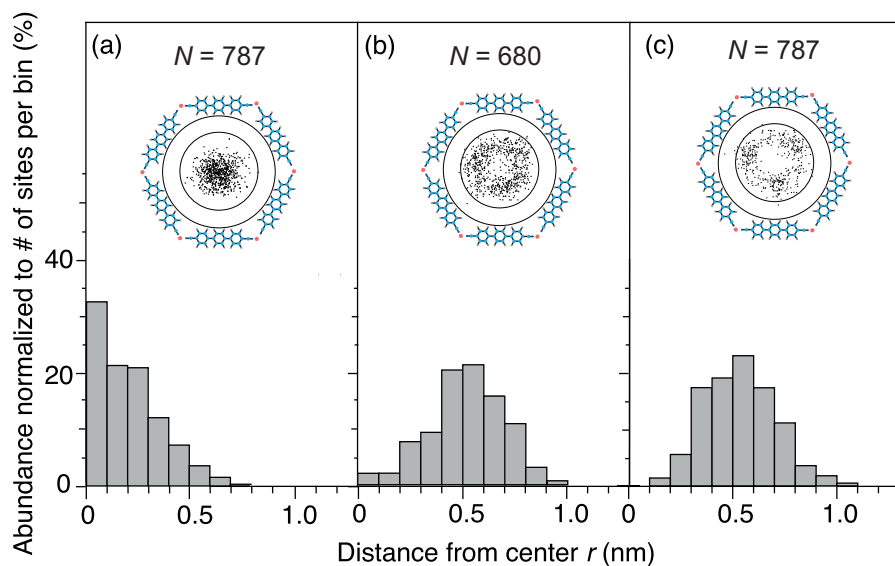


Figure 5.13: Positioning of the Fe adatoms in the NC-Ph₃-CN hexagonal cavities. As in Fig. 5.4, position of the Fe adatoms in the pores for occupancies of (a) one, (b) two, and (c) three Fe atoms. N is the number of analyzed adatoms. The radial distribution histograms are normalized to the number of adsorption sites for each bin. Circles on the adatom position plots have radii $r = 1.0$ and 1.44 nm.

in Chapter 7, is a very good choice for the production of a well organized array of Kondo impurities.

Deposition of Fe at a temperature between 18 and 50 K results, as with NC-Ph₅-CN, in a sample

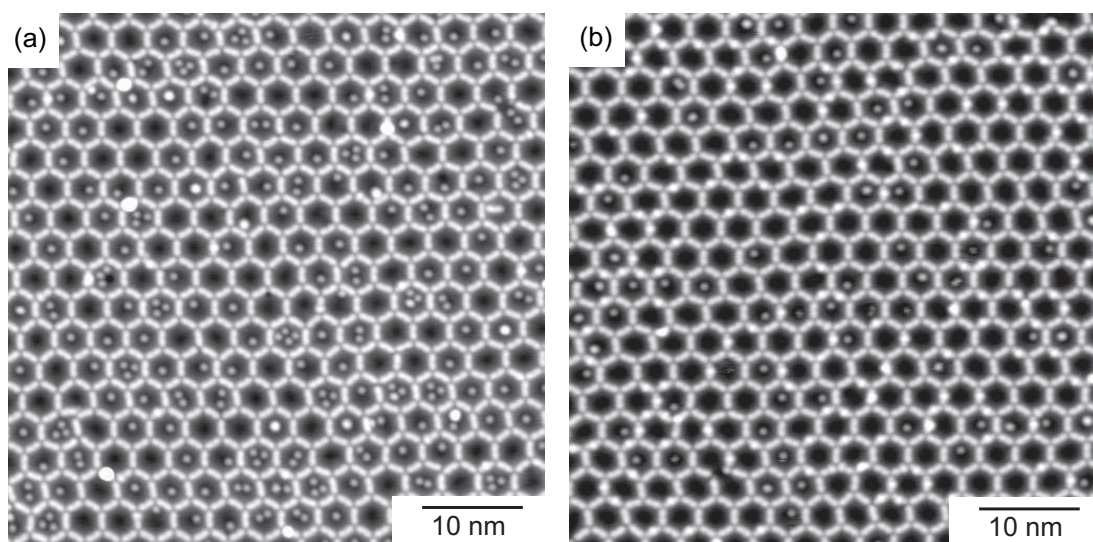


Figure 5.14: Annealing at 18 K. STM images of Fe on the NC-Ph₃-CN honeycomb template before (a) and after (b) annealing at 18 K for 1 minute. ($\Theta = 6.0 \times 10^{-3}$ ML, $V_t = -100$ mV, $I_t = 50$ pA).

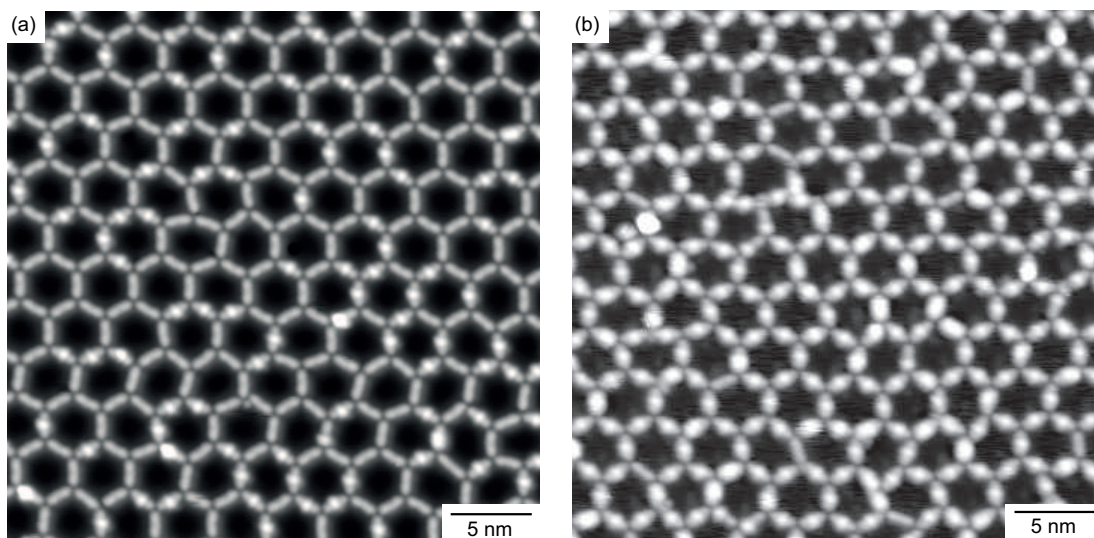


Figure 5.15: Deposition of Fe at a temperature $50 \text{ K} > T_{\text{dep}} > 18 \text{ K}$ leads to decoration of the molecules by Fe atoms adsorbed below. (a) $\Theta = 6 \times 10^{-3} \text{ ML}$, $T_{\text{dep}} = 20 \pm 2 \text{ K}$ ($V_t = -50 \text{ mV}$, $I_t = 300 \text{ pA}$) (b) $\Theta = 18 \times 10^{-3} \text{ ML}$, $T_{\text{dep}} = 50 \pm 2 \text{ K}$ ($V_t = -500 \text{ mV}$, $I_t = 100 \text{ pA}$, $T_{\text{meas}} = 50 \text{ K}$).

with all the atoms adsorbed under the molecules, Fig. 5.15(a). While for the longer molecules the preferred absorption site for Fe atoms is under the second (or fourth) phenyl ring, for the shorter ligands the central ring is by far the most likely one for the adsorption of Fe atoms (97%). By increasing the Fe coverage we can obtain a network where we have more or less an atom under each molecule, Fig. 5.15(b), even though the metal-decorated network is not perfect owing to the presence of undecorated molecules and of small Fe clusters under some ligands. As we shall see in Chapter 7, the Fe atoms adsorbed under the molecules have very interesting magnetic properties, and being able to organize them in a regular pattern is an important result.

5.5 Co clusters on NC-Ph₅-CN honeycomb template

We used the NC-Ph₅-CN honeycomb template also for inducing the organization of Co atoms and clusters. The deposition of $6 \times 10^{-3} \text{ ML}$ of Co atoms on the network results in a sample similar to the one obtained with Fe, shown in Fig. 5.16(a). Also in this case the atoms or groups of atoms do not diffuse toward the molecules, but rather organize in the cavities forming regular geometries around the center. However, annealing at 18 K, that for Fe is sufficient to make atoms agglomerate into clusters inside the cavities, has little effect in the case of Co, Fig. 5.16(b). This is expected, as the diffusion barrier for Co atoms on Cu(111) is calculated to be 37 meV [151], compared to the $\approx 25 \text{ meV}$ of Fe on the same substrate [148, 146, 147]. Therefore, the thermal energy at 18 K is not sufficient to activate atom migration and the formation of clusters. Successful cluster formation is obtained upon annealing at a temperature of 50 K. As in the case of Fe, also Co clusters tend to be centered in the honeycomb cavities, Fig. 5.16(c). However, the higher annealing temperature produces contamination of some of the Co atoms,

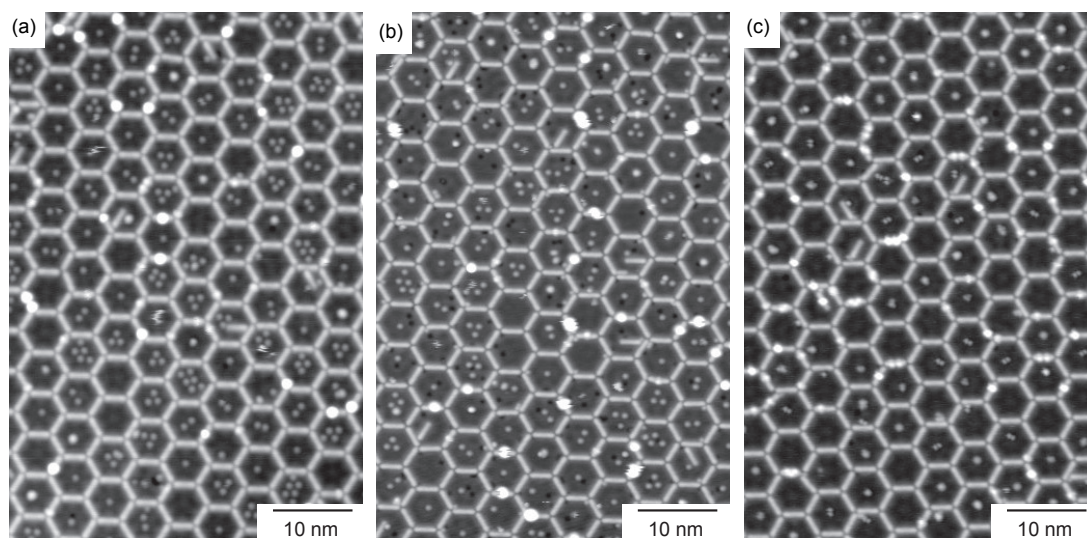


Figure 5.16: Co on NC-Ph₅-CN honeycomb network. The system before annealing (a), after annealing at 18 K (b) and after annealing at 50 K (c). $\Theta = 6.0 \times 10^{-3}$ ML, $V_t = 50$ mV, $I_t = 20$ pA.

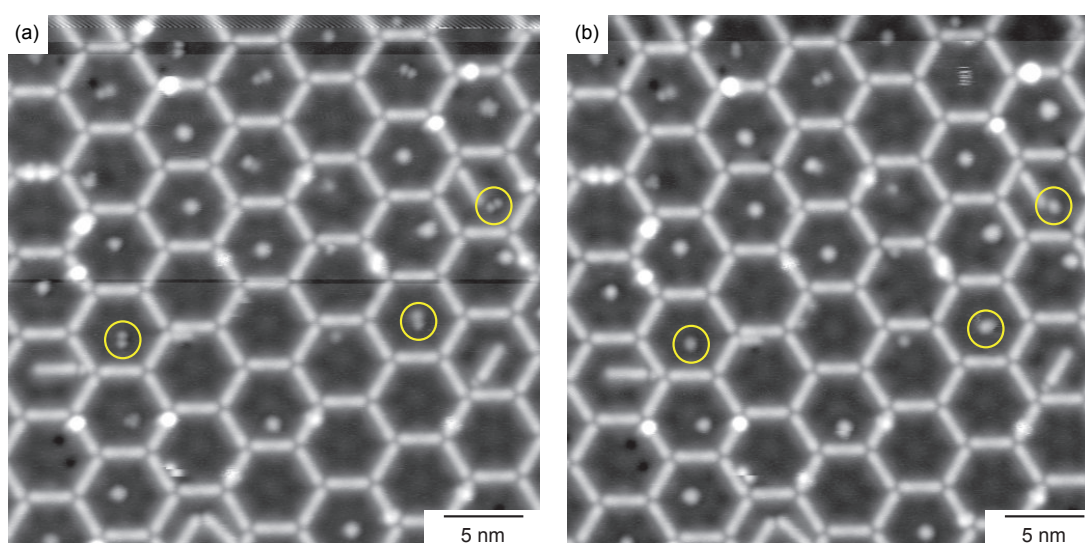


Figure 5.17: Contamination of Co atoms. Co on NC-Ph₅-CN honeycomb network after annealing at 50 K for 1 minute, before (a) and after (b) a pulse of -2 V. The appearance of the objects in the yellow circles is transformed from that of a double dot to a round shape ($V_t = 50$ mV, $I_t = 20$ pA).

as the ones marked in the yellow circles in Fig. 5.17(a), that appear as pairs of small dots. These objects recover the appearance of single atoms when a pulse of -2 V is applied: the atoms in Fig 5.17(b) were cleaned from their contaminants with a single pulse applied in a corner of the image. The most likely source of this contamination is H atoms [152].

5.6 Er clusters on NC-Ph₅-CN honeycomb template

As a next step, we moved from transition metals to rare earth elements, which exhibit appealing magnetic properties [153]. To exploit these properties, it would be beneficial to be able to induce their self-organization in regular patterns. With this in mind, we evaporated Er atoms on the NC-Ph₅-CN honeycomb template. Evaporation of 3.5×10^{-3} ML of Er on the sample kept at 10 K results in the organization shown in Fig. 5.18. One can immediately see that the atoms disposition is not as regular as in the case of Fe and Co atoms. As a first point, there are many more atoms adsorbed on top of molecules, as the one in the yellow circle, and a number of atoms, as the one in the red circle, are adsorbed in the cavity in off-center positions, probably because of adsorbates present on the surface acting as pinning sites. Moreover, some clusters are already present, see blue circle. However, the general tendency of the adatoms to organize around the center of the cavities seen for Fe and Co is clearly present. We note that the atoms adsorbed on molecules, unlike in the systems seen up to now, are very stable against manipulation and are not displaced during measurements, even by scanning at relatively high bias voltage (+700 mV). The occupancy histogram shown along with the STM image in Fig. 5.18 reveals that also for this system the occupancy of the cavities follows a binomial distribution.

The sequence of images in Fig. 5.19 shows that imaging is strongly bias dependent. In Fig. 5.19(a) a relatively high negative bias voltage is used ($V_t = -500$ mV): the atoms adsorbed on the substrate appear very small, owing to a repulsive interaction with the STM tip. In areas of the sample where the cavities are bigger than the honeycomb ones adatoms are not visible in this tunneling conditions. In Fig. 5.19(b), $V_t = +500$ mV, the opposite phenomenon

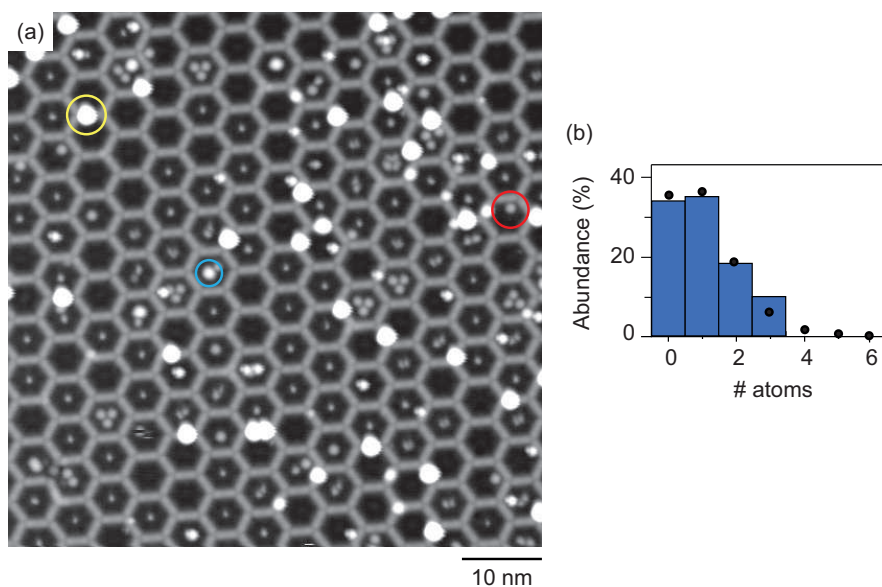


Figure 5.18: Er on NC-Ph₅-CN honeycomb network, $T_{\text{dep}} = 10$ K, $\Theta = 3.5 \times 10^{-3}$ ML. (a) STM image ($V_t = -50$ mV, $I_t = 15$ pA), accompanied by (b) the occupancy histogram, comparing measured values (bars) with calculated binomial distribution (dots).

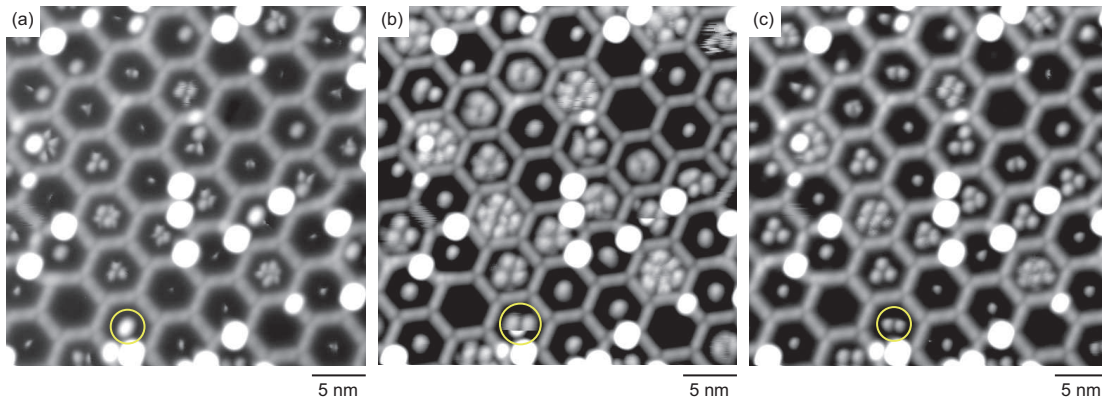


Figure 5.19: Bias dependence of images. Er on NC-Ph₅-CN honeycomb network, $T_{\text{dep}} = 10$ K, $\Theta = 7 \times 10^{-3}$ ML, measured with the following tunneling parameters: (a) $V_t = -500$ mV, $I_t = 20$ pA, (b) $V_t = +500$ mV, $I_t = 20$ pA and (c) $V_t = -100$ mV, $I_t = 20$ pA. The dimer circled in yellow in (a) splits during the scan at positive voltage.

is observed: the atoms are attracted by the tip and when more than one atom is present in the cavity they are imaged as if they occupied multiple positions in the hexagon, giving the impression of a coverage higher than real. Another effect obtained when measuring at positive voltages in this range is that some of the dimers present on the surface split during the scan, as the one circled in yellow. The best measuring conditions are obtained with a moderate negative bias voltage, typically of -50 or -100 mV, as the one used in Fig. 5.19(c).

As for Co atoms, an annealing temperature of 18 K is not sufficient to activate the aggregation of atoms into clusters. Fig. 5.20 shows a sample with a coverage $\Theta = 7 \times 10^{-3}$ ML before [panel

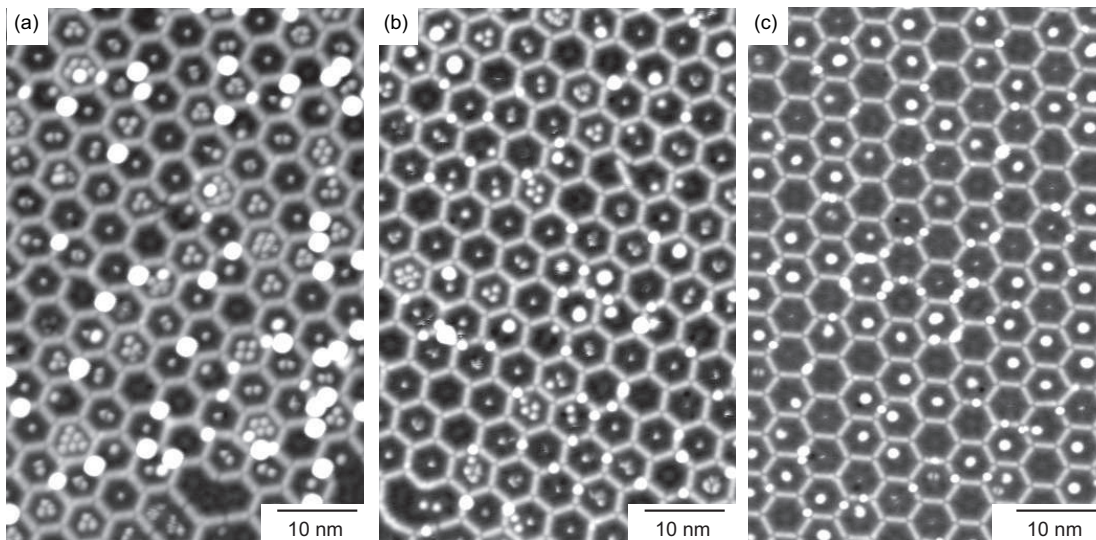


Figure 5.20: Cluster formation. Er on NC-Ph₅-CN honeycomb network, $T_{\text{dep}} = 10$ K, $\Theta = 7 \times 10^{-3}$ ML, (a) after Er deposition, (b) after annealing at 18 K for 1 min and (c) after annealing at 50 K for 1 min ($V_t = -100$ mV, $I_t = 20$ pA).

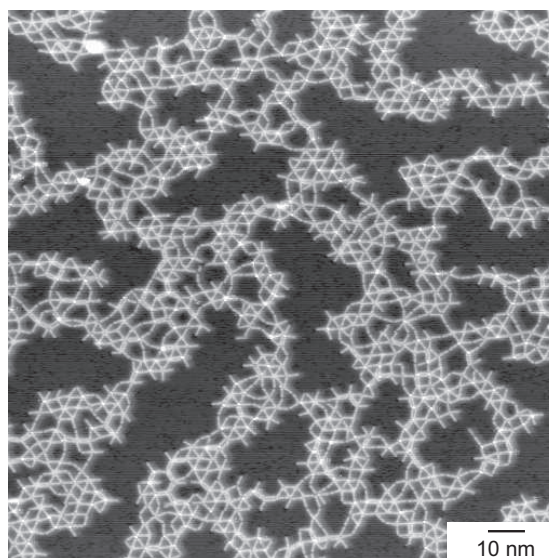


Figure 5.21: Annealing at RT. Er on NC-Ph₅-CN honeycomb network, $T_{\text{dep}} = 10$ K, $\Theta = 7 \times 10^{-3}$ ML after annealing at RT for 2 hours and a half ($V_t = -500$ mV, $I_t = 50$ pA, $T_{\text{meas}} = 50$ K).

(a) and after annealing at 18 K for 1 minute [panel(b)], showing that only in very few cavities clusters are formed. However, this annealing has the effect of providing enough thermal energy to Er atoms on top of molecules to move under the ligands. Annealing for 1 minute at 50 K, on the contrary, leads to the desired results of an array of Er clusters centered in the cavities, Fig. 5.20(c). This shows that the use of the NC-Ph₅-CN honeycomb template for the organization of metal clusters is effective for a relatively wide variety of elements.

Finally, we tested the effect of annealing the sample at room temperature for a long interval of time, two hours and a half, and the result is shown in Fig. 5.21. At such a high temperature the honeycomb network is disrupted and molecules form coordinate bonds with the Er atoms. These nodes have coordination four, five or six: high coordination numbers are common for rare earths [98]. Some nodes with coordination two are probably Cu-coordinated. The assemblies formed by polyphenyl dicarbonitrile molecules in combination with lanthanide centers, namely NC-Ph_{*n*}-CN with Ce or Gd on Ag(111), where recently investigated, and networks with unusual geometries were observed [154, 98].

5.7 Mixed Co-Er clusters on NC-Ph₅-CN template

Co and Er atoms were deposited together on the NC-Ph₅-CN template, with a coverage of 3 and 3.5×10^{-3} ML, respectively. The result is shown in Fig. 5.22(a). The two elements are very easy to recognize, as Er atoms (red circle) have a higher apparent height than Co atoms (blue circle), with values of 130 and 65 pm, respectively. As on the samples with only one kind of atom, a number of atoms are found on top of molecules and some clusters are formed already after the low-temperature deposition. We can observe that in many cavities, for example the one in the yellow circle, are hosted atoms of both kinds. The presence of two different species does not change the tendency of atoms to orderly organize around the center of the

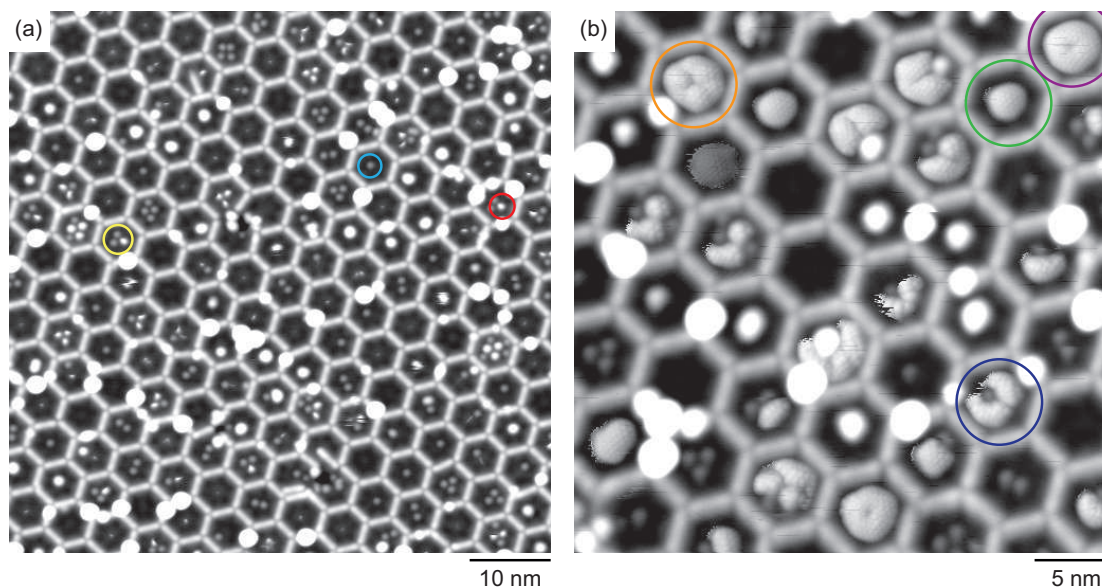


Figure 5.22: Co and Er on NC-Ph₅-CN honeycomb network, $T_{\text{dep}} = 10$ K, $\Theta_{\text{Co}} = 3 \times 10^{-3}$ ML, $\Theta_{\text{Er}} = 3.5 \times 10^{-3}$ ML, (a) overview and (b) closeup. The second image was recorded with a tip that was probably terminated with an impurity giving a special resolution when scanned over Er atoms ($V_t = -50$ mV, $I_t = 20$ pA).

cavities. Figure 5.22(b) shows a closeup view of the system, measured with a functionalized tip, probably terminated with a CO molecule. This special tip is strongly disturbing to the Er atoms, that move around exploring all the most favorable adsorption positions in the cavity, while it leaves unperturbed the Co atoms and the clusters. Notice that through these Er-related features the atomic resolution on the Cu(111) substrate is visible. Based on the analysis of the most likely positions of the atoms in the cavities (cfr Fig. 5.4), we can distinguish cavities occupied by one, two and three Er atoms, indicated respectively with a green, violet and orange circle. In cavities where a cluster or a Co atom is present, the movement of the Er atoms is restricted, blue circle.

Annealing at 50 K for 1 minute has the effect of activating cluster formation, Fig. 5.23, and, as in the other samples, the clusters tend to be centered in the cavities. Since before the annealing most cavities contained a mixture of Co and Er atoms, these clusters are mixed transition metal - rare earth metal clusters. 3D structures where both transition metal and rare earth elements coexist have been synthesized [155, 156], however this is to our knowledge the first time that such mixed clusters are obtained on surfaces, with the additional advantage of being organized in a regular array.

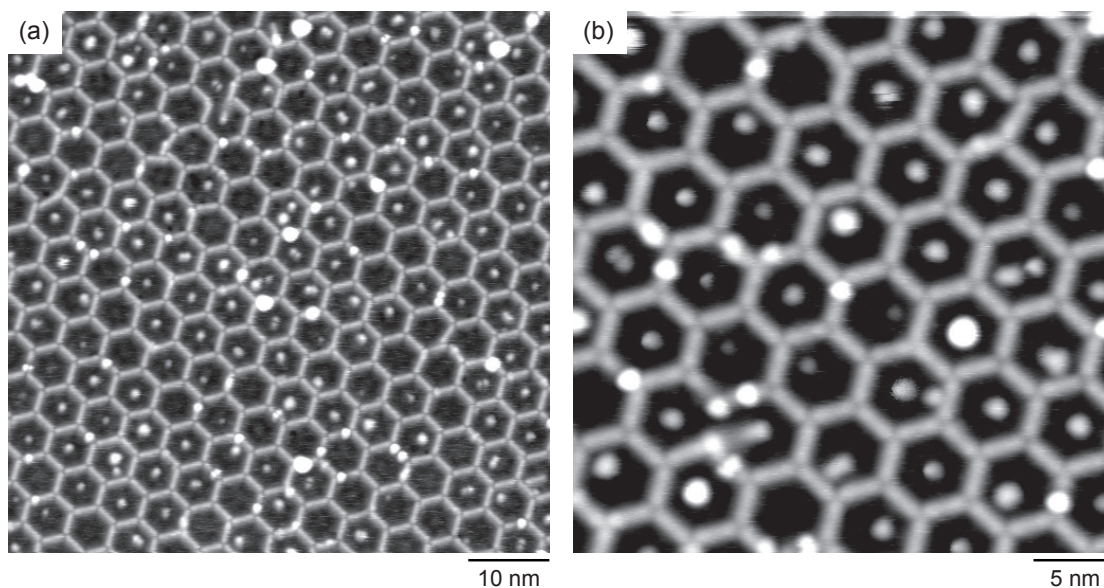


Figure 5.23: Cluster formation. Co and Er on NC-Ph₅-CN honeycomb network after annealing at 50 K for one minute, (a) overview and (b) close-up image. $T_{\text{dep}} = 10$ K, $\Theta_{\text{Co}} = 3 \times 10^{-3}$ ML, $\Theta_{\text{Er}} = 3.5 \times 10^{-3}$ ML ($V_t = -50$ mV, $I_t = 20$ pA).

5.8 Conclusions

In this chapter we demonstrated how the regular networks formed by NC-Ph_{*n*}-CN molecules on Cu(111) can be used as templates for the organization of metal atoms and clusters. The molecules with three phenyl rings are particularly effective for the adsorption of single atoms under the central ring of the molecules. The molecules with five phenyl rings, on the other hand, induce a confinement of the surface state inside the cavities that results in a tendency for atoms to adsorb in the center of the pores. By annealing the sample we can then obtain clusters with a narrow size distribution, nicely organized in a regular array. This is demonstrated both for transition metal elements, Fe and Co, and for a rare earth metal, Er. A regular array of mixed Co-Er clusters is also shown.

Chapter summary

The regular networks formed by NC-Ph₅-CN and NC-Ph₃-CN molecules on Cu(111) can be used to induce the organization of metal atoms and clusters.

On NC-Ph₅-CN networks, upon deposition at 10 K

- Fe atoms are centered in the pores of the honeycomb, truncated triangular, kagome and triangular networks
- Co atoms are centered in the pores of the honeycomb network
- Er atoms are centered in the pores of the honeycomb network
- Fe atoms form clusters upon annealing at 18 K
- Co atoms form clusters upon annealing at 50 K
- Er atoms form clusters upon annealing at 50 K
- Mixed Co-Er clusters are formed upon annealing at 50 K

Thus, regular arrays of clusters of different elements can be obtained.

On NC-Ph₃-CN networks, upon deposition at 18 K, Fe atoms adsorb under the central ring of molecules.



Part III:
Magnetic properties

6 Magnetic properties of Fe atoms and clusters on Cu(111)

6.1 Introduction

Fe atoms adsorbed under the molecules in the NC-Ph_n-CN honeycomb template exhibit very interesting magnetic properties, that will be the subject of Chapter 7. To investigate such properties by means of x-ray absorption and dichroism, we performed reference measurements on Fe atoms adsorbed on the Cu(111) surface. This system proved very interesting in itself, as we observed sharp atomic-like multiplet features, which is unexpected for individual *3d* atoms adsorbed on transition metal surfaces. We determined the spin and orbital magnetic moment and the magnetic anisotropy energy (MAE), for both single atoms and small Fe clusters. We observed a smoothening of the multiplet features and a decrease in the orbital moment with increasing cluster size. Moreover, density functional theory and multiplet calculations revealed an electronic configuration close to *d*⁷.

Fe atoms and clusters adsorbed on Cu(111) have been the subject of a number of studies aiming at the determination of their magnetic properties, both from the theoretical and from the experimental point of view. For example, spin-polarized scanning tunneling microscopy has been used to assemble Fe atoms on Cu(111) to form chains able to perform logical operations [157], or clusters with different geometries to investigate their magnetic properties on an atom-by-atom basis [158]. On top of that, five-atom Fe clusters adsorbed on Cu(111) were reported to exhibit magnetic remanence at $T = 0.3$ K with a relaxation time longer than two hours, and were thus demonstrated to be the smallest stable magnet ever constructed [159]. Single atoms adsorbed on metal surfaces normally experience a strong hybridization, leading to electron delocalization and to a loss of the atomic character of the electronic states. In the case of Fe atoms on Cu(111), however, the issue is controversial. Spin-polarized STM measurements suggest a strong hybridization for this system [160], even if a model that treats five-atom Fe clusters as having half integer spin, thus giving them strong atomic-like features, reproduces correctly the experimental results [159]. It is known that Fe atoms on alkali surfaces exhibit multiplet structures in photoemission spectra, with the degree of atomic-like behavior depending on the chosen substrate [161]. On the other hand, on the surfaces of *5d* and *4d* elements, for example Pt(111) [162, 163], Rh(111) and Pd(111) [164], Fe atoms are known to be strongly hybridized. Cu(111) has an *s*-like density of states at the Fermi energy, bringing it close to alkali surfaces, but at the same time is a *3d* metal, thus it is not trivial to say whether a strong or a weak degree of hybridization is expected. To investigate this issue, we performed a

comprehensive study of the magnetic properties of Fe atoms and clusters on Cu(111). An example of an STM image of Fe atoms deposited on Cu(111) at 10 K and measured at 5 K is shown in Fig. 6.1.

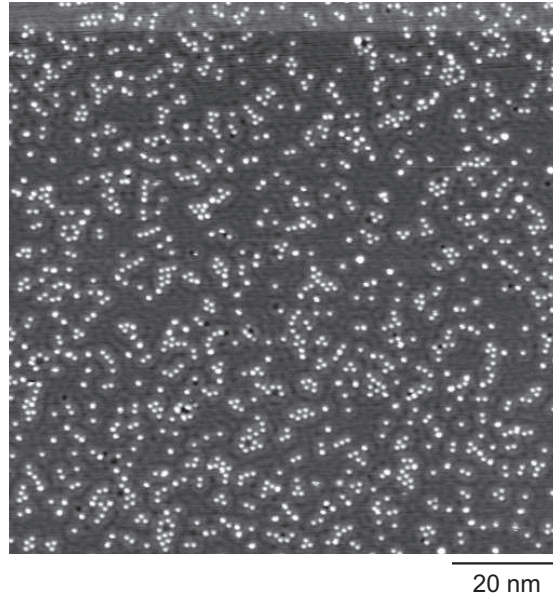


Figure 6.1: STM image of 8×10^{-3} ML of Fe on Cu(111). Fe was deposited at 10 K, the image was measured at 5 K ($V_t = -200$ mV, $I_t = 20$ pA).

Experimental details

The measurements were performed at the EPFL/PSI X-Treme beamline at the Swiss Light Source [54]. We investigated Fe coverages ranging from $\Theta_{\text{Fe}} = 0.007$ ML to 0.145 ML in order to have access to both isolated impurities and small clusters. The Fe coverage was calibrated by correlating XAS and STM data recorded with the microscope mounted on the end station, and the deposition rate was set to 0.007 ML/min.

Measurements were taken at the $L_{2,3}$ absorption edges of Fe, resulting from the excitation of $2p$ core electrons into empty $3d$ states. We investigated both the out-of-plane and in-plane XAS and XMCD signals by rotating the sample from $\theta = 0^\circ$ to $\theta = 60^\circ$ between sample normal and x-ray beam. We recorded element specific magnetization curves as the ratio between the amplitude of the L_3 XMCD intensity at the peak and the intensity at the pre-edge, at both normal and grazing incidence. All measurements were performed at $T = 2.5$ K and in magnetic fields up to $B = \pm 6.8$ T parallel to the x-ray beam.

6.2 Fe monomers on Cu(111)

Figure 6.2 shows XAS and XMCD spectra measured for normal and grazing incidence on a sample with coverage $\Theta_{\text{Fe}} = 0.007$ ML. Multiplet structures, which are not observed in the bulk spectra [166], can be clearly seen for both angles of incidence. In the XAS a splitting of the L_2 peak is observed, both for μ_+ and μ_- , and the L_2 peak in the XMCD spectra, which is

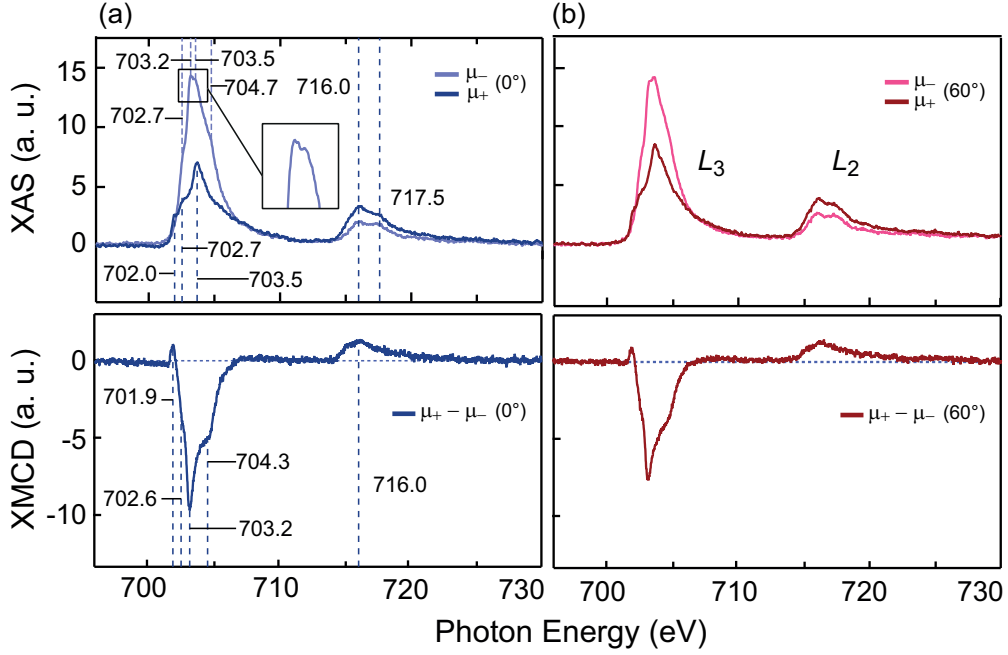


Figure 6.2: XAS and XMCD spectra for Fe monomers on Cu(111) for (a) normal incidence and (b) grazing incidence. Spectra are measured at the Fe $L_{2,3}$ absorption edges, with $T = 2.5$ K and $B = 6.8$ T collinear with the x-ray beam. Spectra are taken with parallel (μ_+) and antiparallel (μ_-) alignment of light helicity with respect to the magnetic field. XMCD spectra have been normalized to the Fe coverage determined by the integral of the $\mu_+ + \mu_-$ spectrum over the $L_{2,3}$ edges. The inset magnifies the L_3 peak of the μ_- component of the XAS; $\Theta_{\text{Fe}} = 0.007$ ML. Adapted with permission from our paper, Ref. [165].

found at 716.0 eV, originates from the lower energy component of this XAS peak. Also on the L_3 peak the μ_- component is split, as seen in the inset, and also in this case the corresponding XMCD peak, measured at 703.2 eV, comes from the lower energy component of the XAS feature. Moreover, multiple shoulders are present on the sides of the L_3 peak both in the XAS and in the XMCD spectra (see the labeled energies on the figure), and in the XMCD a small positive feature at the onset of the L_3 peak is observed.

These features are similar to those measured for Fe atoms on alkali metal [167, 161], or thin oxide films [168], suggesting an electronic configuration close to $3d^7$. Our spectra have more atomic-like features than the ones reported for Fe/Cu(100) [169, 162], as expected if one considers the reduced number of nearest-neighbors on Cu(111) with respect to Cu(100), and coherently with the higher orbital magnetic moment that is predicted by DFT for Fe on Cu(111) ($\mu_L = 0.65 \mu_B$) with respect to Fe on Cu(100) ($\mu_L = 0.47 \mu_B$) [170].

To determine the electronic configuration of the Fe atoms on Cu(111) multiplet calculations were performed¹ using the CTM4XAS55 code [171]. To a first approximation a $C_{\infty,v}$ sym-

¹ Configuration interaction is allowed respecting the $C_{\infty,v}$ symmetry, therefore the hopping integrals $t(a_1) = 0.3$ eV, $t(e_1) = 1.0$ eV and $t(e_2) = 1.0$ eV were used. The charge transfer energy Δ and the core-hole interaction $U_{p-d} - U_{d-d}$ were set respectively to -10.0 eV and 1.0 eV. Default values were used for the Slater-Condon integrals, corresponding to a reduction to 80% of the Hartree-Fock values. Transition amplitudes for L_2 and L_3 were

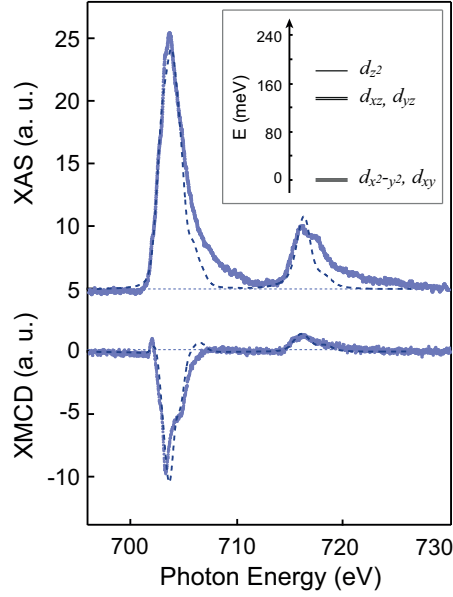


Figure 6.3: Simulated XAS and XMCD spectra (dashed lines) compared with experimental ones for normal incidence on individual Fe atoms on Cu(111), $\Theta_{\text{Fe}} = 0.007$ ML. The inset shows the energy splitting of the singlet and doublet states resulting from the $3d$ orbitals as given by multiplet calculations. XAS and XMCD spectra are best reproduced using a 3 % $3d^6$ and 97 % $3d^7$ configuration. Adapted with permission from our paper, Ref. [165].

metry was assumed for the crystal field felt by the atom. This symmetry is generated by the sea of s -like conduction electrons of the substrate, which creates a vertically homogeneous electrostatic repulsion, while the d -states, that are well below E_{F} , do not contribute. This uniaxial crystal field lifts the degeneracy of the d -orbitals, producing an a_1 singlet (d_{z^2}) and two doublets e_1 (d_{xz}, d_{yz}) and e_2 ($d_{x^2-y^2}, d_{xy}$). Best fits, obtained by optimizing the multiplet calculation parameters to describe the XAS and XMCD spectra measured at normal incidence, are shown in Fig. 6.3. We find that the ground state is well described using a mixed electronic configuration that consists of 3 % $3d^6$ and 97 % $3d^7$, which corresponds to a number of holes $h_d = 3.03$. The calculated splitting of the $3d$ orbitals is shown in the inset of Fig. 6.3: the $d_{x^2-y^2}, d_{xy}$ doublet is lowest in energy, followed by the d_{xz}, d_{yz} doublet (135 meV) and finally by the d_{z^2} singlet (180 meV).

With the number of holes found in the multiplet calculations, orbital and spin magnetic moments can be obtained from the measured spectra using the sum rules [51, 52]. We obtain $\mu_L = 0.66 \pm 0.04 \mu_{\text{B}}$ and $\mu_{S+7T} = 2.18 \pm 0.05 \mu_{\text{B}}$ at normal incidence, and $\mu_L = 0.42 \pm 0.04 \mu_{\text{B}}$ and $\mu_{S+7T} = 1.80 \pm 0.04 \mu_{\text{B}}$ at grazing incidence. As the sum rule gives the spin moment together with the spin dipole moment, it is not possible to determine the two contributions individually, also because saturation is not reached at grazing incidence [172]. We also note that the L_2 and L_3 edges are not perfectly separated, which can lead to an underestimation of the spin

calculated in a dipolar approximation and broadened with Lorentzian functions of FWHM = 0.45 and 0.15 eV, respectively, to reproduce the experimental data. A further gaussian broadening of 0.35 eV was introduced to include the finite experimental energy resolution.

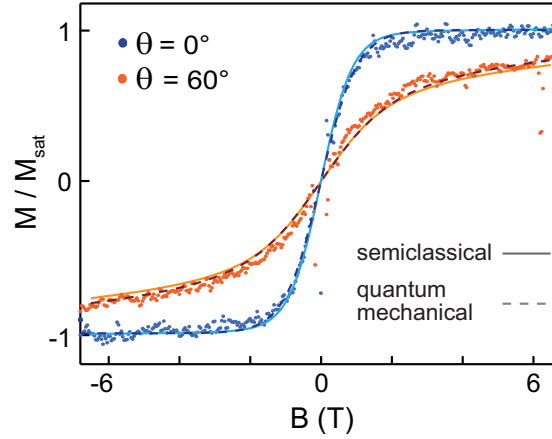


Figure 6.4: Magnetization curves for normal (blue) and grazing (orange) incidence. The experimental dots represent the amplitude of the L_3 XMDC peak at 703.2 eV divided by the pre-edge intensity at 701.2 eV. The curve measured at grazing incidence is multiplied by the ratio $(\mu_L + \mu_{S+7T})_{grazing}/(\mu_L + \mu_{S+7T})_{normal}$. Solid lines represent the fit obtained with the semiclassical model, dashed lines the one obtained with the quantum mechanical model; $\Theta_{Fe} = 0.011$ ML. Adapted with permission from our paper, Ref. [165].

moment [173].

We note that at normal incidence the ratio μ_L/μ_{S+7D} is 0.30, more than twice the value of 0.12 that is obtained for Fe/Pd(111), and twice that of Fe/Rh(111) (0.15) [164], which confirms the reduced hybridization of the present system.

The fact that the intensity of the L_3 XMCD peak is higher in normal compared to grazing incidence implies an out-of-plane easy axis. This is confirmed by the fact that the magnetization curve, which is shown in Fig. 6.4, is steeper for $\theta = 0^\circ$ than for $\theta = 60^\circ$ around 0 T.

Since the system has a behavior in between a classical and a quantum one, we used two different approaches to simulate the magnetization curves, in order to obtain the average MAE per atom K and the total magnetic moment μ . Within a semiclassical model the magnetization curve can be fit using the formula [174]:

$$M = M_{sat} \frac{\int_0^{2\pi} d\phi \int_0^\pi d\theta \sin\theta \cos\theta e^{-E(\theta_0, \theta, \phi)/k_B T}}{\int_0^{2\pi} d\phi \int_0^\pi d\theta \sin\theta e^{-E(\theta_0, \theta, \phi)/k_B T}} \quad (6.1)$$

where

$$E(\theta_0, \theta, \phi) = -\mu B \cos\theta - K(\sin\theta_0 \sin\theta \cos\phi + \cos\theta_0 \cos\theta)^2 \quad (6.2)$$

with θ_0 the easy magnetization direction and \mathbf{B} taken as z -axis.

With this analysis we find a MAE per atom of $K = 1.8 \pm 0.4$ meV and a total magnetic moment per atom of $\mu = 4.5 \pm 0.5 \mu_B$, where $\mu = \mu_L + \mu_S + \mu_{ind}(\text{Cu})$ includes the magnetic moment that is induced on the Cu sites per Fe atom. The calculated curves are shown in Fig. 6.4 and show a very good agreement with the experimental ones.

On the other hand, in a quantum mechanical approach we can describe the spin states of an Fe atom using the following spin hamiltonian:

$$\hat{H}_{spin} = g\mu_B \hat{\mathbf{S}} \cdot \mathbf{B} + D\hat{S}_z^2 \quad (6.3)$$

where g is the electron Landé factor, \mathbf{B} is the external magnetic field, D the uniaxial anisotropy parameter, and $\hat{\mathbf{S}}$ the effective spin operator. The z -axis is chosen by convention in order to maximize $|D|$. Following the electronic configuration suggested by the multiplet calculations, we modeled our system using an effective spin $S = 3/2$, implying a half-integer ground and first excited state doublets. The expectation values of the magnetization along the beam axis as a function of \mathbf{B} are calculated as:

$$\langle M_{\theta_0} \rangle = g \langle S_{\theta_0} \rangle = g \frac{\sum_{i=1}^{2S+1} \langle \phi_i | S_{\theta_0} | \phi_i \rangle e^{\epsilon_i / k_B T}}{\sum_{i=1}^{2S+1} e^{\epsilon_i / k_B T}} \quad (6.4)$$

where $S_{\theta_0} = \sin\theta_0 S_x + \sin\theta_0 S_y + \cos\theta_0 S_z$ is the spin operator for an arbitrary incidence angle θ_0 , while ϕ_i and ϵ_i are the eigenstates and eigenvalues obtained after diagonalizing the spin hamiltonian. The parameters g and D were adjusted to fit the experimental data. The obtained curves for both incident angles are shown as dashed lines in Fig. 6.4. They practically coincide with the classical curves and show a very good agreement with experiment. We find $g = 2.45 \pm 0.3$ and $D = -0.85 \pm 0.2$ meV, so, having assumed a spin $S = 3/2$, we obtain a total magnetic moment $\mu = g\mu_B S = 3.7 \pm 0.5 \mu_B$ and a magnetic anisotropy $K = -2D = 1.7 \pm 0.4$ meV. The values for K in the two models agree within the error bars, while the total moment calculated in the quantum mechanical framework is lower than in the semiclassical one.

Multiplet calculations give a good description of atomic systems with localized electrons. However, since our system involves delocalized electrons, we can not exclusively rely on them. In order to address the electronic and magnetic properties of the system with a complementary theoretical method, we asked Dr. Gabriel Autès and Prof. Oleg Yazyev (Institute of theoretical Physics, EPFL) to perform non-relativistic DFT calculations for a single Fe atom located on a 5 layer thick slab of Cu(111) within a (4×4) supercell (see the inset in Fig. 6.5). The generalized gradient approximation was used with a mean-field Hubbard correction (GGA + U) [175], as implemented in the QUANTUM ESPRESSO code [176]. Using the linear response approach, the value of the Hubbard U was estimated to be 2.9 eV [177]. Different values of U , namely $U = 2.2$ eV and $U = 4$ eV, give very similar results. To find the adsorption position of the Fe atom, the structure was fully relaxed starting from the four high symmetry positions (hcp, fcc, top, and bridge). The lowest energy configuration corresponds to the Fe atom located on the fcc adsorption site, at a distance of 1.96 Å above the atomic plane of Cu. The atomic spin and the electronic configuration of the Fe were obtained by projecting the wave functions of the entire system on the Fe atomic orbitals. The Löwdin population and the spin polarization of the 4s and 3d atomic orbitals of Fe are given in Tab. 6.1, while the corresponding spin-resolved local density of states plots are shown in Fig. 6.5.

These results show that the Fe adatom is close to a $4s^1 3d^7$ configuration, which corresponds to $h_d = 3.15$. This value is in good agreement with the one obtained from the multiplet

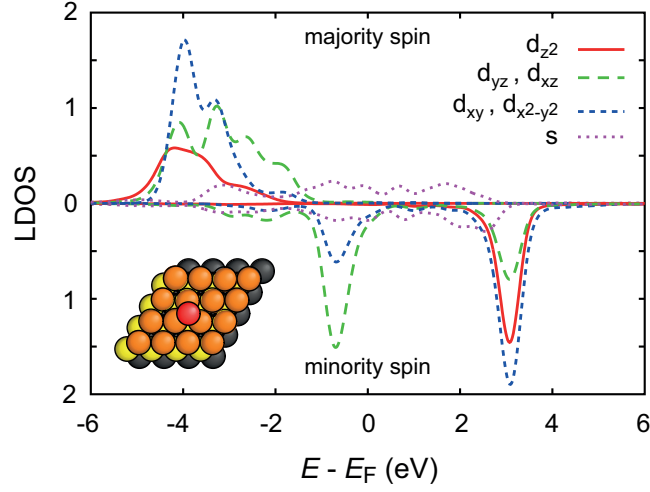


Figure 6.5: Spin-resolved local density of states projected on the Fe atomic orbitals. The inset shows the geometry of the slab used for DFT calculations. Adapted with permission from our paper, Ref. [165].

calculations. We can see that Fe acts as a donor of $\approx 0.1 e^-$, which is transferred to Cu. The spin polarization of the $3d$ states ($3.08 \mu_B$) shows that the Fe atom is in a $S = 3/2$ spin configuration, as was assumed in the quantum mechanical model.

To estimate the orbital moment and the MAE, a relativistic calculation was performed on a smaller 3-layer-thick 4×4 slab of Cu(111) with a single Fe atom located in the lowest energy relaxed position. Spin-orbit effects were accounted for using fully relativistic pseudopotentials acting on valence electron wavefunctions represented in the two-component spinor form [178]. The orbital moment was estimated by computing the expectation value of the orbital moment operator for the projection of the Khon-Sham wavefunctions on the $3d$ orbitals of Fe. For the out-of-plane spin polarization, an orbital moment $\mu_L = 0.175 \mu_B$ is obtained, smaller than the one found with the sum rules, while the spin moment is $\mu_S = 3.16 \mu_B$, in good agreement with the non relativistic result of $3.24 \mu_B$. The spin moment cannot be compared directly to the experimental one, because the latter includes μ_{7T} . The low MAE obtained in these calculations is beyond the level of convergence that could be achieved with respect to k -point sampling on a (3×3) mesh.

The reduced value of the calculated orbital moment compared to the experimental one is a

Table 6.1: Löwdin populations and spin polarization of the Fe orbitals as obtained from the non-relativistic DFT calculations.

	Total	4s	3d
total charge	7.89	1.04	6.85
spin up	5.57	0.60	4.97
spin down	2.33	0.44	1.88
polarization	3.24	0.16	3.08

well known limitation of DFT calculations considering structural relaxation. On the contrary, calculations that are based on idealized bulk-like distances minimize the adatom-support hybridization, giving larger orbital moment and MAE at the expense of an unrealistic geometry and electronic structure, as extensively discussed in Ref. [164]. For example, Lazarovits *et al.* [170] find $\mu_L = 0.65 \mu_B$ and $K = 4.3$ meV, considering for the Fe atom a bulk-like distance from the surface of 2.11 Å, about 10% larger than the value found in our calculations of 1.96 Å. Their value for $\mu_S = 3.27 \mu_B$, on the other hand, is in good agreement with ours, as are the $3.24 \mu_B$ found by Mavropoulos *et al.* [179] and the $3.17 \mu_B$ reported by Stepanyuk *et al.* [180]. All the calculated spin moments are larger than the value we find with the application of the sum rules. The total magnetic moment we deduce by fitting the magnetization curves is close to the $\mu = 3.5 \mu_B$ reported for Fe monomers on Cu(111) by Khajetoorians *et al.* [160]. In the same work they also report a value for the anisotropy energy K comprised between 0.8 and 1.5 meV, similar to the values we determine from our analysis. The experimental values for K are not surprising, since also on other substrates, such as Ag(111) [181], Pt(111) [162, 163], Pd(111) and Rh(111) [164], Fe atoms have an out-of-plane anisotropy and a small value for the MAE, of the order of at most 2 meV.

6.3 Small Fe clusters on Cu(111)

We investigated the evolution of the spectral features and of the magnetic moments upon formation of small Fe clusters by increasing the Fe coverage up to $\Theta = 0.145$ ML. The XAS and XMCD spectra are shown in Fig. 6.6, with coverage increasing from top to bottom. The spectra evolve towards those of bulk Fe, with a gradual smoothening of the shoulders that decorate the XAS and XMCD peaks, along with the disappearance of the small peak at the onset of the XMCD L_3 main peak. The disappearance of the low-energy component of the μ_- XAS L_3 peak results in a shift toward higher energies of the corresponding XMCD peak, up to a final value of 703.6 eV. In a similar way, the evolution of the XAS L_2 double peak into a single feature results in an upward shift of the corresponding XMCD resonance, that is located at 716.9 eV for the sample with highest coverage. The smoothening of the multiplet structure with increasing coverage resembles what was observed for Co atoms and clusters on K films [167] and on Pt(111) [174]. It is a consequence of the broadening of the adatom density of states, owing to d -state hybridization with the surrounding atoms in the cluster.

To correlate the observed spectral changes with the cluster sizes at the respective coverages Kinetic Monte Carlo (KMC) simulations [129] were performed. The diffusion of Fe on Cu(111) was studied in the past: the diffusion barriers reported from DFT calculations are $E_m = 25$ meV [148], 22 meV [138] and 28 meV [146], and the barriers and attempt frequencies measured from temperature dependent adatom diffusion rates are $E_m = 22$ meV and $\nu_0 = 1 \times 10^{10}$ Hz [146], and $E_m = 23.8$ meV and $\nu_0 = 4 \times 10^8$ Hz [147]. $E_m = 25$ meV and a universal pre-exponential factor of $\nu_0 = 10^{12}$ Hz were chosen for our simulations. From this, we find in agreement with experiment that the terrace diffusion of isolated Fe atoms is frozen at our $T_{\text{dep}} = 3.5$ K and that the diffusion rate is 30 Hz at 12 K - in line with the fact that, as we saw in Chapter 5, at this temperature Fe atoms organize in the cavities of porous metal-organic templates. The formation of dimers has been reported to happen for Fe/Cu(111) by deposition

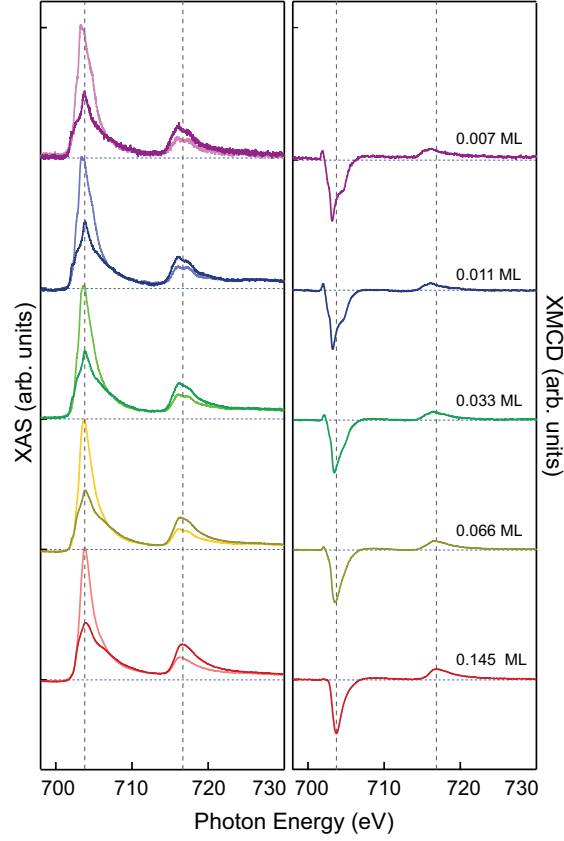


Figure 6.6: XAS (left) and XMCD (right) spectra at the Fe $L_{2,3}$ absorption edges for the Fe coverages indicated next to each curve. $T = 2.5$ K, $B = 6.8$ T and $\theta = 0^\circ$. All XAS are normalized to one and vertically offset. Adapted with permission from our paper, Ref. [165].

of atoms close to other adatoms ($r \leq 0.6$ nm) and not by the lateral approach of adatoms that are further away [182]. In our simulations, we enable easy attachment of one Fe atom to a neighboring Fe atom or cluster if it is two atomic distances apart [129]. The barrier for this process is chosen such that it always happens ($E_{\text{att}} = 0.1$ meV). The time intercurring between the deposition and the end of measurements does not alter the size distributions, since regular terrace diffusion does not take place and all easy attachment processes have happened immediately during deposition.

Figure 6.7 shows the orbital and spin magnetic moments as a function of coverage and of the respective mean cluster size found in KMC simulations; the corresponding values are reported in Tab. 6.2 together with the branching ratios. Figure 6.8 shows the contributions of the different cluster sizes to the XAS intensity for four Fe coverages, obtained by multiplying the relative abundance of each cluster size by the number of atoms contained in the cluster.

In the spectra of Fig. 6.6, some multiplet-related features are observed for coverages up to 0.066 ML. By comparison with Fig. 6.8, we deduce that the multiplet structure disappears when the contribution of monomers to the overall XAS signal becomes negligible. We conclude that only monomers have a remainder of the atomic-like spectrum, while already

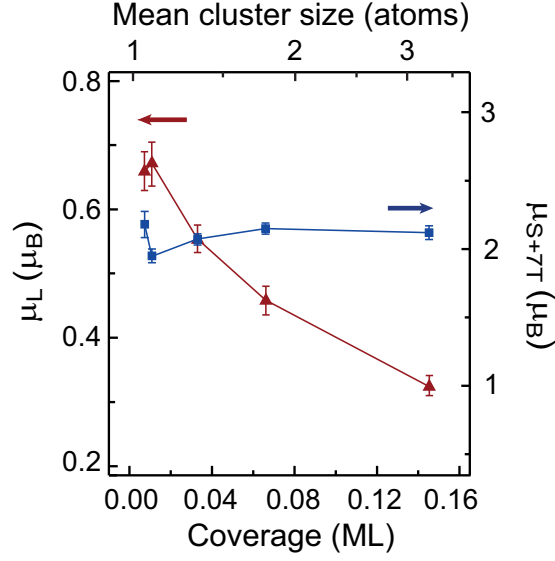


Figure 6.7: Orbital magnetic moments, triangles, and spin magnetic moments, squares, measured at normal incidence as a function of coverage (bottom) and mean cluster size (top). We assumed the single atom value for the number of holes $h_d = 3.03$, as given by multiplet calculations, independently of cluster size. Adapted with permission from our paper, Ref. [165].

dimers have a spectrum close to the bulk one. We note that while the spin moment is size-independent, the orbital moment rapidly decreases with increasing mean size, similar to the case of Co/Pt(111) [174]. The ratio of L_3 to L_2 x-ray absorption intensities (branching ratio) starts to decrease once the monomers are not the dominant species any more. The overall values are quite high since the statistical ratio of $L_3:L_2$ is 2:1, and crystal field and spin-orbit interaction normally cause a reduction. However, large branching ratios were observed for small Fe clusters in gas phase and attributed to size-dependent core-hole screening [184, 185].

Table 6.2: Coverage dependent out-of-plane spin and orbital magnetic moments, $L_{2,3}$ branching ratios ($I(L_3)/I(L_2)$), and mean cluster size $\langle s \rangle$ as calculated by KMC. The spin and orbital magnetic moments for 1 ML of Fe on Cu(111) and for bulk Fe are shown for comparison. We assumed $h_d = 3.03$, independently of cluster size, while $h_d = 3.4$ has been taken for the ML and bulk cases.

Coverage (ML)	μ_{S+7D} (μ_B)	μ_L (μ_B)	L_3/L_2	$\langle s \rangle$
0.007	2.18 ± 0.10	0.66 ± 0.04	4.2	1.07
0.011	1.95 ± 0.05	0.67 ± 0.05	4.4	1.12
0.033	2.07 ± 0.04	0.55 ± 0.03	4.3	1.37
0.066	2.15 ± 0.04	0.45 ± 0.03	3.9	1.82
0.145	2.12 ± 0.05	0.32 ± 0.02	3.3	3.25
1 [183]	0.70 ± 0.20	0.045 ± 0.015	-	-
bulk [166]	1.97	0.068	2.2	-

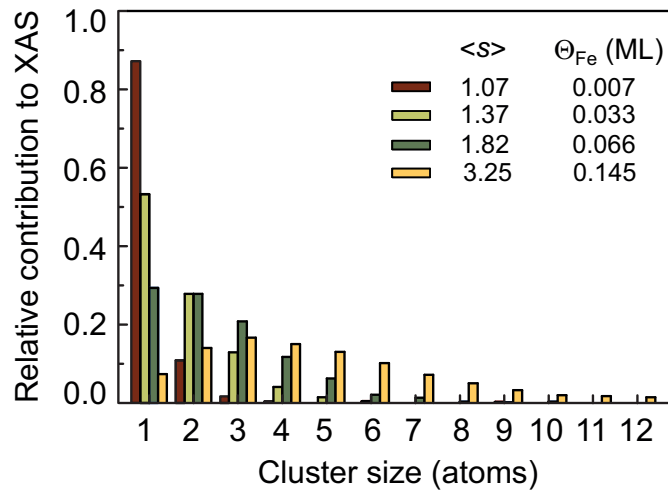


Figure 6.8: Cluster size distributions as determined from KMC simulations, multiplied by the respective size to yield the contribution of each cluster size to the overall XAS intensity for the four displayed coverages. Adapted with permission from our paper, Ref. [165].

6.4 Conclusions

Our XAS and XMCD measurements show that Fe atoms adsorbed on Cu(111) exhibit multiplet features, that gradually disappear with increasing coverage and mean cluster size. We measure the spin, orbital and total magnetic moment, as well as the magnetic anisotropy energy, for single Fe atoms adsorbed on Cu(111), and compare the obtained values with the ones predicted by DFT. We find that the ground state of the Fe atoms is close to a $4s^1 3d^7$ configuration, and that the hybridization with the Cu substrate is low. We also demonstrate how the formation of small clusters influences the evolution of the orbital magnetic moment and of the branching ratio, while the spin magnetic moment is, at the small sizes considered and within our resolution, insensitive to cluster size.

Chapter summary

We studied the magnetic properties of Fe atoms and clusters on Cu(111) by means of XAS, XMCD, multiplet calculations and DFT

- Fe atoms/Cu(111) have atomic-like multiplet features and an out-of-plane magnetic anisotropy energy
- such features disappear upon cluster formation
- the orbital magnetic moment decreases upon cluster formation, while the spin moment is unaffected
- the ground state electronic configuration of Fe atoms/Cu(111) is close to $4s^1 3d^7$

7 Two-orbital Kondo effect on metal-organic complexes

7.1 Introduction

The interaction between a magnetic impurity and the conduction electrons of a non-magnetic host can give rise to a many body singlet state and to the appearance of a resonance near the Fermi energy (E_F). This process, known as Kondo effect [186], has been deeply investigated in bulk solids, but also in various low-dimensional systems, such as surface adsorbed atoms [187, 188, 189], semiconductor quantum dots [190, 191], and carbon nanotubes [192]. In recent years, great attention was devoted also to organic and metal-organic molecules, thanks to the possibility of manipulating their electronic and magnetic properties and their potential in single-molecule spintronic applications [193, 194]. A very interesting aspect is that, to a certain extent, the Kondo effect in metal-organic systems can be manipulated in a controlled way: it can be turned on and off by adsorbing atoms or small molecules [195, 196, 197], by detaching peripheral hydrogen atoms [198], by charge transfer from other molecules [199] or by modifying the molecular conformation with voltage pulses [200, 201], a procedure that can also change the Kondo temperature, T_K [202], which determines the energy scale of the screening. The study of more complex Kondo systems, for example the case where there is more than one screening channel available, can give new insight into their properties, possibly leading to new tools for the control of magnetism and spintronics at the nanoscale. To date, molecular systems where more than one orbital can contribute to Kondo screening have rarely been investigated. Underscreened Kondo systems, where only one of the available channels is active, were reported [203, 204]. For metal-organic molecules on superconducting substrates, the screening of two Kondo channels was observed above the critical temperature [205].

In this chapter we will discuss how the combination of transition metal atoms and dicyanobenzene poliphenyl molecules can, depending on the chosen element, suppress or induce a Kondo effect. In particular, we will investigate a strongly anisotropic Kondo effect which arises when Fe atoms are adsorbed under NC-Ph_n-CN molecules. Owing to the presence of two singly occupied orbitals acting as Kondo channels, this system exhibits two distinct Kondo temperatures and line shapes, as observed in STS. DFT calculations demonstrate that these Fe-related *d* orbitals have different spatial distributions across the system and a different hybridization with the molecular orbitals. XMCD reveals that the spin in both Kondo channels is fully screened. We therefore have a multichannel Kondo system, where two channels with distinctive spatial distributions are active.

7.2 STS measurements

As discussed in Chapter 5, after deposition of Fe and Co atoms on the NC-Ph₃-CN honeycomb network at 10 K three species are observed on the sample: atoms adsorbed on the Cu(111) substrate, atoms on top of molecules and atoms below molecules. For the case of Fe this is illustrated in Fig. 7.1(a), with an Fe adatom on the substrate circled in turquoise, one on top of a molecule in yellow, and one below a molecule in red. In Fig. 7.1(b) a sample prepared in order to have approximately one Fe atom under each molecule is shown, obtained by depositing 18×10^{-3} ML of Fe at $T_{\text{dep}}=50$ K.

The electronic structure of Fe and Co atoms adsorbed on the substrate, on top and under the molecules has been characterized by means of STS.

A Kondo resonance measured by STS can be described by a Fano function [206],

$$\Phi(E) = \frac{(q\Gamma + E - E_0)^2}{\Gamma^2 + (E - E_0)^2} \quad (7.1)$$

with E_0 the energy position of the resonance and Γ its half-width at half-maximum; q determines the shape of the curve and expresses the ratio between direct tunneling into the impurity state and tunneling into the continuum. Γ has a characteristic dependence on temperature expressed by $2\Gamma = [(\alpha k_B T)^2 + (2\Gamma_0)^2]^{1/2}$ [207, 208], with Γ_0 the half-width at 0 K, related to the Kondo temperature by $\Gamma_0 = k_B T_K$.

Undecorated molecules and Fe and Co atoms adsorbed on top of molecules show no noteworthy spectral features around E_F , Fig. 7.2(a).

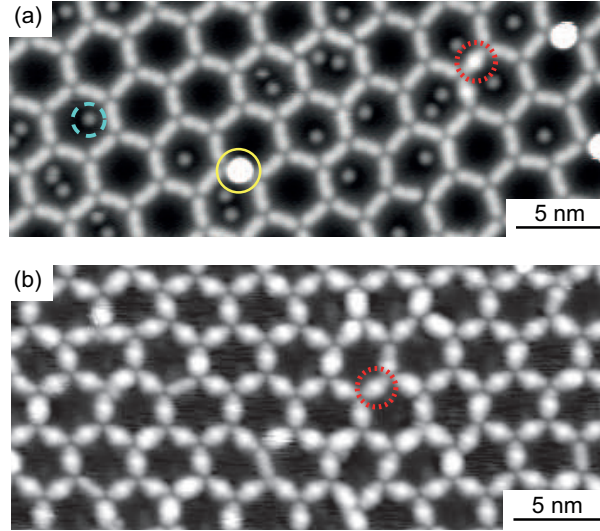


Figure 7.1: Fe deposition on the NC-Ph₃-CN honeycomb network. (a) The NC-Ph₃-CN honeycomb network after evaporation of $\Theta = 6 \times 10^{-3}$ ML of Fe at $T_{\text{dep}} = 10 \pm 2$ K ($V_t = -200$ mV, $I_t = 100$ pA). Dashed turquoise circle: Fe atom on Cu(111); solid yellow circle: Fe atom on-top of molecule; dotted red circle: Fe atom below molecule. (b) Deposition of $\Theta = 18 \times 10^{-3}$ ML of Fe at $T_{\text{dep}} = 50 \pm 2$ K ($V_t = -500$ mV, $I_t = 100$ pA).

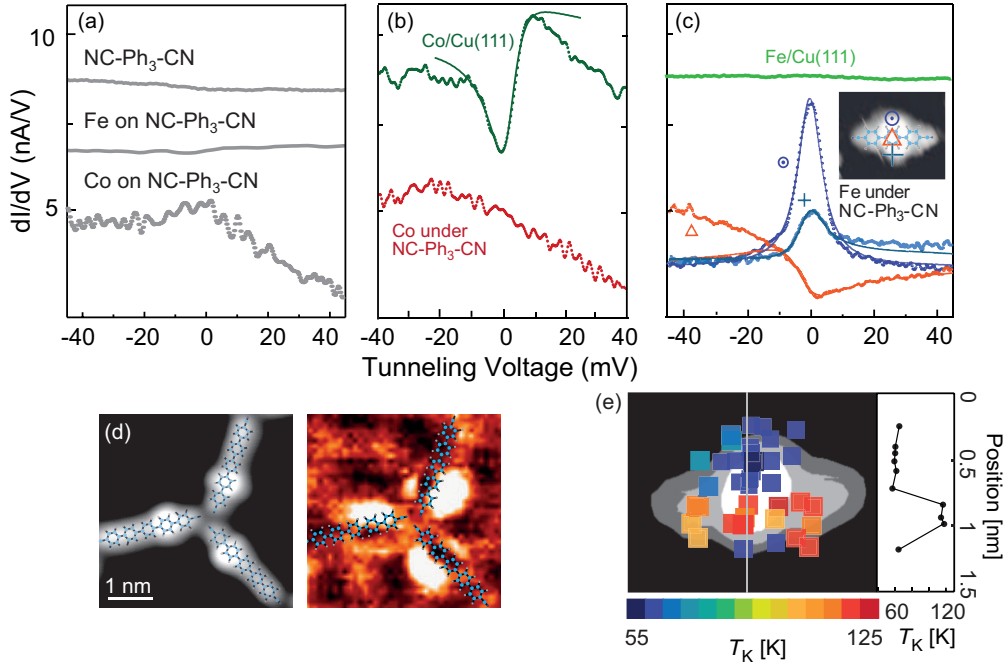


Figure 7.2: STS on metal-organic complexes. (a) Spectra acquired on the indicated systems, offset for clarity. Setpoint: $V_t = -50$ mV, $I_t = 300$ pA, $V_{\text{mod}} = 2$ mV at 523 Hz. (b) dI/dV spectra acquired on a Co atom on Cu(111) (green) and under a molecule (red). Green solid line: fit by Eq. (7.1). Setpoint: $V_t = -50$ mV, $I_t = 50$ pA, $V_{\text{mod}} = 2$ mV at 523 Hz. (c) dI/dV spectra acquired on an Fe atom on Cu(111) (green) and on an Fe atom buried by NC-Ph₃-CN at the locations shown in the inset. Solid lines are fits by Eq. (7.1): (\odot) $\Gamma_0 = 5.4 \pm 0.3$ meV, $q = 10$; (+) $\Gamma_0 = 5.3 \pm 0.2$ meV, $q = 3$; (Δ) $\Gamma_0 = 9.8 \pm 0.5$ meV, $q = -0.6$. $\alpha = 5$. Setpoint: $V_t = -50$ mV, $I_t = 300$ pA, $V_{\text{mod}} = 2$ mV at 523 Hz. (d) Topography and dI/dV map at E_F showing three NC-Ph₅-CN molecules, each with an Fe atom below the second phenyl ring. Overlay: Molecular structure. (e) T_K map recorded on a NC-Ph₃-CN molecule burying an Fe atom. Right: variation of T_K along a cut perpendicular to the molecular axis (grey line).

Co is known to exhibit a Kondo resonance on Cu(111) [188, 134], and our STS measurements, shown in Fig. 7.2(b), reproduce well the reported Fano dip. Fit with Eq. 7.1 yields $\Gamma_0 = 4.5 \pm 0.3$ meV, $q = 0.4$ and $T_K = 52 \pm 3$ K. However, this Kondo signature disappears when Co atoms are under the molecules, Fig. 7.2(b), or, as we said, on top of them, Fig. 7.2(a). The disappearance of the Kondo effect upon formation of metal organic complexes was reported also for the case of Co bound to TCNE molecules on Cu₂N [209].

The case of Fe is quite different. The differential conductance spectrum acquired on an Fe atom adsorbed on Cu(111), Fig. 7.2(c), is flat around E_F . On the contrary, spectra acquired on molecules covering an Fe atom show rather large variations of the differential conductance close to E_F , with a marked spatial dependence of the spectral features across the molecule, Fig. 7.2(c). The conductance exhibits an intense peak on one side (\odot), followed by a dip above the molecule (Δ), and finally on the other side of the molecule by a peak with reduced conductance change (+). These spectral features are very similar for both NC-Ph₃-CN and

NC-Ph₅-CN molecules. We interpret them as a manifestation of Kondo screening.

The fit with Eq. (7.1) [solid lines in Fig. 7.2(c)] agrees very well with experiment in the relevant energy interval around E_F . The peaks on both sides of the molecule yield consistent Kondo temperatures of $T_K = 63 \pm 4$ K and 62 ± 3 K, while the dip gives a significantly higher value of $T_K = 114 \pm 5$ K.

We can conclude that Fe is Kondo-screened only when under the molecules, while Co is Kondo-screened only as adatom.

The spatial distribution of the two types of resonances observed for Fe atoms buried by NC-Ph_{*n*}-CN molecules can be seen in the differential conductance map shown together with the constant current image in Fig. 7.2(d). The images show three NC-Ph₅-CN molecules bound to the central Cu atom, each with an Fe atom below the second phenyl ring. The brightest and largest spots in the dI/dV image correspond to the main peak and are located at one side of the ligands. The dips appear as depressions in the map and extend along the molecular axis, while the peaks with smaller amplitude appear as less bright and smaller features on the respective other side of the molecule. The higher intensity observed on one side of the molecule is ascribed to the tilt of the phenyl rings with respect to the surface plane and with respect to each other, as discussed in Chapter 2.

The spatial distribution of the Kondo temperature is shown in Fig. 7.2(e). The map was derived by fitting with Eq. 7.1 a set of point spectra acquired across the molecule. It shows two distinct T_K values with a sharp transition from one to the other, as evidenced by the profile taken along a cut through the center of the molecule. The bright areas seen on the dI/dV map at E_F display the lower T_K value and the peak-like line shape, while along the molecular axis T_K doubles and the Kondo effect leads to a dip. Differently from the spatial variation of T_K reported for TBrPP-Co molecules on Cu(111) [210] and for Fe(II)P on Au(111) [211], our system shows a sharp transition, without intermediate values of T_K . This abrupt transition between the two T_K values and line shapes hints toward the coexistence of two Kondo channels with different coupling to the conduction electrons of the substrate.

7.3 DFT calculations

To rationalize these findings, Dr. Gabriel Autès and Prof. Oleg Yazyev (Institute of theoretical Physics, EPFL) performed density functional theory calculations on this system. The generalized gradient approximation (GGA) was employed, with a mean-field Hubbard correction (GGA+ U , with $U=4$ eV) [175] as implemented in the QUANTUM-ESPRESSO package [176]. Calculations were made with ultrasoft pseudopotentials, a planewave cutoff of 30 Ryd and a Hubbard parameter U of 4 eV for the Fe and Co d -orbitals. Convergence was checked with respect to the cutoff and different values of U (namely $U=2$ eV and $U=3$ eV) were tested, obtaining very similar results. To take into account the van-der-Waals interaction between the molecule and the substrate, the semi-empirical long-range dispersion correction proposed by Grimme [212, 213] was included. A three layers thick Cu(111) slab model was constructed in a 6×6 supercell. On it a NC-Ph₃-CN molecule was added, oriented along a direction forming an angle of 4° with the second nearest neighbor direction (see Chapter 2), and attached to two Cu adatoms. An Fe or Co atom was placed below the central phenyl ring. The structure was

fully relaxed using a 2×2 k-points mesh until all residual forces were below 10^{-3} Ha/ a_0 . After relaxation, both transition metal adatoms sit on a bridge position of the Cu(111) substrate at ≈ 1.6 Å above the surface. The central ring of the NC-Ph₃-CN molecule is located at ≈ 3.1 Å above the substrate. The relaxed geometry of the NC-Ph₃-CN molecule with an Fe atom adsorbed below is shown in Fig. 7.3(a).

The density of states and magnetic properties were then computed self-consistently on a 4×4 k-points mesh. The atomic magnetic moment and the Löwdin population of the Fe and Co orbitals were obtained by projecting the Kohn-Sham wavefunctions onto a set of localized atomic orbitals.

The GGA+ U calculations predict an atomic magnetic moment of $2.1 \mu_B$ and $0.6 \mu_B$ for the buried Fe and Co, respectively. This indicates that the Fe atom is in a $S=1$ state. Table 7.1 shows the Löwdin spin up and spin down occupations [214] of the s and d orbitals for the buried Fe and Co atoms. The d orbitals of Co are all nearly completely filled, which explains the absence of a Kondo effect for this system, since there is no unpaired spin to be screened by the substrate conduction electrons. In the case of Fe, on the other hand, the diagonal orbitals, d_{xz} and d_{yz} , are both almost singly occupied and can thus contribute to the Kondo screening [215].

To have a better understanding of the molecular orbitals involved, a DFT calculation of a free standing NC-Ph₃-CN molecule with an Fe atom attached on the central ring was performed. The projected density of states of this system is shown in Fig. 7.3(b). The singly occupied orbitals which originate from the Fe d_{yz} and d_{xz} orbitals, labeled A and B respectively, are depicted in Fig. 7.3(c). A' and B' denote their unoccupied counterparts. Their local density of states projected on Fe and on NC-Ph₃-CN [Fig. 7.3(b)] shows that the B and B' orbitals possess a sizable weight on the molecule giving rise to a small magnetic moment ($0.3 \mu_B$) localized on the central molecular ring. By looking at the isodensity contour plot [Fig. 7.3(c)], we can see that A and A' are almost pure Fe states, with little or no hybridization with the molecule, while B and B' have a higher degree of hybridization and are delocalized on the molecular axis. The asymmetry between the hybridization of these two orbitals reflects the anisotropy observed in the STS measurements. Thus the observed Kondo effect arises from the presence of two screening channels, one extending perpendicular and the other parallel to the molecular axis.

Table 7.1: Löwdin population of the s and d atomic orbitals for Fe and Co atoms adsorbed under NC-Ph₃-CN on Cu(111).

	s	d_{z^2}	d_{xz}	d_{yz}	$d_{x^2-y^2}$	d_{xy}
Fe spin up	0.31	0.97	0.92	0.92	0.90	0.90
Fe spin down	0.30	0.94	0.19	0.20	0.65	0.60
Co spin up	0.30	0.96	0.85	0.86	0.85	0.85
Co spin down	0.30	0.95	0.67	0.64	0.80	0.80

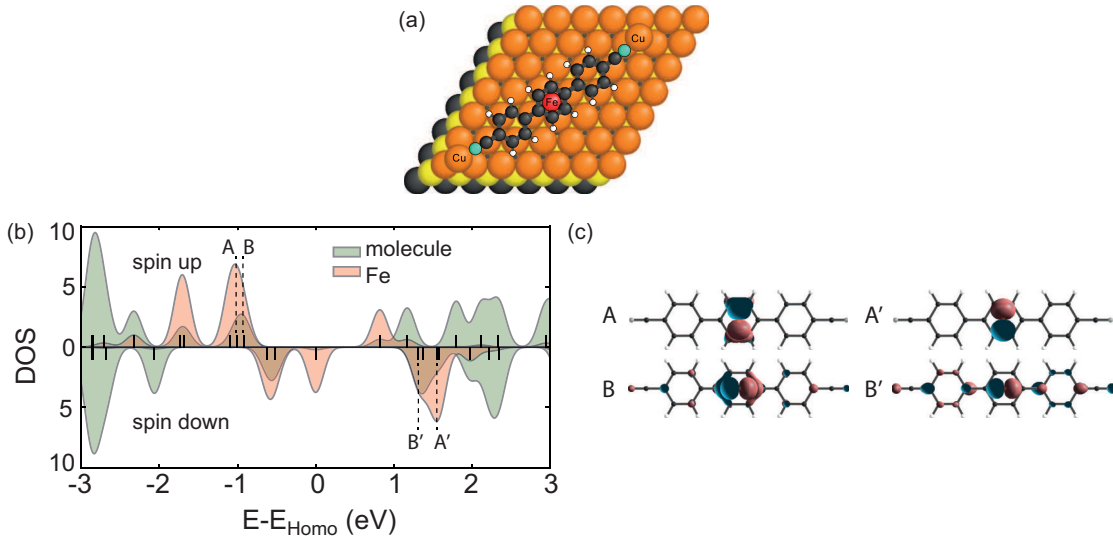


Figure 7.3: DFT results for the Fe-NC-Ph₃-CN system. (a) Relaxed geometry of the NC-Ph₃-CN molecule burying an Fe atom on top of Cu(111). (b) Spin resolved density of states used to represent molecular orbitals of the free standing Fe-molecule system, projected on the Fe atom (red) and on the molecule (green). (c) Isodensity surface ($0.002 e/a_0^3$) of the free standing Fe-molecule system wave functions corresponding to the two highest occupied majority spin Fe d orbitals (A,B) and to the two lowest unoccupied minority spin Fe d orbitals (A', B').

The first originates from the d_{yz} Fe orbital and is the most distant from E_F , and therefore has the lower T_K [189]. The spatial distribution of this state corresponds to the area where the peaks are observed in the STS. The second originates from d_{xz} , has a higher T_K and extends over the molecular backbone. It is the channel giving rise to the dip feature in STS. The dip in the conductance indicates that for this Kondo channel there is interference between two tunneling paths [216].

7.4 XAS and XMCD measurements

To investigate the degree of screening of both Kondo channels, we performed XAS and XMCD measurements at the EPFL/ PSI X-Treme beam line at the Swiss Light Source [54]. We recorded the $L_{2,3}$ absorption edges of Fe in the total electron yield mode. The Cu(111) preparation and the molecule deposition were performed in the preparation chamber of X-Treme [54], while Fe was deposited after the sample had been transferred *in-situ* into the cryostat. Molecule and Fe coverages were calibrated by crosscorrelating XAS spectra with the *in-situ* STM measurements, that were also employed to check the quality of the metal-organic honeycomb network structure.

Since the Fe deposition temperature controls the Fe abundance on the three adsorption sites on the $(\text{NC-Ph}_3\text{-CN})_3\text{Cu}_2/\text{Cu}(111)$ surface, we can produce samples with the Fe adatoms predominantly adsorbed on the Cu(111) substrate (sample A, $T_{\text{dep}} = 3$ K) and others where they are mostly below the molecules (sample B, $T_{\text{dep}} = 40$ K). Figures 7.4(a) and (b) compare XAS and XMCD recorded at the Fe $L_{2,3}$ absorption edges of two such samples. As expected, the

spectra of sample A are very similar to those measured for Fe atoms on the pristine Cu(111) surface seen in the previous chapter. In contrast, the XAS spectra of sample B show a broader L_3 absorption peak. As the shapes of the magnetization curves of samples A and B are identical [see inset of Fig. 7.4(b)], implying an equal response to the external magnetic field, we can conclude that the remaining magnetic signal of sample B originates entirely from residual Fe atoms on Cu(111). This is further confirmed by the observation that depositing additional Fe atoms on sample B at 3 K results in the recovery of the XAS shape and XMCD intensity, as seen in Fig. 7.5.

We can estimate the amount of Fe adsorbed on the Cu(111) surface on the sample on which Fe was evaporated at 40 K (sample B) by comparing the spectrum of this sample with the one of Fe on Cu(111) that was presented in the previous chapter. To separate the contribution of the Fe atoms on Cu(111) from the one of Fe atoms under molecules, we need to subtract the spectrum of Fe/Cu(111) from the one of sample B. However, the resulting XAS spectrum can never, by definition, be negative. This gives us a criterion for choosing the rescaling factor for the Fe spectra, whose maximum intensity compatible with a positive difference spectrum is shown in Fig. 7.6. In the grey circle, is highlighted the part of the spectra that would result in

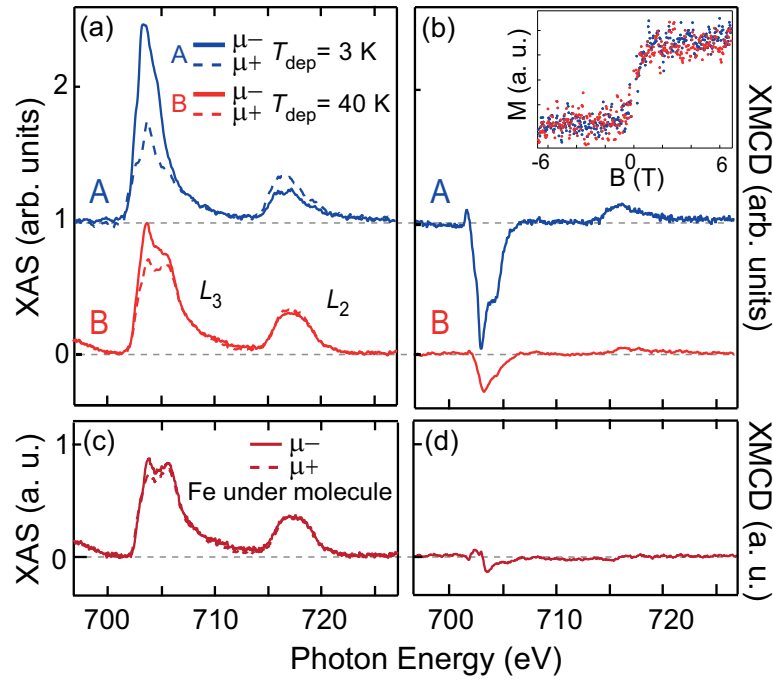


Figure 7.4: X-ray absorption spectroscopy and x-ray magnetic circular dichroism. (a) Fe $L_{2,3}$ XAS recorded with parallel (μ_+) and antiparallel (μ_-) circular polarization with respect to B , x-ray beam, and surface normal ($B = 6.8$ T, $T = 2.5$ K, $\Theta = (7 \pm 1) \times 10^{-3}$ ML). (b) XMCD of spectra in (a), $\mu_+ - \mu_-$. Inset: magnetization curves of samples A and B, obtained as the amplitude of the L_3 XMCD peak intensity at 703.5 eV divided by the pre-edge signal at 701.5 eV. Curves are scaled to the same saturation value. (c) XAS signal resulting from the subtraction of the contribution of Fe atoms on the bare substrate from spectra of sample B and (d) corresponding XMCD. All spectra are normalized to the XAS integral.

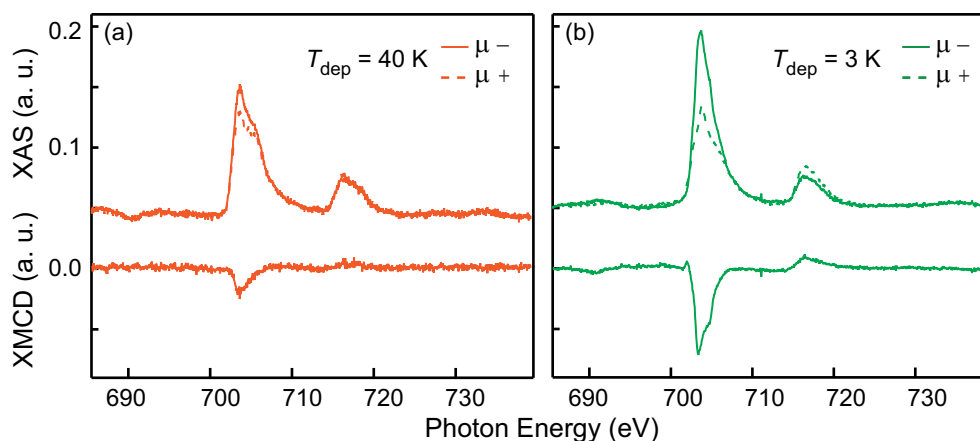


Figure 7.5: XAS and corresponding XMCD spectra of a sample on which Fe was evaporated at 40 K (a) and added on top at 3 K (b). The XAS shape and XMCD intensity in (b) are similar to the ones measured on the sample with Fe deposited directly at 3 K (sample A in Fig. 7.4).

a negative XAS in the difference spectrum if the Fe signal was more intense. Thanks to this analysis we can say that the amount of Fe adsorbed on the substrate in sample B is at most 20%.

Thus, to separate the contribution of the atoms adsorbed under molecules, we subtract 20% of the signal of Fe on the substrate from the spectra of sample B, obtaining the signal shown in Fig. 7.4(c). The total magnetic moment associated with the XMCD signal, Fig. 7.4(d), is at most $0.3 \mu_B$, while a non-screened spin 1 would result in a magnetic moment of $\approx 1.9 \mu_B$, as estimated using the Brillouin function. It is thus clear from these results that the spin in both orbitals is effectively Kondo screened.

It is interesting to note that both Fe atoms adsorbed under the molecules and Co atoms

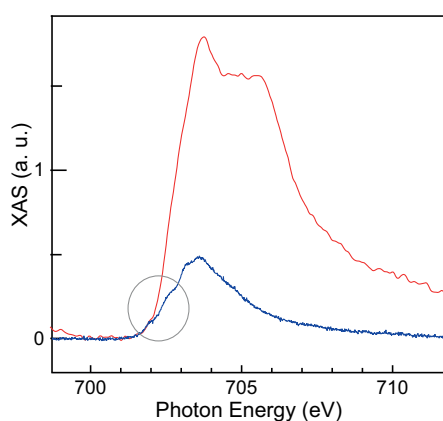


Figure 7.6: Zoom on the L_3 peak of the total XAS of sample B, with Fe deposited on the molecular network at 40 K (red), and total XAS of Fe atoms on Cu(111) (blue), rescaled so that the difference of the two spectra is always positive. Fe coverage is $\Theta = (7 \pm 1) \times 10^{-3} \text{ ML}$ for both samples.

on Cu(111) are $S = 1$ systems, with two singly-occupied orbitals. However, in the case of Co/Cu(111), the two orbitals are degenerate, resulting in a single value for T_K [217].

7.5 Conclusions

In conclusion, we have shown that the combination of transition metal atoms and organic molecules can suppress the Kondo effect in the case of Co, while inducing it for Fe, producing a regular array of Kondo impurities. In this system the presence of two screening channels originating from non degenerate orbitals with different spatial distributions gives rise to a Kondo effect with different signatures in the directions parallel and perpendicular to the molecular axis. The effective screening of the spin in both channels in this $S = 1$ metal-organic complex is demonstrated through XAS and XMCD measurements.

Chapter summary

Combining metal atoms with organic molecules can suppress or induce a Kondo effect:

- Co/Cu(111) is a Kondo system
- Co under NC-Ph₃-CN on Cu(111) is not a Kondo system
- Fe /Cu(111) is not a Kondo system
- Fe under NC-Ph₃-CN on Cu(111) is a Kondo system

For Fe atoms under NC-Ph₃-CN on Cu(111):

- STS measurements show two distinct T_K and line shapes
- DFT calculations show that there are two singly occupied Fe d orbitals, with different hybridization with the molecular orbitals
- XAS and XMCD measurements show that the magnetic moment of the system is suppressed, thus the spin in both channels is screened

Thus, we demonstrated the formation of a spatial dependent, two-channel metal-organic Kondo system, where both channels are Kondo screened.

8 Conclusions and perspectives

In this thesis, we have demonstrated how we can use self-assembly to obtain the formation of molecular networks with a variety of different geometries by tuning the molecular deposition conditions, such as the temperature of the substrate and the molecular coverage. For dicyanitrile polyphenyl molecules on Cu(111), we investigated deposition temperatures ranging from 300 to 140 K, observing by means of STM how the diminishing amount of Cu adatoms supplied by the surface with decreasing temperature results in a transition from fully metal-coordinated networks to purely organic ones, with an intermediate regular structure in which half of the nodes are Cu-coordinated and half stabilized by hydrogen bonds. We observed highly regular structures, both porous and compact. By comparing the structures formed by two kinds of molecules differing in the number of their phenyl rings, we revealed a competition between different interactions governing the assembly process. Indeed, the molecule-substrate and the molecule-adatom interactions can not be optimized at the same time, and while the first dominates the assembly of the longer molecules, the latter determines the organization of the shorter ones. We also investigated, using STS, how the unoccupied molecular orbitals are influenced by the organization of the molecules, by the kind of bond and by the molecular orientation with respect to the substrate.

It is well known that the choice of the substrate is a very important ingredient for molecular self-assembly: by adding a graphene decoupling layer on metal substrates, we were able to observe the self-assembly of single ion magnets that do not organize on the bare metal surface. XAS and XMCD measurements demonstrated that, indeed, the magnetic anisotropy of such samples has the maximum possible value, that of the molecular crystal.

The regular porous networks presented at the beginning of this thesis provide effective templates for the organization of metal atoms and clusters. Thanks to the various geometric structures that can be obtained, and to the distinct periodicities of the networks formed by molecules of different length, these molecular networks provide versatile templates. We demonstrated that the surface state confinement induced by the molecular structures leads to a neat organization of metal atoms and clusters at the center of the network pores.

We obtained for the first time, to the best of our knowledge, regular arrays of metal clusters with a narrow size distribution hosted in the network cavities. We demonstrated that our method can be extended to different classes of elements, ranging from transition metals to rare earths, successfully using Fe, Co and Er. We also produced mixed transition metal - rare

Chapter 8. Conclusions and perspectives

earth metal clusters, which have never been obtained before and which are expected to exhibit intriguing magnetic properties.

The same molecular networks can be also used as templates to organize metal atoms under the molecules. In particular, Fe atoms adsorbed under dicyanitrile polyphenyl molecules on Cu(111) proved very interesting from the magnetic point of view. To start with, we performed a systematic study of the magnetic properties of Fe atoms and small clusters adsorbed on Cu(111) by means of XAS, XMCD and theoretical methods.

Scanning tunneling spectroscopy revealed that the system formed by Fe atoms adsorbed under NC-Ph_n-CN molecules on Cu(111) exhibits a Kondo effect with a strong spatial dependence, with two different Kondo temperatures and line shapes. Density functional theory demonstrated that there are two singly occupied orbitals with different spatial distributions that could act as Kondo channels, and x-ray adsorption and dichroism measurements confirmed that both channels are effectively Kondo-screened. We showed that the combination of transition metal atoms and organic molecules can activate or suppress the Kondo effect: while Fe is not a Kondo system when adsorbed on the substrate but exhibits Kondo behavior when buried by molecules, the opposite is true for Co. Metal-organic systems where two Kondo channels are screened at the measuring temperature have been reported only once, and our system is the first to show such a strong spatial dependence.

Many aspects of this work can become the starting point of further investigations to exploit the most appealing features of the described systems.

For example, in this thesis we studied the properties and the self-assembly of polyphenyl-dicyanitrile molecules; we also saw how the use of decoupling layers can influence molecular organization. Moreover, the use of such layers gives better access to the electronic properties, as it usually makes it possible to measure the occupied molecular orbitals and to see finer details of the unoccupied ones. On decoupling layers the molecular orbitals are close to the gas phase ones thanks to the reduced hybridization with the substrate. It would thus be interesting to study the growth and organization of these molecules on substrates such as supported graphene and hexagonal boron nitride, alone and with codeposition of metal atoms. Such a system would be well suited also for the study of the magnetic properties of the coordination atoms, which are expected to be much more atomic-like on decoupling layers than on metal substrates. Moreover, their electronic structure can be changed by the coordination bonds, and the ligand field symmetry can be tuned modifying the coordination number. The highly regular distribution of these atoms on the surface would clearly be an advantage, as the homogeneity of the system would make it particularly suitable for measurements with spatially averaging techniques such as XAS and XMCD. Moreover, the typical periodicity of the networks allows for a very dense array of coordination atoms; the presence of the decoupling layer could result in a longer magnetization lifetime, leading to magnetic remanence. Such a system would be promising for applications in magnetic data storage systems.

The system constituted by the metal clusters organized in the network pores is expected to have very interesting properties both from the catalytic and from the magnetic point of view. In the biological fixation of nitrogen the FeMo cofactor, the active site of the enzyme nitrogenase [218, 219, 220], has the stoichiometric formula Fe₇MoS₉. Clusters containing

seven Fe atoms might thus be good candidates for catalytic ammonia synthesis at low temperature [221]. In this perspective, the array of Fe clusters presented in this thesis might be a good starting point for the search of a system where this reaction can happen at ambient temperature. To reach this goal, it would be necessary to increase the thermal stability of the metal-organic template, for example by using different functional groups at the molecular ends or different coordination atoms. For example, networks formed by NC-Ph_n-CN molecules with Co coordination atoms on Ag(111) are stable to temperatures up to 300 K [62]. Rare earth metals are known for their peculiar magnetic properties, determined by the localized nature of the 4*f* electrons, and well organized rare earth clusters are certainly worth investigating from this point of view. We showed the organization of Er clusters as a proof of principle, and we expect that similar results will be obtained with other rare earth elements. Mixed transition metal - rare earth metal clusters are new and, as the strongest known permanent magnets are composed of 3*d*-4*f* alloys, such clusters might possess significant magnetic properties, that could be revealed by x-ray absorption and dichroism studies. Thus, further studies of these or similar self-assembled metal-organic networks hosting ordered metal clusters will lead to a deeper understanding of the cluster properties both from the fundamental and from the technological point of view.

Bibliography

- [1] J. K. Gimzewski, E. Stoll, and R. R. Schlittler, "Scanning tunneling microscopy of individual molecules of copper phthalocyanine adsorbed on polycrystalline silver surfaces," *Surf. Sci.*, vol. 181, p. 267, 1986.
- [2] P. H. Lippel, R. J. Wilson, M. D. Miller, C. Wöll, and S. Chiang, "High-resolution imaging of copper-phthalocyanine by scanning-tunneling microscopy," *Phys. Rev. Lett.*, vol. 62, no. 2, p. 171, 1989.
- [3] S. A. Elrod, A. L. de Lozanne, and C. F. Quate, "Low-temperature vacuum tunneling microscopy," *Appl. Phys. Lett.*, vol. 45, p. 1240, 1984.
- [4] R. C. Jaklevic and J. Lambe, "Molecular vibration spectra by electron tunneling," *Phys. Rev. Lett.*, vol. 17, p. 1139, 1966.
- [5] G. Binnig, N. Garcia, and H. Rohrer, "Conductivity sensitivity of inelastic scanning tunneling microscopy," *Phys. Rev. B*, vol. 32, p. 1336, 1985.
- [6] B. C. Stipe, M. A. Rezaei, and W. Ho, "Single-molecule vibrational spectroscopy and microscopy," *Science*, vol. 280, no. 5370, p. 1732, 1998.
- [7] L. Turin, "A spectroscopic mechanism for primary olfactory reception," *Chemical Senses*, vol. 21, no. 6, p. 773, 1996.
- [8] H. J. Zandvliet and A. van Houselt, "Scanning tunneling spectroscopy," *Annu. Rev. Anal. Chem.*, vol. 2, no. 1, p. 3, 2009.
- [9] J. Gimzewski, R. Berndt, and R. Schlittler, "Observation of local photoemission using a scanning tunneling microscope," *Ultramicroscopy*, vol. 42-44, no. PART 1, p. 366, 1992.
- [10] R. Berndt, R. Gaisch, J. K. Gimzewski, B. Reihl, R. R. Schlittler, W. D. Schneider, and M. Tschudy, "Photon emission at molecular resolution induced by a scanning tunneling microscope," *Science*, vol. 262, no. 5138, p. 1425, 1993.
- [11] X. H. Qiu, G. V. Nazin, and W. Ho, "Vibrationally resolved fluorescence excited with submolecular precision," *Science*, vol. 299, no. 5606, p. 542, 2003.
- [12] B. Mann and H. Kuhn, "Tunneling through fatty acid salt monolayers," *J. Appl. Phys.*, vol. 42, p. 4398, 1971.

Bibliography

- [13] A. Aviram and M. A. Ratner, "Molecular rectifiers," *Chem. Phys. Lett.*, vol. 29, no. 2, p. 277, 1974.
- [14] M. A. Reed, C. Zhou, C. J. Muller, T. P. Burgin, and J. M. Tour, "Conductance of a molecular junction," *Science*, vol. 278, no. 5336, p. 252, 1997.
- [15] S. Reineke, M. Thomschke, B. Lüssem, and K. Leo, "White organic light-emitting diodes: Status and perspective," *Rev. Mod. Phys.*, vol. 85, p. 1245, 2013.
- [16] J. Roncali, P. Leriche, and P. Blanchard, "Molecular materials for organic photovoltaics: Small is beautiful," *Adv. Mater.*, vol. 26, no. 23, p. 3821, 2014.
- [17] S. Sanvito, "Molecular spintronics," *Chem. Soc. Rev.*, vol. 40, p. 3336, 2011.
- [18] M. Bode, M. Getzlaff, and R. Wiesendanger, "Spin-polarized vacuum tunneling into the exchange-split surface state of Gd(0001)," *Phys. Rev. Lett.*, vol. 81, p. 4256, 1998.
- [19] C. Iacovita, M. V. Rastei, B. W. Heinrich, T. Brumme, J. Kortus, L. Limot, and J. P. Bucher, "Visualizing the spin of individual cobalt-phthalocyanine molecules," *Phys. Rev. Lett.*, vol. 101, p. 116602, 2008.
- [20] H. W. Langmi, J. Ren, B. North, M. Mathe, and D. Bessarabov, "Hydrogen storage in metal-organic frameworks: A review," *Electrochim. Acta*, vol. 128, p. 368, 2014.
- [21] J. Liu, L. Chen, H. Cui, J. Zhand, L. Zhang, and C.-Y. Su, "Applications of metal-organic frameworks in heterogeneous supramolecular catalysis," *Chem. Soc. Rev.*, vol. 43, p. 6011, 2014.
- [22] J.-R. Li, R. J. Kuppler, and H.-C. Zhou, "Selective gas adsorption and separation in metal-organic frameworks," *Chem. Soc. Rev.*, vol. 38, p. 1477, 2009.
- [23] C.-Y. Sun, C. Qin, X.-L. Wang, and Z.-M. Su, "Metal-organic frameworks as potential drug delivery systems," *Expert Opin. Drug Del.*, vol. 10, no. 1, p. 89, 2013.
- [24] J. K. Gimzewski and C. Joachim, "Nanoscale science of single molecules using local probes," *Science*, vol. 283, no. 5408, p. 1683, 1999.
- [25] J. V. Barth, "Molecular architectonic on metal surfaces," *Annu. Rev. Phys. Chem.*, vol. 58, p. 375, 2007.
- [26] C. Becker and K. Wandelt, "Surfaces: Two-dimensional templates," in *Templates in Chemistry III* (P. Broekmann, K.-H. Dötz, and C. Schalley, eds.), vol. 287 of *Topics in Current Chemistry*, p. 45, 2009.
- [27] L. Bartels, "Tailoring molecular layers at metal surfaces," *Nat. Chem.*, vol. 2, p. 87, 2010.
- [28] J. E. Mondloch, M. J. Katz, W. C. Isley III, P. Ghosh, P. Liao, W. Bury, G. W. Wagner, M. G. Hall, J. B. DeCoste, G. W. Peterson, R. Q. Snurr, C. J. Cramer, J. T. Hupp, and O. K. Farha, "Destruction of chemical warfare agents using metal-organic frameworks," *Nat. Mater.*, vol. 14, p. 512, 2015.

- [29] M. Campbell, D. Sheberla, S. F. Liu, T. M. Swager, and M. Dincă, "Cu₃(hexaminotriphenylene)₂: an electrically conductive 2D metal–organic framework for chemiresistive sensing," *Angew. Chem. International Edition*, vol. 54, no. 14, p. 4349, 2015.
- [30] G. Binnig, H. Rohrer, C. Gerber, and E. Weibel, "Tunneling through a controllable vacuum gap," *Applied Physical Letters*, vol. 40, pp. 178–180, 1982.
- [31] G. Binnig and H. Rohrer, "Scanning tunneling microscopy from birth to adolescence," *Reviews of Modern Physics*, vol. 59, pp. 615–625, 1987.
- [32] G. Binnig, H. Rohrer, C. Gerber, and E. Weibel, "Surface studies by scanning tunneling microscopy," *Physical Review Letters*, vol. 49, pp. 57–61, 1982.
- [33] D. M. Eigler and E. K. Schweizer, "Positioning single atoms with a scanning tunneling microscope," *Nature*, vol. 344, pp. 524–526, 1990.
- [34] J. A. Stroscio and D. M. Eigler, "Atomic and molecular manipulation with the scanning tunneling microscope," *Science*, vol. 254, pp. 1319–1326, 1991.
- [35] G. Dujardin and P. Avouris, "Dissociation of individual molecules with electrons from the tip of a scanning tunneling microscope," *Science*, vol. 255, pp. 1232–1235, 1992.
- [36] H. J. Lee and W. Ho, "Single-bond formation and characterization with a scanning tunneling microscope," *Science*, vol. 286, pp. 1719–1722, 1999.
- [37] J. Bardeen, "Tunnelling from a many-particle point of view," *Phys. Rev. Lett.*, vol. 6, pp. 57–59, 1961.
- [38] C. Weiss, C. Wagner, C. Kleimann, M. Rohlfing, F. S. Tautz, and R. Temirov, "Imaging Pauli repulsion in scanning tunneling microscopy," *Phys. Rev. Lett.*, vol. 105, p. 086103, 2010.
- [39] R. Temirov, S. Soubatch, O. Neucheva, A. C. Lassise, and F. S. Tautz, "A novel method achieving ultra-high geometrical resolution in scanning tunnelling microscopy," *New J. Phys.*, vol. 10, p. 053012, 2008.
- [40] L. Gross, N. Moll, F. Mohn, A. Curioni, G. Meyer, F. Hanke, and M. Persson, "High-resolution molecular orbital imaging using a *p*-wave STM tip," *Phys. Rev. Lett.*, vol. 107, p. 086101, 2011.
- [41] P. Hapala, G. Kichin, C. Wagner, F. S. Tautz, R. Temirov, and P. Jelínek, "Mechanism of high-resolution STM/AFM imaging with functionalized tips," *Phys. Rev. B*, vol. 90, p. 085421, 2014.
- [42] C. Weiss, C. Wagner, R. Temirov, and F. S. Tautz, "Direct imaging of intermolecular bonds in scanning tunneling microscopy," *J. Am. Chem. Soc.*, vol. 132, p. 11864, 2010.

Bibliography

- [43] G. Kichin, C. Weiss, C. Wagner, F. S. Tautz, and R. Temirov, "Single molecule and single atom sensors for atomic resolution imaging of chemically complex surfaces," *J. Am. Chem. Soc.*, vol. 133, p. 16847, 2011.
- [44] R. Gaisch, J. K. Gimzewski, B. Reihl, R. R. Schlittler, M. Tschudy, and W. D. Schneider, "Low-temperature ultra-high vacuum scanning tunneling microscope," *Ultramicroscopy*, vol. 42-44, p. 1621, 1992.
- [45] R. Gaisch, *Scanning tunneling microscopy in ultra high vacuum at low temperature*. PhD thesis, Université de Lausanne, 1994.
- [46] F. Rossel, *Plasmon enhanced luminescence from fullerene molecules excited by local electron tunneling*. PhD thesis, EPFL, 2009.
- [47] E. Čavar, M.-C. Blüm, M. Pivetta, F. Patthey, M. Chergui, and W.-D. Schneider, "Fluorescence and phosphorescence from individual C₆₀ molecules excited by local electron tunneling," *Phys. Rev. Lett.*, vol. 95, p. 196102, 2005.
- [48] H. Ulbricht, J. Kriebel, G. Moos, and T. Hertel, "Desorption kinetics and interaction of Xe with single-wall carbon nanotube bundles," *Chem. Phys. Lett.*, vol. 363, no. 3–4, p. 252, 2002.
- [49] J. Stöhr, H. A. Padmore, S. Anders, T. Stammler, and M. R. Scheinfein, "Principles of x-ray magnetic dichroism spectromicroscopy," *Surf. Rev. Lett.*, vol. 05, p. 1297, 1998.
- [50] G. van der Laan, "Applications of soft x-ray magnetic dichroism," *J. Phys.: Conf. Ser.*, vol. 430, p. 012127, 2013.
- [51] B. T. Thole, P. Carra, F. Sette, and G. van der Laan, "X-ray circular dichroism as a probe of orbital magnetization," *Phys. Rev. Lett.*, vol. 68, p. 1943, 1992.
- [52] P. Carra, B. T. Thole, M. Altarelli, and X. Wang, "X-ray circular dichroism and local magnetic fields," *Phys. Rev. Lett.*, vol. 70, p. 694, 1993.
- [53] J. Stöhr, "Exploring the microscopic origin of magnetic anisotropies with X-ray magnetic circular dichroism (XMCD) spectroscopy," *J. Magn. Magn. Mater.*, vol. 200, no. 1, pp. 470–497, 1999.
- [54] C. Piamonteze, U. Flechsig, S. Rusponi, J. Dreiser, J. Heidler, M. Schmidt, R. Wetter, M. Calvi, T. Schmidt, H. Pruchova, J. Krempasky, C. Quitmann, H. Brune, and F. Nolting, "X-Treme beamline at SLS: X-ray magnetic circular and linear dichroism at high field and low temperature," *J. Synchrotron Radiat.*, vol. 19, p. 661, 2012.
- [55] J. V. Barth, J. Weckesser, N. Lin, A. Dmitriev, and K. Kern, "Supramolecular architectures and nanostructures at metal surfaces," *Appl. Phys. A*, vol. 76, p. 645, 2003.

- [56] T. Classen, M. Lingenfelder, Y. Wang, R. Chopra, C. Virojanadara, U. Starke, G. Costantini, G. Fratesi, S. Fabris, S. de Gironcoli, S. Baroni, S. Haq, R. Raval, and K. Kern, "Hydrogen and coordination bonding supramolecular structures of trimesic acid on Cu(110)," *J. Phys. Chem. A*, vol. 111, p. 12589, 2007.
- [57] Y.-F. Zhang, N. Zhu, and T. Komeda, "Mn-coordinated stillbenedicarboxylic ligand supramolecule regulated by the herringbone reconstruction of Au(111)," *J. Phys. Chem. C*, vol. 111, p. 16946, 2007.
- [58] H. Walch, J. Dienstmaier, G. Eder, R. Gutzler, S. Schlögl, T. Sirtl, K. Das, M. Schmittel, and M. Lackinger, "Extended two-dimensional metal-organic frameworks based on thiolate-copper coordination bonds," *J. Am. Chem. Soc.*, vol. 133, p. 7909, 2011.
- [59] S. L. Tait, A. Langner, N. Lin, S. Stepanow, C. Rajadurai, M. Ruben, and K. Kern, "One-dimensional self-assembled molecular chains on Cu(100): interplay between surface-assisted coordination chemistry and substrate commensurability," *J. Phys. Chem. C*, vol. 111, p. 10982, 2007.
- [60] Z. L. Shi, J. Liu, T. Lin, F. Xia, P. N. Liu, and N. Lin, "Thermodynamics and selectivity of two-dimensional metallo-supramolecular self-assembly resolved at molecular scale," *J. Am. Chem. Soc.*, vol. 133, p. 6150, 2011.
- [61] T. R. Umbach, M. Bernien, C. F. Hermanns, L. L. Sun, H. Mohrmann, K. E. Hermann, A. Krüger, N. Krane, Z. Yang, F. Nickel, Y.-M. Chang, K. J. Franke, J. I. Pascual, and W. Kuch, "Site-specific bonding of copper adatoms to pyridine end groups mediating the formation of two-dimensional coordination networks on metal surfaces," *Phys. Rev. B*, vol. 89, 2014.
- [62] U. Schlickum, R. Decker, F. Klappenberger, G. Zoppellaro, S. Klyatskaya, M. Ruben, I. Silanes, A. Arnau, K. Kern, H. Brune, and J. V. Barth, "Metal-organic honeycomb nanomeshes with tunable cavity size," *Nano Lett.*, vol. 7, p. 3813, 2007.
- [63] G. Pawin, K. L. Wong, D. Kim, D. Sun, L. Bartels, S. Hong, T. S. Rahman, R. Carp, and M. Marsella, "A surface coordination network based on substrate-derived metal adatoms with local charge excess," *Angew. Chem. Int. Ed.*, vol. 47, p. 8442, 2008.
- [64] T. Sirtl, S. Schlögl, A. Rastgoo-Lahrood, J. Jelic, S. Neogi, M. Schmittel, W. M. Heckl, K. Reuter, and M. Lackinger, "Control of intermolecular bonds by deposition rates at room temperature: hydrogen bonds versus metal coordination in trinitrile monolayers," *J. Am. Chem. Soc.*, vol. 135, p. 691, 2013.
- [65] U. Schlickum, R. Decker, F. Klappenberger, G. Zoppellaro, S. Klyatskaya, W. Auwärter, S. Neppel, K. Kern, H. Brune, M. Ruben, and J. V. Barth, "Chiral kagome lattice from simple ditopic molecular bricks," *J. Am. Chem. Soc.*, vol. 130, p. 11778, 2008.
- [66] A. Breittruck, H. E. Hoster, C. Meier, U. Ziener, and R. J. Behm, "Interaction of Cu atoms with ordered 2D oligopyridine networks," *Surf. Sci.*, vol. 601, p. 4200, 2007.

Bibliography

- [67] A. Breitruck, H. E. Hoster, and R. J. Behm, "Short-range order in a metal-organic network," *J. Phys. Chem. C*, vol. 113, p. 21265, 2009.
- [68] J. Liu, T. Lin, Z. Shi, F. Xia, L. Dong, P. N. Liu, and N. Lin, "Structural transformation of two-dimensional metal-organic coordination networks driven by intrinsic in-plane compression," *J. Am. Chem. Soc.*, vol. 133, p. 18760, 2011.
- [69] Z. L. Shi, T. Lin, J. Liu, P. N. Liu, and N. Lin, "Regulating a two-dimensional metallo-supramolecular self-assembly of multiple outputs," *Cryst. Eng. Comm*, vol. 13, p. 5532, 2011.
- [70] A. Langner, S. L. Tait, N. Lin, R. Chandrasekar, M. Ruben, and K. Kern, "Ordering and stabilization of metal-organic coordination chains by hierarchical assembly through hydrogen bonding at a surface," *Angew. Chem. Int. Ed.*, vol. 47, p. 8835, 2008.
- [71] D. Heim, D. Ecija, K. Seutert, W. Auwärter, C. Aurisicchio, C. Fabbro, D. Bonifazi, and J. V. Barth, "Self-assembly of flexible one-dimensional coordination polymers on metal surfaces," *J. Am. Chem. Soc.*, vol. 132, p. 6783, 2010.
- [72] M. Matena, M. Stöhr, T. Riehm, J. Björk, S. Martens, M. S. Dyer, M. Persson, J. Lobo-Checa, K. Müller, M. Enache, H. Wadepohl, J. Zegenhagen, T. A. Jung, and L. H. Gade, "Aggregation and contingent metal/surface reactivity of 1,3,8,10-tetraazaperopyrene (TAPP) on Cu(111)," *Chem. Eur. J.*, vol. 16, p. 2079, 2010.
- [73] W. H. Wang, S. Y. Wang, Y. N. Hong, B. Z. Tang, and N. Lin, "Selective supramolecular assembly of multifunctional ligands on a Cu(111) surface: metallacycles, propeller trimers and linear chains," *Chem. Commun.*, vol. 47, p. 10073, 2011.
- [74] D. Ecija, S. Vijayaraghavan, W. Auwärter, S. Joshi, K. Seufert, C. Aurisicchio, D. Bonifazi, and J. V. Barth, "Two-dimensional short-range disordered crystalline networks from flexible molecular modules," *ACS Nano*, vol. 6, p. 4258, 2012.
- [75] G. Schulze Icking-Konert, M. Giesen, and H. Ibach, "Decay of Cu adatom islands on Cu(111)," *Surf. Sci.*, vol. 398, p. 37, 1998.
- [76] M. Giesen, "Scaling transition of the time dependence of step fluctuations on Cu(111)," *Surf. Sci.*, vol. 442, p. 543, 1999.
- [77] P. J. Feibelman, "Formation and diffusion of S-decorated Cu clusters on Cu(111)," *Phys. Rev. Lett.*, vol. 985, p. 606, 2000.
- [78] R. Gomer, "Diffusion of adsorbates on metal surfaces," *Rep. Prog. Phys.*, vol. 53, p. 917, 1990.
- [79] M. Pivetta, G. E. Pacchioni, E. Fernandes, and H. Brune, "Temperature-dependent self-assembly of NC-Ph₅-CN molecules on Cu(111)," *J. Chem. Phys.*, vol. 142, p. 101928, 2015.

- [80] M. E. Cañas-Ventura, K. Aït-Mansour, P. Ruffieux, R. Rieger, K. Müllen, H. Brune, and R. Fasel, "Complex interplay and hierarchy of interactions in two-dimensional supramolecular assemblies," *ACS Nano*, vol. 5, p. 457, 2011.
- [81] C. R. L. Chapman, E. C. Ting, A. Kereszti, and I. Paci, "Self-assembly of cysteine dimers at the gold surface: A computational study of competing interactions," *J. Phys. Chem. C*, vol. 117, pp. 19426–19435, 2013.
- [82] S. Gottardi, K. Müller, J. C. Moreno-López, H. Yildirim, U. Meinhardt, M. Kivala, A. Kara, and M. Stöhr, "Cyano-functionalized triarylaminos on Au(111): Competing intermolecular versus molecule/substrate interactions," *Adv. Mater. Interfaces*, vol. 1, p. 1300025, 2014.
- [83] N. Ashcroft and N. Mermin, *Solid State Physics*. Philadelphia: Saunders College, 1976.
- [84] T. S. Chwee and M. B. Sullivan, "Adsorption studies of C₆H₆ on Cu (111), Ag (111), and Au (111) within dispersion corrected density functional theory," *J. Chem. Phys.*, vol. 137, p. 134703, 2012.
- [85] W. Reckien, M. Eggers, and T. Bredow, "Theoretical study of the adsorption of benzene on coinage metals," *Beilstein J. Org. Chem.*, vol. 10, p. 1775, 2014.
- [86] M. J. S. Spencer and G. L. Nyberg, "DFT modelling of hydrogen on Cu(110)- and (111)-type clusters," *Mol. Simulat.*, vol. 28, p. 807, 2002.
- [87] P. J. Feibelman and D. R. Hamann, "Theory of H bonding and vibration on close-packed metal surfaces," *J. Vac. Sci. Technol. A*, vol. 5, p. 424, 1987.
- [88] D. Kühne, F. Klappenberger, R. Decker, U. Schlickum, H. Brune, S. Klyatskaya, M. Ruben, and J. V. Barth, "Self-assembly of nanoporous chiral networks with varying symmetry from sexiphenyl-dicarbonitrile on Ag(111)," *J. Phys. Chem. C*, vol. 113, p. 17851, 2009.
- [89] A. Bogicevic, S. Ovesson, P. Hyldgaard, B. I. Lundqvist, H. Brune, and D. R. Jennison, "Nature, strength, and consequences of indirect adsorbate interactions on metals," *Phys. Rev. Lett.*, vol. 85, p. 1910, 2000.
- [90] N. Knorr, H. Brune, M. Epple, A. Hirstein, M. A. Schneider, and K. Kern, "Long-range adsorbate interactions mediated by a two-dimensional electrons gas," *Phys. Rev. B*, vol. 65, p. 115420, 2002.
- [91] J. Repp, G. Meyer, K.-H. Rieder, and P. Hyldgaard, "Site determination and thermally assisted tunneling in homogenous nucleation," *Phys. Rev. Lett.*, vol. 91, p. 206102, 2003.
- [92] N. Abdurakhmanova, A. Floris, T.-C. Tseng, A. Comisso, S. Stepanow, A. De Vita, and K. Kern, "Stereoselectivity and electrostatics in charge-transfer Mn- and Cs-TCNQ₄ networks on Ag(100)," *Nat. Commun.*, vol. 3, p. 940, 2012.

Bibliography

- [93] U. Schlickum, F. Klappenberger, R. Decker, G. Zoppellaro, S. Klyatskaya, M. Ruben, K. Kern, H. Brune, and J. V. Barth, "Surface-confined metal-organic nanostructures from Co-directed assembly of linear terphenyl-dicarbonitrile linkers on Ag(111)," *J. Phys. Chem. C*, vol. 114, p. 15602, 2010.
- [94] G. Tomba, M. Stengel, W.-D. Schneider, A. Baldereschi, and A. De Vita, "Supramolecular self-assembly driven by electrostatic repulsion: the 1D aggregation of rubrene pentagons on Au(111)," *ACS Nano*, vol. 4, p. 7545, 2010.
- [95] J. V. Barth, J. Weckesser, C. Cai, P. Günter, L. Bürgi, O. Jeandupeux, and K. Kern, "Building supramolecular nanostructures at surfaces by hydrogen bonding," *Ang. Chem. Int. Ed.*, vol. 39, p. 1230, 2000.
- [96] D. Kühne, F. Klappenberger, R. Decker, U. Schlickum, H. Brune, S. Klyatskaya, M. Ruben, and J. V. Barth, "Self-assembly of nanoporous chiral networks with varying symmetry from sexiphenyl-dicarbonitrile on Ag(111)," *J. Phys. Chem. C*, vol. 113, p. 17851, 2009.
- [97] P. Brocorens, E. Zojer, J. Cornil, Z. Shuai, G. Leising, K. Müllen, and J. Brédas, "Theoretical characterization of phenylene-based oligomers, polymers, and dendrimers," *Synthetic Met.*, vol. 100, pp. 141 – 162, 1999.
- [98] J. I. Urgel, D. Écija, W. Auwärter, A. C. Papageorgiou, A. P. Seitsonen, S. Vijayaraghavan, S. Joshi, S. Fischer, J. Reichert, and J. V. Barth, "Five-vertex lanthanide coordination on surfaces: A route to sophisticated nanoarchitectures and tessellations," *J. Phys. Chem. C*, vol. 118, no. 24, p. 12908, 2014.
- [99] T.-C. Tseng, C. Lin, X. Shi, S. L. Tait, U. Liu, X. and Starke, N. Lin, R. Zhang, C. Minot, M. A. Van H., J. I. Cerdá, and K. Kern, "Two-dimensional metal-organic coordination networks of Mn-7,7,8,8-tetracyanoquinodimethane assembled on Cu(100): Structural, electronic, and magnetic properties," *Phys. Rev. B*, vol. 80, p. 155458, 2009.
- [100] D. Kühne, F. Klappenberger, R. Decker, U. Schlickum, H. Brune, S. Klyatskaya, M. Ruben, and J. V. Barth, "High-quality 2D metal-organic coordination network providing giant cavities within mesoscale domains," *J. Am. Chem. Soc.*, vol. 131, p. 3881, 2009.
- [101] F. Klappenberger, D. Kühne, M. Marschall, S. Nepl, W. Krenner, A. Nefedov, T. Strunskus, K. Fink, C. Wöll, S. Klyatskaya, O. Fuhr, M. Ruben, and J. V. Barth, "Uniform π -system alignment in thin films of template-grown dicarbonitrile-oligophenyls," *Adv. Funct. Mater.*, vol. 21, p. 1631, 2011.
- [102] S.-W. Hla, K.-F. Braun, B. Wassermann, and K.-H. Rieder, "Controlled low-temperature molecular manipulation of sexiphenyl molecules on Ag(111) using scanning tunneling microscopy," *Phys. Rev. Lett.*, vol. 93, p. 208302, 2004.
- [103] M. Pivetta, G. E. Pacchioni, U. Schlickum, J. V. Barth, and H. Brune, "Formation of Fe cluster superlattice in a metal-organic quantum-box network," *Phys. Rev. Lett.*, vol. 110, p. 086102, 2013.

- [104] J. Björk, M. Matena, M. S. Dyer, M. Enache, J. Lobo-Checa, L. H. Gade, T. A. Jung, M. Stöhr, and M. Persson, "STM fingerprint of molecule-atom interactions in a self-assembled metal-organic surface coordination network on Cu(111)," *Phys. Chem. Chem. Phys.*, vol. 12, p. 8815, 2010.
- [105] S. Vijayaraghavan, D. Eciija, W. Auwärter, S. Joshi, K. Seufert, M. Drach, D. Nieckarz, P. Szabelski, C. Aurisicchio, D. Bonifazi, and J. V. Barth, "Supramolecular assembly of interfacial nanoporous networks with simultaneous expression of metal-organic and organic-bonding motifs," *Chem. Eur. J.*, vol. 19, p. 14143, 2013.
- [106] M. Roos, B. Uhl, D. Künzel, H. E. Hoster, A. Groß, and J. R. Behm, "Intermolecular vs molecule-substrate interactions: a combined STM and theoretical study of supramolecular phases on graphene/Ru(0001)," *Beilstein J. Nanotechnol.*, vol. 2, p. 365, 2011.
- [107] P. Järvinen, S. K. Hämäläinen, K. Banerjee, P. Häkkinen, M. Ijäs, A. Harju, and P. Liljeroth, "Molecular self-assembly on graphene on SiO₂ and h-BN substrates," *Nano Lett.*, vol. 13, no. 7, p. 3199, 2013.
- [108] S. K. Hämäläinen, M. Stepanova, R. Drost, P. Liljeroth, J. Lahtinen, and J. Sainio, "Self-assembly of cobalt-phthalocyanine molecules on epitaxial graphene on Ir(111)," *J. Phys. Chem. C*, vol. 116, no. 38, p. 20433, 2012.
- [109] J. M. MacLeod and F. Rosei, "Molecular self-assembly on graphene," *Small*, vol. 10, no. 6, p. 1038, 2014.
- [110] A. Caneschi, D. Gatteschi, R. Sessoli, A. L. Barra, L. C. Brunel, and M. Guillot, "Alternating current susceptibility, high field magnetization, and millimeter band EPR evidence for a ground $S = 10$ state in $[\text{Mn}_{12}\text{O}_{12}(\text{CH}_3\text{COO})_{16}(\text{H}_2\text{O})_4] \cdot 2\text{CH}_3\text{COOH} \cdot 4\text{H}_2\text{O}$," *J. Am. Chem. Soc.*, vol. 113, no. 15, p. 5873, 1991.
- [111] R. Sessoli, D. Gatteschi, A. Caneschi, and M. A. Novak, "Magnetic bistability in a metal-ion cluster," *Nature*, vol. 365, no. 6442, p. 141, 1993.
- [112] G. Christou, D. Gatteschi, D. N. Hendrickson, and R. Sessoli, "Single-molecule magnets," *MRS Bulletin*, vol. 25, p. 66, 2000.
- [113] A. R. Rocha, V. M. García-suárez, S. W. Bailey, C. J. Lambert, J. Ferrer, and S. Sanvito, "Towards molecular spintronics," *Nat. Mater.*, vol. 4, no. 4, p. 335, 2005.
- [114] N. Ishikawa, M. Sugita, T. Ishikawa, S. Koshihara, and Y. Kaizu, "Mononuclear lanthanide complexes with a long magnetization relaxation time at high temperatures: a new category of magnets at the single molecular level," *J. Phys. Chem. B*, vol. 108, p. 11265, 2004.
- [115] D. N. Woodruff, R. E. P. Winpenny, and R. A. Layfield, "Lanthanide single-molecule magnets," *Chem. Rev.*, vol. 113, no. 7, p. 5110, 2013.

Bibliography

- [116] H. L. C. Feltham and S. Brooker, "Review of purely 4f and mixed-metal nd-4f single-molecule magnets containing only one lanthanide ion," *Coord. Chem. Rev.*, vol. 276, p. 1, 2014.
- [117] J. Dreiser, "Molecular lanthanide single-ion magnets: from bulk to submonolayers," *Journal Phys.: Condens. Matter*, vol. 27, no. 18, p. 183203, 2015.
- [118] B. M. Flanagan, P. V. Bernhardt, E. R. Krausz, S. R. Lüthi, and M. J. Riley, "Ligand-field analysis of an Er(III) complex with a heptadentate tripodal N₄O₃ ligand," *Inorg. Chem.*, vol. 40, no. 21, p. 5401, 2001.
- [119] K. S. Pedersen, L. Ungur, M. Sigrüst, A. Sundt, M. Schau-Magnussen, V. Vieru, H. Mutka, S. Rols, H. Weihe, O. Waldmann, L. F. Chibotaru, J. Bendix, and J. Dreiser, "Modifying the properties of 4f single-ion magnets by peripheral ligand functionalisation," *Chem. Sci.*, vol. 5, p. 1650, 2014.
- [120] J. Dreiser, C. Wäckerlin, M. E. Ali, C. Piamonteze, F. Donati, A. Singha, K. S. Pedersen, S. Rusponi, J. Bendix, M. Oppeneer, T. A. Jung, and H. Brune, "Exchange interaction of strongly anisotropic tripodal erbium single-ion magnets with metallic surfaces," *ACS Nano*, vol. 8, no. 5, p. 4662, 2014.
- [121] S. Kahle, Z. Deng, N. Malinowski, C. Tonnoir, A. Forment-Aliaga, N. Thontasen, G. Rinke, D. Le, V. Turkowski, T. S. Rahman, S. Rauschenbach, M. Ternes, and K. Kern, "The quantum magnetism of individual manganese-12-acetate molecular magnets anchored at surfaces," *Nano Lett.*, vol. 12, no. 1, p. 518, 2012.
- [122] P. Erler, P. Schmitt, N. Barth, A. Irmler, S. Bouvron, T. Huhn, U. Groth, F. Pauly, L. Gragnaniello, and M. Fonin, "Highly ordered surface self-assembly of Fe₄ single molecule magnets," *Nano Lett.*, vol. 15, no. 7, p. 4546, 2015.
- [123] S. Marchini, S. Günther, and J. Wintterlin, "Scanning tunneling microscopy of graphene on Ru(0001)," *Phys. Rev. B*, vol. 76, p. 075429, 2007.
- [124] J. Wintterlin and M.-L. Bocquet, "Graphene on metal surfaces," *Surf. Sci.*, vol. 603, no. 10–12, p. 1841, 2009.
- [125] J. Mao, H. Zhang, Y. Jiang, Y. Pan, M. Gao, W. Xiao, and H.-J. Gao, "Tunability of supramolecular kagome lattices of magnetic phthalocyanines using graphene-based moiré patterns as templates," *J. Am. Chem. Soc.*, vol. 131, no. 40, p. 14136, 2009.
- [126] H. G. Zhang, J. T. Sun, T. Low, L. Z. Zhang, Y. Pan, Q. Liu, J. H. Mao, H. T. Zhou, H. M. Guo, S. X. Du, F. Guinea, and H.-J. Gao, "Assembly of iron phthalocyanine and pentacene molecules on a graphene monolayer grown on Ru(0001)," *Phys. Rev. B*, vol. 84, p. 245436, 2011.
- [127] K. Yang, W. D. Xiao, Y. H. Jiang, H. G. Zhang, L. W. Liu, J. H. Mao, H. T. Zhou, S. X. Du, and H.-J. Gao, "Molecule–substrate coupling between metal phthalocyanines and epitaxial

- graphene grown on Ru(0001) and Pt(111),” *J. Phys. Chem. C*, vol. 116, no. 26, p. 14052, 2012.
- [128] M. Schmid, G. Kresse, A. Buchsbaum, E. Napetschnig, S. Gritschneider, M. Reichling, and P. Varga, “Nanotemplate with holes: Ultrathin alumina on Ni₃Al(111),” *Phys. Rev. Lett.*, vol. 99, p. 196104, 2007.
- [129] H. Brune, M. Giovannini, K. Bromann, and K. Kern, “Self-organized growth of nanostructure arrays on strain-relief patterns,” *Nature*, vol. 394, p. 451, 1998.
- [130] R. Decker, U. Schlickum, F. Klappenberger, G. Zoppellaro, S. Klyatskaya, M. Ruben, J. V. Barth, and H. Brune, “Using metal-organic templates to steer the growth of Fe and Co nanoclusters,” *Appl. Phys. Lett.*, vol. 93, p. 243102, 2008.
- [131] S. Nowakowska, A. Wäckerlin, S. Kawai, T. Ivas, J. Nowakowski, S. Fatayer, C. Wäckerlin, T. Nijs, E. Meyer, J. Björk, M. Stöhr, L. H. Gade, and T. A. Jung, “Interplay of weak interactions in the atom-by-atom condensation of xenon within quantum boxes,” *Nat. Commun.*, vol. 6, no. 6071, p. 1, 2015.
- [132] P. Hyldgaard and M. Persson, “Long-ranged adsorbate-adsorbate interactions mediated by a surface state band,” *J. Phys.: Condens. Matter*, vol. 12, p. L13, 2000.
- [133] J. Repp, F. Moresco, G. Meyer, K. H. Rieder, P. Hyldgaard, and M. Persson, “Substrate mediated long-range oscillatory interaction between adatoms: Cu/Cu(111),” *Phys. Rev. Lett.*, vol. 85, p. 2981, 2000.
- [134] N. Knorr, M. A. Schneider, L. Diekhöner, P. Wahl, and K. Kern, “Kondo effect of single Co adatoms on Cu surfaces,” *Phys. Rev. Lett.*, vol. 88, p. 096804, 2002.
- [135] F. Silly, M. Pivetta, M. Ternes, F. Patthey, J. P. Pelz, and W. D. Schneider, “Creation of an atomic superlattice by immersing metallic adatoms in a two-dimensional electron sea,” *Phys. Rev. Lett.*, vol. 92, p. 016101, 2004.
- [136] H. F. Ding, V. S. Stepanyuk, P. A. Ignatiev, N. N. Negulyaev, L. Niebergall, M. Wasniowska, C. L. Gao, P. Bruno, and J. Kirschner, “Self-organized long-period adatom strings on stepped metal surfaces: Scanning tunneling microscopy, *ab initio* calculations, and kinetic Monte Carlo simulations,” *Phys. Rev. B*, vol. 76, p. 033409, 2007.
- [137] Y. Pennec, W. Auwärter, A. Schiffrin, A. Weber-Bargioni, A. Riemann, and J. V. Barth, “Supramolecular gratings for tuneable confinement of electrons on metal surfaces,” *Nat. Nanotechnol.*, vol. 2, p. 99, 2007.
- [138] N. N. Negulyaev, V. S. Stepanyuk, L. Niebergall, P. Bruno, W. Hergert, J. Repp, K.-H. Rieder, and G. Meyer, “Direct evidence for the effect of quantum confinement of surface-state electrons on atomic diffusion,” *Phys. Rev. Lett.*, vol. 101, p. 226601, 2008.

Bibliography

- [139] A. Schiffrin, J. Reichert, W. Auwärter, G. Jahnz, Y. Pennec, A. Weber-Bargioni, V. S. Stepanyuk, L. Niebergall, P. Bruno, and J. V. Barth, "Self-aligning atomic strings in surface-supported biomolecular gratings," *Phys. Rev. B*, vol. 78, p. 035424, 2008.
- [140] Z. Cheng, J. Wyrick, M. Luo, D. Sun, D. Kim, Y. Zhu, W. Lu, K. Kim, T. L. Einstein, and L. Bartels, "Adsorbates in a box: Titration of substrate electronic states," *Phys. Rev. Lett.*, vol. 105, p. 066104, 2010.
- [141] M. F. Crommie, C. P. Lutz, and D. M. Eigler, "Confinement of electrons to quantum corrals on a metal surface," *Science*, vol. 262, p. 218, 1993.
- [142] J. Kliewer, R. Berndt, and S. Crampin, "Scanning tunnelling spectroscopy of electron resonators," *New J. Phys.*, vol. 3, p. 22, 2001.
- [143] N. Kepčija, T.-J. Huang, F. Klappenberger, and J. V. Barth, "Quantum confinement in self-assembled two-dimensional nanoporous honeycomb networks at close-packed metal surfaces," *J. Chem. Phys.*, vol. 142, no. 10, p. 101931, 2015.
- [144] J. Li, W. D. Schneider, S. Crampin, and R. Berndt, "Tunnelling spectroscopy of surface state scattering and confinement," *Surf. Sci.*, vol. 95, p. 422, 1999.
- [145] L. Niebergall, G. Rodary, H. F. Ding, D. Sander, V. S. Stepanyuk, P. Bruno, and J. Kirschner, "Electron confinement in hexagonal vacancy islands: theory and experiment," *Phys. Rev. B*, vol. 74, p. 195436, 2006.
- [146] N. N. Negulyaev, V. S. Stepanyuk, L. Niebergall, P. Bruno, W. Auwärter, Y. Pennec, G. Jahnz, and J. V. Barth, "Effect of strain relaxations on heteroepitaxial metal-on-metal island nucleation and superlattice formation: Fe on Cu(111)," *Phys. Rev. B*, vol. 79, p. 195411, 2009.
- [147] X. P. Zhang, B. F. Miao, L. Sun, C. L. Gao, A. Hu, H. F. Ding, and J. Kirschner, "Atomic superlattice formation mechanism revealed by scanning tunneling microscopy and kinetic Monte Carlo simulations," *Phys. Rev. B*, vol. 81, p. 125438, 2010.
- [148] Y. Mo, K. Varga, E. Kaxiras, and Z. Y. Zhang, "Kinetic pathway for the formation of Fe nanowires on stepped Cu(111) surfaces," *Phys. Rev. Lett.*, vol. 94, p. 155503, 2005.
- [149] V. S. Stepanyuk, N. N. Negulyaev, L. Niebergall, and P. Bruno, "Effect of quantum confinement of surface electrons on adatom-adatom interactions," *New J. Phys.*, vol. 9, p. 388, 2007.
- [150] D. Y. Zhong, J. Franke, T. Blömker, G. Erker, L. F. Chi, and H. Fuchs, "Manipulating surface diffusion ability of single molecules by scanning tunneling microscopy," *Nano Lett.*, vol. 9, p. 132, 2009.
- [151] D. V. Tsvilin, V. S. Stepanyuk, W. Hergert, and J. Kirschner, "Effect of mesoscopic relaxations on diffusion of Co adatoms on Cu(111)," *Phys. Rev. B*, vol. 68, p. 205411, 2003.

- [152] F. D. Natterer, F. Patthey, and H. Brune, "Quantifying residual hydrogen adsorption in low-temperature STMs," *Surf. Sci.*, vol. 615, p. 80, 2013.
- [153] R. Skomski and D. Sellmyer, "Anisotropy of rare-earth magnets," *J. Rare Earth.*, vol. 27, no. 4, p. 675, 2009.
- [154] D. Ćcija, J. I. Urgel, A. C. Papageorgiou, S. Joshi, W. Auwärter, A. P. Seitsonen, S. Klyatskaya, M. Ruben, S. Fischer, S. Vijayaraghavan, J. Reichert, and J. V. Barth, "Five-vertex archimedean surface tessellation by lanthanide-directed molecular self-assembly," *P. Natl. Acad. Sci. USA*, vol. 110, no. 17, p. 6678, 2013.
- [155] A. Kornienko, L. Huebner, D. Freedman, T. J. Emge, and J. G. Brennan, "Lanthanide-transition metal chalcogenido cluster materials," *Inorg. Chem.*, vol. 42, no. 25, p. 8476, 2003.
- [156] J.-W. Cheng, J. Zhang, S.-T. Zheng, M.-B. Zhang, and G.-Y. Yang, "Lanthanide-transition-metal sandwich framework comprising Cu_3 cluster pillars and layered networks of Er_{36} wheels," *Angew. Chem.*, vol. 118, no. 1, p. 79, 2006.
- [157] A. A. Khajetoorians, J. Wiebe, B. Chilian, and R. Wiesendanger, "Realizing all-spin-based logic operations atom by atom," *Science*, vol. 332, p. 1062, 2011.
- [158] A. A. Khajetoorians, J. Wiebe, B. Chilian, S. Lounis, S. Blügel, and R. Wiesendanger, "Atom-by-atom engineering and magnetometry of tailored nanomagnets," *Nat. Phys.*, vol. 8, p. 497, 2012.
- [159] A. A. Khajetoorians, B. Baxevanis, C. Hübner, T. Schlenk, S. Krause, T. O. Wehling, S. Lounis, A. Lichtenstein, D. Pfannkuche, J. Wiebe, and R. Wiesendanger, "Current-driven spin dynamics of artificially constructed quantum magnets," *Science*, vol. 339, p. 55, 2013.
- [160] A. A. Khajetoorians, S. Lounis, B. Chilian, A. T. Costa, L. Zhou, D. L. Mills, J. Wiebe, and R. Wiesendanger, "Itinerant nature of atom-magnetization excitation by tunneling electrons," *Phys. Rev. Lett.*, vol. 106, p. 037205, 2011.
- [161] C. Carbone, M. Veronese, P. Moras, S. Gardonio, C. Grazioli, P. H. Zhou, O. Rader, A. Varykhalov, C. Krull, T. Balashov, A. Mugarza, P. Gambardella, S. Lebègue, O. Eriksson, M. I. Katsnelson, and A. I. Lichtenstein, "Correlated electrons step by step: itinerant-to-localized transition of Fe impurities in free-electron metal hosts," *Phys. Rev. Lett.*, vol. 104, p. 117601, 2010.
- [162] A. Lehnert, *Magnetism of individual adatoms and of epitaxial monolayers*. PhD thesis, EPFL, 2009.
- [163] A. A. Khajetoorians, T. Schlenk, B. Schweffinghaus, M. dos Santos Dias, M. Steinbrecher, M. Bouhassoune, S. Lounis, J. Wiebe, and R. Wiesendanger, "Spin excitations of individual Fe atoms on Pt(111): impact of the site-dependent giant substrate polarization," *Phys. Rev. Lett.*, vol. 111, p. 157204, 2013.

Bibliography

- [164] P. Błoński, A. Lehnert, S. Dennler, S. Rusponi, M. Etzkorn, G. Moulas, P. Bencok, P. Gambardella, H. Brune, and J. Hafner, “Magnetocrystalline anisotropy energy of Co and Fe adatoms on the (111) surfaces of Pd and Rh,” *Phys. Rev. B*, vol. 81, p. 104426, 2010.
- [165] G. E. Pacchioni, L. Gragnaniello, F. Donati, M. Pivetta, G. Autès, O. V. Yazyev, S. Rusponi, and H. Brune, “Multiplet features and magnetic properties of Fe on Cu(111): from single atoms to small clusters,” *Phys. Rev. B*, vol. 91, p. 235426, 2015.
- [166] C. T. Chen, Y. U. Idzerda, H.-J. Lin, N. V. Smith, G. Meigs, E. Chaban, G. H. Ho, E. Pellegrin, and F. Sette, “Experimental confirmation of the X-ray magnetic circular dichroism sum rules for iron and cobalt,” *Phys. Rev. Lett.*, vol. 75, p. 152, 1995.
- [167] P. Gambardella, S. S. Dhesi, S. Gardonio, C. Grazioli, P. Ohresser, and C. Carbone, “Localized magnetic states of Fe, Co, and Ni impurities on alkali metal films,” *Phys. Rev. Lett.*, vol. 88, p. 047202, 2002.
- [168] A. Lehnert, S. Rusponi, M. Etzkorn, S. Ouazi, P. Thakur, and H. Brune, “Magnetic properties of Fe and Co adatoms and Fe clusters magnetically decoupled from Ni₃Al(111) by an alumina bilayer,” *Phys. Rev. B*, vol. 81, p. 104430, 2010.
- [169] P. Gambardella, S. Stepanow, A. Dmitriev, J. Honolka, F. M. F. de Groot, M. Lingerfelder, S. Sen Gupta, D. D. Sarma, B. P. S. Stanesco, S. Clair, S. Pons, N. Lin, A. P. Seitsonen, H. Brune, J. V. Barth, and K. Kern, “Supramolecular control of the magnetic anisotropy in two-dimensional high-spin Fe arrays at a metal interface,” *Nat. Mater.*, vol. 8, p. 189, 2009.
- [170] B. Lazarovits, L. Szunyogh, P. Weinberger, and B. Újfalussy, “Magnetic properties of finite Fe chains at fcc Cu(001) and Cu(111) surfaces,” *Phys. Rev. B*, vol. 68, p. 024433, 2003.
- [171] E. Stavitski and F. M. F. de Groot, “The CTM4XAS program for EELS and XAS spectral shape analysis of transition metal *L* edges,” *Micron*, vol. 41, p. 687, 2010.
- [172] D. Weller, J. Stöhr, R. Nakajima, A. Carl, M. G. Samant, C. Chappert, R. Mégy, P. Beauvilain, P. Veillet, and G. A. Held, “Microscopic origin of magnetic anisotropy in Au/Co/Au probed with X-ray magnetic circular dichroism,” *Phys. Rev. Lett.*, vol. 75, p. 3752, 1995.
- [173] C. Piamonteze, P. Miedema, and F. M. F. de Groot, “Accuracy of the spin sum rule in XMCD for the transition-metal *L* edges from manganese to copper,” *Phys. Rev. B*, vol. 80, p. 184410, 2009.
- [174] P. Gambardella, S. Rusponi, M. Veronese, S. S. Dhesi, C. Grazioli, A. Dallmeyer, I. Cabria, R. Zeller, P. H. Dederichs, K. Kern, C. Carbone, and H. Brune, “Giant magnetic anisotropy of single Co atoms and nanoparticles on Pt,” *Science*, vol. 300, p. 1130, 2003.
- [175] V. I. Anisimov, J. Zaanen, and O. K. Andersen, “Band theory and Mott insulators: Hubbard *U* instead of Stoner *I*,” *Phys. Rev. B*, vol. 44, p. 943, 1991.

-
- [176] P. Giannozzi *et al.*, “QUANTUM ESPRESSO: a modular and open-source software project for quantum simulations of materials,” *J. Phys. Condens. Matter*, vol. 21, p. 395502, 2009.
- [177] M. Cococcioni and S. de Gironcoli, “Linear response approach to the calculation of the effective interaction parameters in the LDA+U method,” *Phys. Rev. B*, vol. 71, p. 035105, 2005.
- [178] A. Dal Corso and A. Mosca Conte, “Spin-orbit coupling with ultrasoft pseudopotentials: Application to Au and Pt,” *Phys. Rev. B*, vol. 71, p. 115106, 2005.
- [179] P. Mavropoulos, S. Lounis, R. Zeller, and S. Blügel, “Fe clusters on Ni and Cu: size and shape dependence of the spin moment,” *Appl. Phys. A*, vol. 82, p. 103, 2006.
- [180] V. S. Stepanyuk, L. Niebergall, R. C. Longo, W. Hergert, and P. Bruno, “Magnetic nanostructures stabilized by surface-state electrons,” *Phys. Rev. B*, vol. 70, p. 075414, 2004.
- [181] B. Chilian, A. A. Khajetoorians, S. Lounis, A. T. Costa, D. L. Mills, J. Wiebe, and R. Wiesendanger, “Anomalously large g factor of single atoms adsorbed on a metal substrate,” *Phys. Rev. B*, vol. 84, p. 212401, 2011.
- [182] J. Hu, B. Teng, F. Wu, and Y. Fang, “Fe nanostructures stabilized by long-range interactions on Cu(111): kinetic Monte Carlo simulations,” *New J. Phys.*, vol. 10, p. 023033, 2008.
- [183] P. Ohresser, G. Ghiringhelli, O. Tjernberg, N. B. Brookes, and M. Finazzi, “Magnetism of nanostructures studied by X-ray magnetic circular dichroism: Fe on Cu(111),” *Phys. Rev. B*, vol. 62, p. 5803, 2000.
- [184] J. T. Lau, J. Rittmann, V. Zamudio-Bayer, M. Vogel, K. Hirsch, P. Klar, F. Lofink, T. Möller, and B. v. Issendorff, “Size-dependence of $L_{2,3}$ branching ratio and $2p$ core-hole screening in X-ray absorption of metal clusters,” *Phys. Rev. Lett.*, vol. 101, p. 153401, 2008.
- [185] K. Hirsch, V. Zamudio-Bayer, J. Rittmann, A. Langenberg, M. Vogel, T. Möller, B. v. Issendorff, and J. T. Lau, “Initial- and final-state effects on screening and branching ratio in $2p$ X-ray absorption of size-selected free $3d$ transition metal clusters,” *Phys. Rev. B*, vol. 86, p. 165402, 2012.
- [186] A. C. Hewson, *The Kondo Problem to Heavy Fermions*. Cambridge University Press, 1993.
- [187] V. Madhavan, W. Chen, T. Jamneala, M. F. Crommie, and N. S. Wingreen, “Tunneling into a single magnetic atom: Spectroscopic evidence of the Kondo resonance,” *Science*, vol. 280, p. 567, 1998.
- [188] H. C. Manoharan, C. P. Lutz, and D. M. Eigler, “Quantum mirages formed by coherent projection of electronic structure,” *Nature*, vol. 403, p. 512, 2000.
- [189] M. Ternes, A. J. Heinrich, and W.-D. Schneider, “Spectroscopic manifestation of the Kondo effect on single adatoms,” *J. Phys. Condens. Matter*, vol. 21, p. 053001, 2009.

Bibliography

- [190] D. Goldhaber-Gordon, H. Shtrikman, D. Mahalu, D. Abusch-Magder, U. Meirav, and M. A. Kastner, "Kondo effect in a single-electron transistor," *Nature*, vol. 391, p. 156, 1998.
- [191] S. M. Cronenwett, T. H. Oosterkamp, and L. P. Kouwenhoven, "A tunable Kondo effect in quantum dots," *Science*, vol. 281, p. 540, 1998.
- [192] P. Jarillo-Herrero, J. Kong, H. S. J. van der Zant, C. Dekker, L. P. Kouwenhoven, and S. De Franceschi, "Orbital Kondo effect in carbon nanotubes," *Nature*, vol. 434, p. 484, 2005.
- [193] L. Bogani and W. Wernsdorfer, "Molecular spintronics using single-molecule magnets," *Nat. Mater.*, vol. 7, p. 179, 2008.
- [194] G. D. Scott and D. Natelson, "Kondo resonances in molecular devices," *ACS Nano*, vol. 4, pp. 3560–3579, 2010.
- [195] R. Robles, N. Lorente, H. Isshiki, J. Liu, K. Katoh, B. K. Breedlove, M. Yamashita, and T. Komeda, "Spin doping of individual molecules by using single-atom manipulation," *Nano Lett.*, vol. 12, p. 3609, 2012.
- [196] H. Kim, Y. H. Chang, S.-H. Lee, Y.-H. Kim, and S.-J. Kahng, "Switching and sensing spin states of Co-porphyrin in bimolecular reactions on Au(111) using scanning tunneling microscopy," *ACS Nano*, vol. 7, pp. 9312–9317, 2013.
- [197] L. Liu, K. Yang, Y. Jiang, B. Song, W. Xiao, L. Li, H. Zhou, Y. Wang, S. Du, M. Ouyang, W. A. Hofer, A. H. Castro Neto, and H.-J. Gao, "Reversible single spin control of individual magnetic molecule by hydrogen atom adsorption," *Sci. Rep.*, vol. 3, p. 1210, 2013.
- [198] A. Zhao, Q. Li, L. Chen, H. Xiang, W. Wang, S. Pan, B. Wang, X. Xiao, J. Yang, J. G. Hou, and Q. Zhu, "Controlling the Kondo effect of an adsorbed magnetic ion through its chemical bonding," *Science*, vol. 309, p. 1542, 2005.
- [199] I. Fernández-Torrente, K. J. Franke, and J. I. Pascual, "Vibrational Kondo effect in pure organic charge-transfer assemblies," *Phys. Rev. Lett.*, vol. 101, p. 217203, 2008.
- [200] T. Choi, S. Bedwani, A. Rochefort, C.-Y. Chen, A. J. Epstein, and J. A. Gupta, "A single molecule Kondo switch: Multistability of tetracyanoethylene on Cu(111)," *Nano Lett.*, vol. 10, p. 4175, 2010.
- [201] T. Komeda, H. Isshiki, J. Liu, Y.-F. Zhang, N. Lorente, K. Katoh, B. K. Breedlove, and M. Yamashita, "Observation and electric current control of a local spin in a single-molecule magnet," *Nat. Commun.*, vol. 2, p. 217, 2011.
- [202] V. Iancu, A. Deshpande, and S.-W. Hla, "Manipulating Kondo temperature via single molecule switching," *Nano Lett.*, vol. 6, p. 820, 2006.

-
- [203] A. Mugarza, C. Krull, R. Robles, S. Stepanow, G. Ceballos, and P. Gambardella, "Spin coupling and relaxation inside molecule-metal contacts," *Nat. Commun.*, vol. 2, p. 490, 2011.
- [204] A. Stróżecka, M. Soriano, J. I. Pascual, and J. J. Palacios, "Reversible change of the spin state in a manganese phthalocyanine by coordination of CO molecule," *Phys. Rev. Lett.*, vol. 109, p. 147202, 2012.
- [205] K. J. Franke, G. Schulze, and J. I. Pascual, "Competition of superconducting phenomena and Kondo screening at the nanoscale," *Science*, vol. 332, no. 6032, p. 940, 2011.
- [206] U. Fano, "Effects of configuration interaction on intensities and phase shifts," *Phys. Rev.*, vol. 124, p. 1866, 1961.
- [207] K. Nagaoka, T. Jamneala, M. Grobis, and M. F. Crommie, "Temperature dependence of a single Kondo impurity," *Phys. Rev. Lett.*, vol. 88, p. 077205, 2002.
- [208] A. F. Otte, M. Ternes, K. von Bergmann, S. Loth, H. Brune, C. P. Lutz, C. F. Hirjibehedin, and A. J. Heinrich, "The role of magnetic anisotropy in the Kondo effect," *Nat. Phys.*, vol. 4, p. 847, 2008.
- [209] T. Choi, M. Badal, S. Loth, J.-W. Yoo, C. P. Lutz, A. J. Heinrich, A. J. Epstein, D. G. Stroud, and J. A. Gupta, "Magnetism in single metalloorganic complexes formed by atom manipulation," *Nano Lett.*, vol. 14, pp. 1196–1201, 2014.
- [210] U. G. E. Perera, H. J. Kulik, V. Iancu, L. G. G. V. Dias da Silva, S. E. Ulloa, N. Marzari, and S.-W. Hla, "Spatially extended Kondo state in magnetic molecules induced by interfacial charge transfer," *Phys. Rev. Lett.*, vol. 105, p. 106601, 2010.
- [211] W. Wang, R. Pang, G. Kuang, X. Shi, X. Shang, P. N. Liu, and N. Lin, "Intramolecularly resolved Kondo resonance of high-spin Fe(II)-porphyrin adsorbed on Au(111)," *Phys. Rev. B*, vol. 91, p. 045440, 2015.
- [212] S. Grimme, "Semiempirical GGA-type density functional constructed with a long-range dispersion correction," *J. Comput. Chem.*, vol. 27, pp. 1787–1799, 2006.
- [213] V. Barone, M. Casarin, D. Forrer, M. Pavone, M. Sambi, and A. Vittadini, "Role and effective treatment of dispersive forces in materials: polyethylene and graphite crystals as test cases," *J. Comput. Chem.*, vol. 30, pp. 934–939, 2009.
- [214] P.-O. Löwdin, "On the non-orthogonality problem connected with the use of atomic wave functions in the theory of molecules and crystals," *J. Chem. Phys.*, vol. 18, pp. 365–375, 1950.
- [215] J. Kügel, M. Karolak, J. Senkpiel, P.-J. Hsu, G. Sangiovanni, and M. Bode, "Relevance of hybridization and filling of 3d orbitals for the Kondo effect in transition metal phthalocyanines," *Nano Lett.*, vol. 14, pp. 3895–3902, 2014.

Bibliography

- [216] O. Újsághy, J. Kroha, L. Szunyogh, and A. Zawadowski, “Theory of the Fano resonance in the STM tunneling density of states due to a single Kondo impurity,” *Phys. Rev. Lett.*, vol. 85, pp. 2557–2560, 2000.
- [217] P. P. Baruselli, R. Requist, A. Smogunov, M. Fabrizio, and E. Tosatti, “Co adatoms on Cu surfaces: ballistic conductance and Kondo temperature,” *Phys. Rev. B*, vol. 92, p. 045119, 2015.
- [218] B. K. Burgess and D. J. Lowe, “Mechanism of molybdenum nitrogenase,” *Chem. Rev.*, vol. 96, p. 2983, 1996.
- [219] T. H. Rod, B. Hammer, and J. K. Nørskov, “Nitrogen adsorption and hydrogenation on a MoFe₆S₉ complex,” *Phys. Rev. Lett.*, vol. 82, p. 4054, 1999.
- [220] T. H. Rod, A. Logadottir, and J. K. Nørskov, “Ammonia synthesis at low temperatures,” *J. Chem. Phys.*, vol. 112, p. 5343, 2000.
- [221] Ž. Šljivančanin, H. Brune, and A. Pasquarello, “Nitrogen fixation at passivated Fe nanoclusters supported by an oxide surface: identification of viable reaction routes using density functional calculations,” *Phys. Rev. B*, vol. 80, p. 075407, 2009.

Acknowledgements

First and foremost, I would like to thank my PhD advisor, Harald Brune, for giving me the opportunity to be part of his group and for pushing me to grow scientifically through the discussion of results and the preparation of manuscripts, for encouraging me to participate to international conferences and for supporting my summer school.

I express my gratitude to Katharina Franke, Roman Fasel and Magali Lingensfelder, who served in my jury committee, and to Vincenzo Savona, who presided it.

A big thank you to Marina for the patience with which she helped me with my research, for the support she gave me, both for work and for my personal life, and for all the good moments we shared in front of the STM, of the manuscript drafts, and of a good beer. Thanks to Francois for being there as well, with his humour and his endless problem solving skills. They have been my Swiss family.

Thank you to Fabian and Chongqi, my wonderful office mates, and to all the members of the group for the fun we had together, the coffee breaks and the lunches in the sun at the Banane. Special thanks to the Italian gang, Stefano, Fabio, Sergio, Alberto and Thereza: you all made Lausanne feel like home.

And of course thanks to Luca, who has been at my side from the beginning to the end and has taught me to live in the moment.

Thanks to Emanuele and Silvia, who have been with me in the good and in the bad moments. In particular, thanks to Emanuele for the support with the softwares that refused to obey me, literally at any time of day and night.

Last but not least, a big thank you to my parents, who are always there for me.

Curriculum Vitae

Name: Giulia Elisabetta Pacchioni
Nationality: Italian
Date of birth: 15.12.1987

2015 Associate Editor, Nature Reviews Materials, London, UK
2011 - 2015 PhD studies / teaching assistant, EPFL, Lausanne, Switzerland
2009 - 2011 Master's degree in Physics, University of Milan, Italy
2006 - 2009 Bachelor's degree in Physics, University of Milan, Italy
2001 - 2006 High school diploma, Liceo Classico G. Carducci, Milan, Italy

Publications

"Two-orbital Kondo screening in a self-assembled metal-organic complex", **Giulia E. Pacchioni**, Marina Pivetta, Luca Gagnaniello, Fabio Donati, Gabriel Autès, Oleg V. Yazyev, Stefano Rusponi and Harald Brune, *In preparation*.

"2D crystals of Er(trensol) single-ion magnets on graphene decoupling layers", Jan Dreiser, **Giulia E. Pacchioni**, Fabio Donati, Luca Gagnaniello, Alberto Cavallin, Kasper S. Pedersen, Jesper Bendix, Marina Pivetta, Stefano Rusponi and Harald Brune, *Submitted to Nano Lett.*

"Competing interactions in the self-assembly of NC-Ph₃-CN molecules on Cu(111)", **Giulia E. Pacchioni**, Marina Pivetta and Harald Brune, *J. Phys. Chem. C.*, **119**, 25442, 2015

"Origin of perpendicular magnetic anisotropy and large orbital moment in Fe atoms on MgO", Susanne Baumann, Fabio Donati, Sebastian Stepanow, Stefano Rusponi, William Paul, Shruba Gangopadhyay, Ileana G. Rau, **Giulia E. Pacchioni**, Luca Gagnaniello, Marina Pivetta, Jan Dreiser, Cinthia Piamonteze, Chris P. Lutz, Roger M. Macfarlane, Barbara A. Jones, Pietro Gambardella, Andreas J. Heinrich and Harald Brune, *Phys. Rev. Lett.*, **115**, 237202, 2015.

"Multiplet features and magnetic properties of Fe on Cu(111): From single atoms to small clusters", **Giulia E. Pacchioni**, Luca Gagnaniello, Fabio Donati, Marina Pivetta, Gabriel Autès, Oleg V. Yazyev, Stefano Rusponi and Harald Brune, *Phys. Rev. B*, **91**, 235426, 2015.

"Temperature-dependent self-assembly of NC-Ph₅-CN molecules on Cu(111)", Marina Pivetta, **Giulia E. Pacchioni**, Edgar Fernandes and Harald Brune, *J. Chem. Phys.*, **142**, 101928, 2015.

"Formation of Fe cluster superlattice in a metal-organic quantum-box network", Marina Pivetta, **Giulia E. Pacchioni**, Uta Schlickum, Johannes V. Barth and Harald Brune, *Phys. Rev. Lett.*, **110**, 086102, 2013.